Rudder loads of a moored FPSO in waves and current

A study by experimental means

by

Hanna Pot

to obtain the degree of Master of Science
at the Delft University of Technology,
to be defended publicly on Thursday June 28, 2018.

Student number:	4176588	
Project duration:	September 1, 2017 – June 28, 2018	
Thesis committee:	Prof. dr. ir. A. P. van 't Veer,	TU Delft, supervisor
	Ir. P. Naaijen,	TU Delft

TU Delft

Observe! There are a few things as important, as religious, as that.
Frederick Buechner, minister

Abstract

Floating Production, Storage and Off-loading units (FPSO) are often refitted tankers that sail to their offshore location on own propulsion. Here, they are typically moored for twenty years. The rudder is fixed in the center by mechanical locking of the rudder machine to avoid unwanted motions. A class society's study showed that many FPSO's face challenges with rudder locking; the loads can be more damaging in moored condition than in sailing conditions. Class societies recommend to remove the rudder or to keep the steering motors running. Both solutions are costly and troublesome. Therefore, mechanical locking is highly preferred. However, the design of such a locking construction requires a detailed load assessment.
The hydrodynamic loads on the rudder are caused by wave oscillations, current and ship motions. The loads are complex and governed by flow separation. The engineering application provokes the desire for an uncomplicated load prediction. This research tries to give an answer to the question whether it is possible to predict the complex loads with a calculation model that only requires the undisturbed flow pattern and load coefficients depending on the rudder's shape.

Little research is executed to rudders with oscillating flow patterns perpendicular to its blade. Towing tank experiments are executed rather than computational simulations, as validation of the latter could not be guaranteed. The problem is isolated to a rudder model only. Within this study, two rudder models are tested, one with a typical rudder shape and one with a more simple, rectangular form. In the latter, by using pressure sensors – fitted in the model – an in-depth flow insight around the rudder is obtained. A hexapod oscillated the rudders in regular roll and sway. Currents were imposed by driving the carriage.

The results of the towing tank experiments show that only the Morison model – extended with the third and fifth term of its Fourier's expansion – gives an appropriate description of the force history in sway oscillation. The regular 2-coefficient form of the Morison model underestimates the peak loads, which is of vital importance. It is only due to the peak loads possible to study the fatigue and ultimate strength of the rudder locking system.
When flow fields of sway oscillations and currents perpendicular to the rudder's blade are combined, the 'relative velocity' Morison model – depending on both flow velocities – is expected to present the most accurate load prediction. However, the model shows large discrepancies with the measured force histories. This is a striking result, as the 'relative velocity' Morison model is found best applicable in similar studies to cylinders. Despite the presence of the current, the measured force histories are surprisingly symmetrical over the oscillation' cycle. Therefore, the Morison model which does not take currents into account, presents better results.

In order to use the Morison model, empirical coefficients are required. These coefficients depend on the Keulegan-Carpenter (KC) number: a dimensionless number that substantiates the relation between the oscillations' amplitude and the generated vortices. The influence of the vortex generation and -shedding on the loads cannot be stressed enough. The frequency independence found in this study substantiates this. The rudder's aspect ratio of 1.5 allows vortex separation around all four edges. The magnitude of both the inertia- and drag coefficient is lowered by a factor two, compared to the coefficients of infinite length flat plates. The lift profile and the flat plate profile show comparable results and clear trends are discovered between the third- and fifth order load coefficients and the KC number. The pressure sensors provided valuable insights in flow behaviour. The free surface's vicinity increased the wake's irregularity.

Oscillations with a non-uniform velocity profile over the rudder's span are likely in ocean environments. Unfortunately enough, the results of the roll oscillation experiments could not be relied on. Moreover, eighty to ninety percent of the measured loads accounted for the mass inertia. This significant amount caused a large sensitivity on the hydrodynamic loads; a phase' miscalculation of a few hundredths of a second could cause significant deviations in the load coefficients. It is recommended to execute experiments with higher reliability for both sway- and roll oscillations. The study can be extended by enlarging the test matrix. Furthermore, computational simulations can provide more insights in the flow behaviour and loads.

Contents

Nomenclature

Abbreviations

KC	Keulegan-Carpenter number
Re	Reynolds number
AS	Aft Side sensor: the pressure sensor positioned at the current's pressure-side.
CFD	Computational Fluid Dynamics
CoG	Center of gravity
CoR	Center of rotation
FPSO	Floating Production Storing and Offloading unit
FS	Front Side sensor: the pressure sensor positioned at the current's front-side
MPM	Multi-Point Mooring
SPM	Single Point Mooring

Arabic Symbols

$\ddot{y}$	Acceleration in sway-direction	m/s^2
$\Delta p_{hs}(t)$	Time-varying hydrostatic pressure	Pa
ΔR	Remainder function consisting of the third- and fifth order Fourier terms	N
$\hat{\mathbf{n}}$	Carthesian unit vector	–
$\hat{\mathbf{r}}$	Radial unit vector	–
$\mathbf{b}$	Measured time-series, used as input a for the Least Squares solution	
$\mathbf{F}$	Force vector composed of a force in x- and y-direction	N
$\mathbf{x}*$	'Best fit' column vector of unknown parameters for Least Squares solution	
$\mathbf{x}$	Unknowns in the Method of Least Squares, collected in a column vector of length n	
A_0	Cross-sectional area	m^2
A_n	n^{th} order sine-related Fourier terms	N
A_s	Frontal area of the oscillating body	m^2
$A_{1,cur}$	Acceleration related Fourier coefficient of the relative velocity Morison model	–
$A_{I,b2}$	Amplitude of the inertia force during sway oscillations in air	N
$A_{I,b4}$	Amplitude of the inertia force during roll oscillations in air	N
B_n	n^{th} order cosine-related Fourier terms	
$B_{1,cur}$	Velocity related Fourier coefficient of the relative velocity Morison model	–
$B_{I,b2}$	Amplitude of the drag force during sway oscillations in air	N

$B_{I,b4}$	Amplitude of the drag force during rolls oscillations in air	N
c	Chord length of plate width	m
C_d	Drag coefficient	–
$C_{d,ridj}$	Drag coefficient as defined by Ridjanovic (1962)	–
$C_{d,Vc}$	Drag coefficient as used in the drag equation for constant current	–
C_{dc}	Drag coefficient of the relative velocity Morison model	–
C_{mc}	Inertia coefficient of the relative velocity Morison model	–
C_m	Inertia coefficient	-
$C_{p,d}$	Instantaneous drag coefficient determined with the pressure sensors' signal	–
$C^+_{p,d}$	Instantaneous drag coefficient of the body's front-side	–
$C^-_{p,d}$	Instantaneous drag coefficient of the body's wake-side	–
$C^+_{p,I}$	Instantaneous inertia coefficient of the body's front-side	–
$C^-_{p,I}$	Instantaneous inertia coefficient of the body's wake-side	–
$C_{p,m}$	Instantaneous inertia coefficient of the body's wake-side	–
D	Cylinder's diameter	m
d_m	Distance between the center of mass and the center of rotation	m
D_r	Root's submergence	m
F	Force on a body in oscillation's direction	N
f	Assumed solution for a Least Squares approximation	N
F_d	Drag force	N
F_m	Force predicted with the Morison model	N
F_x	Force in x-direction on a submerged cylindrical cylinder in uniform flow in x-direction	N
$F_{HD,r}$	Hydrodynamic forces on the rudder	N
$F_{HD,s}$	Hydrodynamic forces on the rudder stock	N
$F_{I,b2}$	Mass inertia force in y-direction during sway oscillation	N
$F_{I,b4}$	Mass inertia force in y-direction during roll oscillation	N
$F_{I,b}$	Body mass inertia force	N
$F_{I,connectingrods}$	Mass inertia force of the connecting rods	N
$F_{I,frame}$	Mass inertia force of the frame	N
$F_{I,r}$	Mass inertia force of the rudder model	N
F_{it}	Flow's inertia force	N
$F_{M,cur}$	Force predicted with the relative velocity Morison model	N
$F_{m,cur}$	Force predicted by the 'relative velocity' Morison model	N
F_{signal}	Signal measured by the load cells in an arbitrary direction	N

$F_{x,b}$	Body force in x-direction	N
G	Matrix of size $[m \cdot n]$, used as input for a Least Squares solution	
g	Gravitational constant: 9.81	m/s^2
h_p	Plate height	m
L	Body's characteristic length	m
m	Number of vector entries of a measured time series	
m_a	Added mass	kg
m_{eq2}	Equivalent mass in y-direction during sway oscillation	kg
m_{eq4}	Equivalent mass in y-direction during roll oscillation	kg
N	Number of input arguments	–
n	Number of columns of Least Squares problem	
n	Positive integer	–
p	Pressure	Pa
P_d	Pressure at the moment of maximum velocity	Pa
P_I	Pressure at the moment of maximum acceleration	Pa
r	Measure in cylindrical coordinate system	r
r_a	Radius of a cylinder	m
r_d	Distance between the center of rotation and model's geometrical center	°
S	Surface of a 2D body	m
S_{LSQR}	Minimized differences between assumed solution and measured signal with the method of Least Squares	N
T	Period of oscillation	s
t	Time	s
$T_c(t)$	First zero-crossing of the combined velocity	rad
u	Local flow in x-direction	m/s
$U(t)$	Undisturbed flow velocity	m/s
$U_c(t)$	Combined velocity, including both the fluid velocity due to oscillation and the current velocity	m/s
U_m	Maximum flow velocity in one oscillation cycle	m/s
U_r	Velocity in radial direction, for a cylinder in steady, potential flow	m/s
U_α	Velocity in tangential direction, for a cylinder in steady, potential flow	m/s
v	Local flow velocity in y-direction	m/s
V_0	Reference volume of the oscillating body	m^3
V_c	Steady current velocity	m/s
V_{rod}	Displacement of the rod	m^3

w	Local flow velocity in z-direction	m/s
x	Displacement in surge direction	
x_a	Amplitude of oscillation in x-direction	m
x_b	x-axis of the vessel bounded coordinate system	
y	Displacement in sway direction	
y_a	Amplitude of sway oscillation	m
y_b	y-axis of the vessel bounded coordinate system	
z	Displacement in heave direction	
z_b	z-axis of the vessel bounded coordinate system	

Greek Symbols

α	Directional angle used for the cylindrical coordinate system	rad
$\ddot{\phi}$	Angular acceleration of roll around the CoR	rad/s^2
ϵ_m	Phase of the oscillation motion	rad/s
Λ	Velocity parameter, defined by $\frac{V_c}{U_m}$	–
ν	Kinematic viscosity	m^2/s
ω	Angular velocity of an oscillation, defined by $\frac{2\pi}{T}$	rad/s
ϕ	Roll angle of a vessel	$^\circ$
ϕ_a	Amplitude of roll oscillation	$^\circ$
ϕ_p	Velocity potential	
ψ	Yaw angle of a vessel	$^\circ$
ψ_p	Body force potential	
ρ	Water density	kg/m^3
θ	Pitch angle of a vessel	$^\circ$

List of Figures

List of Tables

1 Introduction

Figure 1.1: General layout of a FPSO. MODEC (2016)

Figure 1.2: Semi-balanced rudder. Cozanet (2006)

Floating Production, Storage and Offloading (FPSO) units pump up, store and process hydrocarbons while anchoring offshore. The units are often refitted tankers that sail on own propulsion to their offshore location. An overview photo of such a refitted tanker is shown in figure 1.1. The ships are typically moored offshore for twenty to twenty-five years. At its offshore location, the rudder is often fixed in the center by mechanical locking of the rudder machine.
An inspection, repair and maintenance study of FPSO's was executed by Lloyd's Register of Shipping. The study shows that a significant amount of FPSO's face problems with rudder locking (Lloyd's Register, 2003). The sources for the study included a questionnaire about system failures of their equipment among ten FPSO operators in the UK continental shelf . Internal communication with a Dutch offshore company pointed out the same problems. Locking-failure causes unwanted rudder motions and may eventually lead to troublesome situations for the ship and the installed operation equipment.

The rudders of large tankers are often semi balanced rudders, which look like the rudder shown in figure 1.2. A drawing of a rudder and the main nomenclature is presented in figure 1.3a. The rudder is connected with the steering machinery by the rudder stock, that leads to the ship's hull. The machinery often consists of a double ram, that is driven by four hydraulic cylinders. A drawing of a typical rudder machine is shown in figure 1.3. A rudder and its machinery are principally designed for sailing conditions. At service speed they should be able to maintain and change the course of the ship. At lower speeds, the main function is manoeuvring. The rudder and machinery should be accounted for all loads in these conditions. In mooring conditions, no special remarks about rudder- and machinery design is given in the class rules. (Molland and Turnock, 2007) (Det Norske Veritas, 2007) (Barrass, 2004)
Rudder-locking in the ship's center is mostly done by mechanical locking of the crosshead of the rudder machine. One way of doing this, it by placing blocks between the rams and the rampson slides. Another option

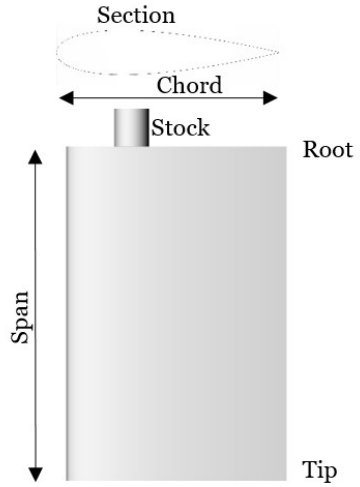

(a) Rudder's nomenclature.

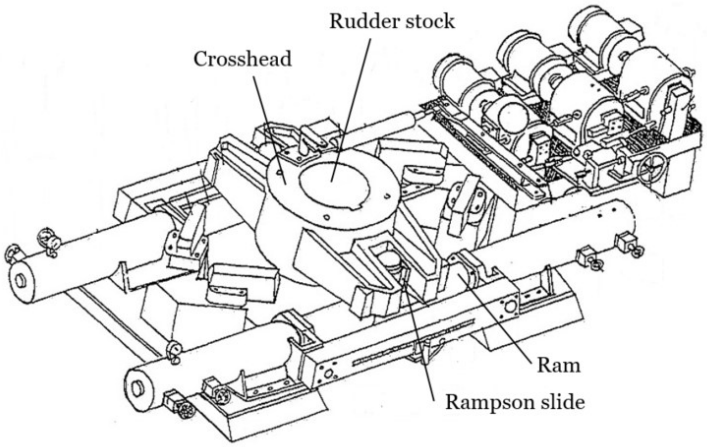

(b) Rudder machinery. Adapted from (BestShippingNews.com, 2018)

Figure 1.3: Drawings of the rudder and the rudder machinery.

is the placement of brackets between the hull and the rudder's tip. Preferences depend on the original rudder design and the expected loads.

1.1. Problem statement

Over the last years several FPSO's suffered from significant issues with rudder-locking and mechanical breakdowns of the steering gear occurred (Lloyd's Register, 2003). It appeared that the forces on the rudder in moored condition can be more damaging than the loads in sailing conditions. Recommendations on how to handle the rudder of a moored FPSO are currently to remove the rudder if possible, or to keep the steering motors running (Lloyd's Register, 2003). Both solutions are costly and troublesome, and internal communication with a FPSO operator showed that mechanical locking is highly preferred. For the design of such a mechanical locking construction, the loads on the rudder should be predicted in detail.

1.2. Research goal

The aim of this research is to derive in depth insights in the loads on a rudder of an offshore moored FPSO. The expected main loads consist of low-speed current and waves. These flows cause complex loads, governed by separation. In the end, a practical load prediction on the rudder is desired. This study therefore tries to capture the complex loads in a practical load prediction model. The research question is defined by:

Can the - by separation governed - loads on a FPSO's rudder in oscillating and steady flow be predicted with a calculation model that only requires the undisturbed flow and empirical load coefficients?

A lot of parameters influence the loads on the rudder. This research is first on this specific topic. Therefore the problem is isolated and the focus is laid on the principal flow types that act on the rudder. The loads in regular oscillation without currents are assessed prior to non-regular oscillation and oscillation with current. Furthermore, the diffraction- and radiation effects are minimized, although some attention is given to the effects on the loads at shallow draughts. The vicinity of the hull is not examined.

1.3. Methodology

This study is started with a theoretical analysis. This analysis forms a theoretical basis of the flow physics and a coarse prediction of the expected loads in oscillation. However, a literature review only is not satisfactory to identify the loads on the rudder. In the second part of this study, the loads on the rudder are studied by experimental means.

Experimental tests are believed to be a reliable method. Loads can be scaled accurately and the facilities of the TU Delft's Maritime and Transportation Technology department make it possible to measure loads and pressures on an oscillating and rotating scale model. Another method of determining the loads is by Computational Fluid Dynamics (CFD) simulations. These simulations are generally less expensive than experimental tests, but with this method correctness cannot be guaranteed. Waves and current can act perpendicular to the rudder plane, through which a large, turbulent wake area is generated behind the body. Turbulence models are therefore required and moreover, three-dimensional flow effects make the simulations rather complex. The turbulence and three-dimensionality give rise to uncertainty of the results' fairness. As only limited validation data is available, CFD simulations lack reliability. The experimental are validated with experimental data from Ridjanovic (Ridjanovic, 1962), Keulegan and Carpenter (Keulegan and Carpenter, 1958), Ikeda (Ikeda *et al.*, 1979) and Sarpkaya (Sarpkaya and O'Keefe, 1996).

The final goal of this study is to capture the complex loads on the rudder in a model, suitable for engineering practices. The Morison model is used for this purpose. Ideally, the model should account for various flow conditions and correct for free surface effects as well.

1.4. Expected results

The aim of this research is to investigate if the Morison model can predict the rudder loads, using experimentally obtained load coefficients. Therefore, drag- and inertia coefficients of a rudder profile are required. It is expected that these coefficients are depending on the Keulegan-Carpenter (KC) number, as observed for flat plates and cylinders as well. New relations between the load coefficients and the KC number are thus foreseen. Local flow behaviour is expected to affect the loads, so attention is paid to local pressures, end-effects and vortex generation.

1.5. Document structure

This report starts in chapter 2 with a literature review. This review includes the expected loads on the rudder in moored conditions and an analysis of the studies executed on the topic of oscillating bodies. By the end of this chapter, the knowledge gaps are identified and detailed research objectives set. Chapter 3 describes the set-up of the experiments. In the subsequent chapter the corrections of the measured signals and their impacts are elaborated, as well as the experimental uncertainty. Chapter 5 and chapter 6 present and discuss the results of the sway oscillations in zero-current respectively current conditions. The final conclusions are drawn in chapter 7 and recommendations are elaborated in chapter 8.

2

Literature review

This chapter includes an elaboration of the research problem. Theoretical background on the problem is given and the current state of research is discussed. The last two sections discuss the knowledge gaps and states the research objectives.

2.1. Environmental loads & ship motions

This first section describes the expected environmental loads acting on the FPSO's rudder and the ship motions expected on the offshore location. The coordinate system used throughout this report is described first.

2.1.1. Coordinate system

This report mainly uses a vessel-bounded coordinate system, a coordinate system that is 'attached' to the ship and moves along with it. This 'body-bound' coordinate system is shown in figure 2.1. The body-bound axis are denoted by x_b, y_b and z_b and the motions of the vessel in x-, y- and z-direction are called surge-, sway- and heave. The positive direction of surge is towards the bow. The positive direction for sway is towards port-side, and an upward heave motion is positive as well. Rotations around the x-, y- and z-axis are named rolling, pitching and respectively yawing. They are denoted by the symbols ϕ, θ and respectively ψ. The system is right-handed, so the roll angle is positive if the ship rolls to starboard, the pitch angle is positive when the bow moves downward and a positive yaw angle is observed for a bow turning to port-side.

2.1.2. Environmental loads

The environmental loads that may act on the rudder are loads induced by ship motions, low-speed currents, wave orbital motions and wave impact (Van 't Veer *et al.*, 2011) (Ikeda *et al.*, 2004). Their physics and their possible impact on the rudder are explained in the next paragraphs.

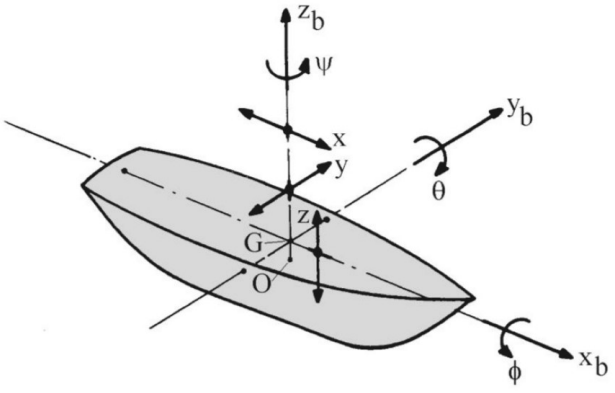

Figure 2.1: Vessel-bounded coordinate system. Journée *et al.* (2015).

Wave orbital loads Waves exist of up- and downward moving water particles. These particles make orbital motions. In deep water with regular waves, the orbital motions are by approximation equal to circles. The circular motion of the water particles declines over depth. Figure 2.2 shows the circular motions of the particles. The motions and thus particle velocities in ocean environments can be described by a sine- and cosine function, depending on among other the wave frequency and amplitude (Holthuijsen, 2007). An arbitrary, stationary point in the water experiences an oscillating flow velocity and acceleration. Regarding the rudder blade, the water particles are oscillating relative it, causing a cyclic load. Such a flow is also named time-dependent or 'unsteady'. (Holthuijsen, 2007)
This fluid oscillation is obviously a simplification. In reality, flow bends around a body. The load, applied by the undisturbed wave only, is called the 'Froude-Krilov' wave load. This simplification assumes that the wave penetrates the rudder or ship without being disturbed. The deflection of wave particles due the presence of a structure is called the diffraction of the wave. Diffraction causes the fluid flow to become less uniform. Water particles are diffracted in x-, y- and z-direction and therefore the flow around the rudder is called 'three-dimensional'. A third fluid velocity component is the flow caused by the motion of the body. This is called radiation. Radiation waves make the flow less uniform too. (Journée *et al.*, 2015)

Wave impact An FPSO can be fully loaded or in ballast condition. In ballast condition, the rudder is often not fully submerged. Because of that, the rudder can be prone to wave impact loads. This can occur by means of wave run-up, breaking waves or horizontal wave slamming. According to a damage report of a FPSO by Lloyd's Register, severe damage on the steering gear was caused by a wave slam on the rudder. Wave impact loads may have a large influence on the steering gear break-downs. (Lloyd's Register, 2003)

In Det Norske Veritas (2007) extensive methods for assessing slamming loads are explained. In these methods, the load estimation is governed by the lateral area, the relative velocity of the incoming water particles and the angle of the incoming water mass. The exact shape of the body is thus not taken into account. Wave impact on the rudder is therefore not picked as governing knowledge gap. (Det Norske Veritas, 2007) (Faltinsen, 2005)

Currents Low-speed tidal currents and drift motions can cause nearly steady motions. The low-speed tidal currents at offshore locations have a maximum velocity of 2 to 3 knots (Remery and Oortmerssen, 1973). Depending on its direction, the current can impose a drag- and lift component. Waves with a non-perpendicular angle of attack on the rudder may cause the same effect.
Much research is executed to flat plates and lift profiles in current. The load on the body can often be approximated with a simple drag formula (Sheldahl and Klimas, 1981) (White, 2011). However, it would be unique if only currents act on the rudder. It is likely that both waves and current act on the rudder, causing a combined steady-unsteady load model.

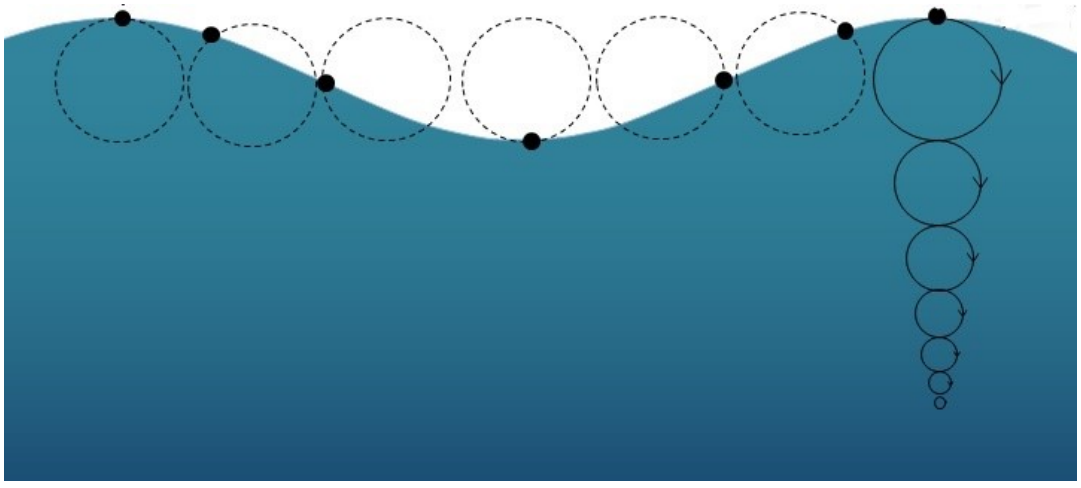

Figure 2.2: Orbital motion of water particle in deep water wave. Adapted from Earle (2015).

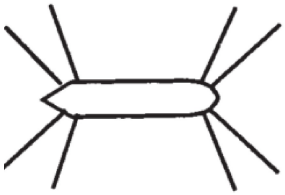

(a) Multi-Point mooring system. Shimamura (2002).

(b) Single point mooring system with external turret. Shimamura (2002).

Figure 2.3: Basic two types of mooring systems.

2.1.3. Ship motion induced loads

In the previous section, the ship was considered as stationary body. Due to wind, waves and current, moored ships are prone to motions as well. This causes an additional relative flow of the water. In this subsection the mooring techniques of FPSO's are discussed first, as it influences the ship's motions. Subsequently the flow patterns due to the ship's motions are discussed.

Mooring techniques FPSO's are moored in basically two ways. The conventional system is spread mooring or Multi-Point Mooring (MPM), which is conceptually shown in figure 2.3a. A second system is Single Point Mooring (SPM) or turret mooring. This system moors the vessel to a single point through which it is able to weathervane around it. The schematic view of this system is shown in figure 2.3b. A SPM system can have an external turret or internal turret. Spread moored FPSO's have a relatively fixed orientation . At locations where the weather conditions are merely unidirectional, for example at locations with a steady swell, spread mooring systems are widely used. This system is often lighter and cheaper. When the direction of wind, waves and currents is likely to vary, a spread mooring system is not preferable any more. In beam seas, large loads can act on the anchors of spread moored systems, making this option costly and less favourable. SPM systems are then preferred. (England *et al.*, 2001)
The motions of a vessel depend on the type of mooring. A spread moored vessel can be prone to roll motions, especially when incident waves have a relative large angle of attack. The roll motions of a SPM moored vessel are often smaller. Besides roll motions, the vessels can make by approximation steady motions as well. Spread moored vessels are likely to make low frequency swaying motions and weathervaning of SPM moored vessels can cause similar low frequent motions. (England *et al.*, 2001)

Unsteady motion induced loads FPSO's which are refitted tankers can be prone to roll motions induced by waves. This occurs especially in beam seas, which can be encountered in spread mooring. The rudder is dragged through the water as a result of the roll motion. This is a similar motion as an oscillating pendulum. In this condition, the undisturbed flow velocities and accelerations vary over the span of the rudder. The loads are highly dependent on the flow velocity and acceleration. An unsteady and non-uniform load over the span of the rudder is thus expected. (Journée *et al.*, 2015)

Steady motion induced loads Nearly steady motions can be induced by a vessel's motion as well. In spread mooring the vessel can drift in sway direction. For SPM systems, the vessel can weathervane around the buoy, causing transverse currents on the rudder (Ikeda *et al.*, 2004). Both motions are at low speed and steady by approximation.

2.1.4. Final notes on environmental loads

The flow pattern around the rudder is influenced by the ship's mooring system and the types of environmental loads present at the offshore location. It is likely that a combined steady-unsteady flow pattern acts on the rudder. Roll motion implies a unsteady, non-uniform flow pattern on the rudder. The hull causes flow diffraction and radiation, which makes the flow less uniform.

2.2. Introduction to fluid dynamics of immersed bluff bodies

For some of the flow conditions described in the previous section, the steady or unsteady flow direction is nearly perpendicular to the rudder plane. The rudder then acts as a bluff body; a body that principally ex-

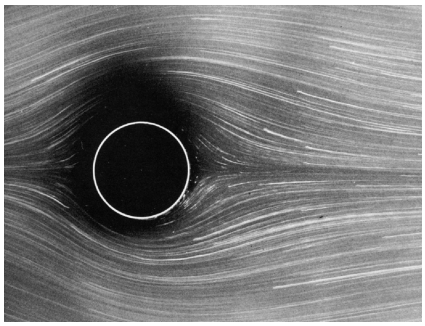

(a) Cylinder in unseparated, laminar flow. Dyke (1982).

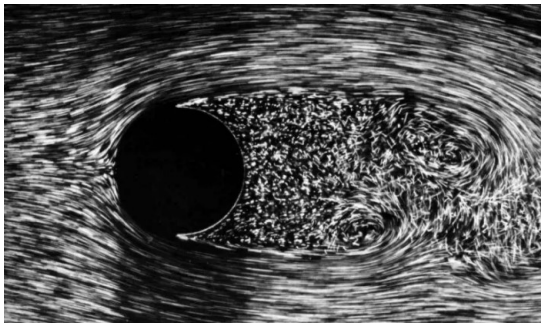

(b) Cylinder separated flow. Dyke (1982).

Figure 2.4: Separated and unseparated flow around a smooth cylinder in steady flow.

periences drag through flow separation. It is the opposite of a streamlined body. In this section the basic working mechanisms of dynamic fluid behaviour around bluff bodies are described.

2.2.1. Physical explanation of the fluid behaviour

The forces on bodies in a fluid are composed of pressures, shear stresses and body forces, like gravity. The total force is calculated by integrating the pressures and shear stresses over the body's surface and adding the body forces, if necessary. When flow observes a body, it is forced to bend around it. Due to this, the pressure in the fluid increases in the vicinity of the body. In flow without any viscosity, the flow would bend precisely around the body and back. However, real fluids contain viscosity. This basically is 'resistance' in the flow, which depends on the fluid's velocity. So in fluids that are not at rest, viscosity causes shear stresses on the body's surface and may add circulations in the flow. An important measure to evaluate the flow around a body is the dimensionless Reynolds number Re. It is defined by the steady fluid velocity V_c times the body's characteristic length L divided by the kinematic viscosity ν in m^2/s:

$$Re = \frac{V_c \cdot L}{\nu} \tag{2.1}$$

In low Reynolds number regions, the flow is generally called laminar. This means that no disorganised layers and wake fields are generated. If the Reynolds number increases, the flow may become turbulent. This is a state in which highly disorganised wakes and boundary layers are observed. Figure 2.4a shows a cylinder in laminar flow and figure 2.4b shows a cylinder with a turbulent wake. In the laminar, steady flow regime, forces on a body are governed by pressure differences over a body's surface and shear stresses as a result of viscosity. In turbulent flow, large pressure suctions are acting on the body. (Kundu *et al.*, 2016)

Boundary layer separation Due to surface roughness effects, a fluid can not have a velocity at the body's surface. Near the body's surface, the fluid velocity increases from zero to the actual local flow velocity around the body. This thin acceleration layer is called the boundary layer.
When steady or unsteady flows act on a bluff body, the flow can have difficulties in following the body's curvature. If the flow is not able to follow the body's curvature any more, an adverse pressure gradient is generated. At the location of the adverse pressure gradient, the boundary layer separates from the body. Separation depends mainly on the body's curvature and the fluid velocity. For steady flows it thus depends on the Reynolds number. Boundary layer separation can occur in both the laminar- and turbulent flow regime. If a body has a sharp edge, for example a flat plate, separation starts already at very small fluid velocities. The separation point is distinctively at the edge (Li, 1989) (Graham, 1980). If a body has a rounded edge, for example a circular cylinder, the flow can follow the body's curvature up to higher velocities. Separation then starts at higher Reynolds numbers. Furthermore, the point of separation of rounded edges can vary, as this is a function of both the curvature and the state of the boundary layer (Bearman, 1984).
When boundary layer separation takes place, the 'former' boundary layer is dragged along with the flow, towards the wake of the body. The separated boundary layer contains fluid particles with a high velocity, while the fluid in the wake has a very low velocity. In between these areas, a shear layer is generated. Due to this shear layer, the separated boundary layer tends to curl. This curl in the flow is called a vortex. The fluid velocity of particles in a vortex is theoretically twice as high as the undisturbed velocity. (Kundu *et al.*, 2016)

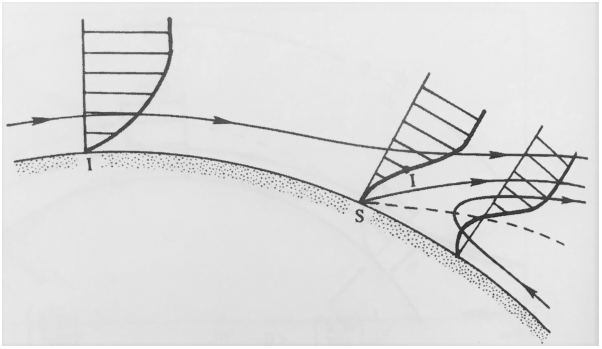

Figure 2.5: Separation of a boundary layer. The velocity profiles and stream lines of the boundary layer are shown. The dashed line indicates the zero-velocity shear line. Kundu *et al.* (2016).

In steady flows, the vortex pattern depends on the Reynolds number. If the direction of the flow alternates, vortices can be generated in alternating directions. In such a flow, the generation of vortices is not by any means depending on the body's shape and the Reynolds number. The separation of the boundary layer and the generation of vortices alters the pressure on the body and the shear stress at the body's surface. This may have a significant influence on the fluid forces on the body.

2.2.2. Mathematical description of forces on a body in uniform flow

The flow around a body in uniform flow can be approximated by a mathematical model. This mathematical model is used further in this study and is therefore derived here in detail. The derivation is executed for a for a cylinder of infinite length, but the mathematical concept is valid for any body in uniform flow.
The flow is assumed inviscid and incompressible. The cylinder is placed vertical, so its cross-section lays in the horizontal x-y plane. Gravity is therefore neglected. The cylinder is assumed to have an infinite length, and therefore the flow in z-direction is assumed nil. As explained in the previous subsection, the forces on a submerged body are calculated by integrating the pressures and shear stresses over the body's surface. In this example, the flow is assumed inviscid, so no shear stresses act on the body. The force vector $\mathbf{F}$ contains the forces in x- and y-direction per unit length on the two-dimensional body. The vector is described by (Sarpkaya and Isaacson, 1981)

$$\mathbf{F} = \int\int_S -p\hat{\mathbf{n}}\, dS \tag{2.2}$$

in which S is the body's surface, p the pressure and $\hat{\mathbf{n}}$ the unit vector normal to the surface, as pressure acts per definition perpendicular to the surface. For a circular 2D cylinder, it is convenient to rewrite the equation in polar coordinates. This is shown in equation 2.3. The Cartesian unit vector $\hat{\mathbf{n}}$ is replaced by the radial unit vector $\hat{\mathbf{r}} = \binom{r_r}{r_a} = \binom{1}{0}$, as pressure only acts in radial direction. The cylinder radius r_a is added, as it is required for proper integration.

$$\mathbf{F} = \int_0^{2\pi} -p\hat{\mathbf{r}} r_a\, d\alpha \tag{2.3}$$

This study focusses on the drag- and inertia loads, which are both in the direction of the flow. Only the loads in the direction of the flow, the x-direction, are thus examined. The term $\cos(\alpha)$ is the projection on the x-axis, and (1) is the radial term r_r of the radial unit vector; elaborating the equation to

$$F_x = \int_0^{2\pi} -p(1)\cos(\alpha) r_a\, d\alpha \tag{2.4}$$

The only unknown in equation 2.4 is the pressure on the body's surface p. The pressure in unsteady flow can described by the unsteady Bernouilli equation, which can be derived from the Navier-Stokes momentum equation. Assuming inviscid flow, these reduce to the Euler equations. This reduced equation is shown for the flow in x-direction, denoted by u, but is reduced in y- and z-direction in the same way.

$$\frac{\partial u}{\partial t} + u\frac{\partial u}{\partial x} + v\frac{\partial u}{\partial y} + w\frac{\partial u}{\partial z} = F_{b,x} - \frac{\partial p}{\rho \partial x} \tag{2.5}$$

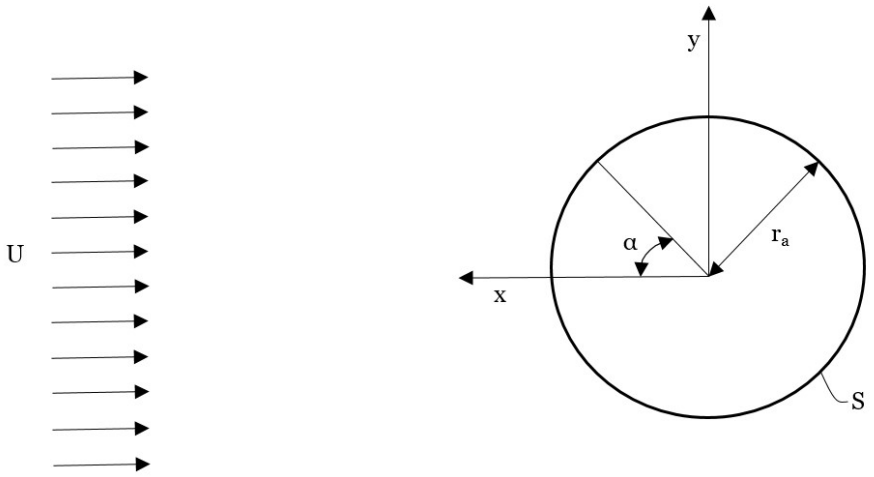

Figure 2.6: Parameters and symbols used to mathematically describe the forces on a cylinder in uniform flow.

When the flow is assumed irrotational, the rotation vector should be zero. Using this condition, the three Euler equations reduce to one equation,

$$\rho\frac{\partial\phi_p}{\partial t}+\frac{1}{2}\rho(u^2+v^2+w^2)+p-\psi=F(t) \tag{2.6}$$

in which ϕ_p is the velocity potential that satisfies $\mathbf{u}=\nabla\phi_p$. ψ are the body forces on the structure, for example gravity, which are assumed zero in this example. For conservative body forces, the equation is rewritten into

$$\rho\frac{\partial\phi_p}{\partial t}+\frac{1}{2}\rho|u_2|^2+p+\psi=p_\infty+\frac{1}{2}\rho u_1^2 \tag{2.7}$$

This equation assumes inviscid, incompressible and irrotational flow and is known as the unsteady Bernoulli equation along a streamline. Substituting equation 2.7 in equation 2.4 and neglecting differences in hydrostatic pressure results in

$$F_x=\int_0^{2\pi}\frac{1}{2}\rho(|u_2|-|u_1|^2)cos(\alpha)r_a d\alpha+\int_0^{2\pi}\rho\frac{\partial\phi}{\partial t}cos(\alpha)r_a d\alpha \tag{2.8}$$

The first part of this equation relates to the drag on the cylinder and the second part to the added mass. The equation can be solved if the flow pattern is known. For the cylinder in steady, potential flow the velocity field shows

$$U_r=U\cos(\alpha)\left(1-\frac{r_a^2}{r^2}\right) \tag{2.9}$$

$$U_\alpha=U\sin(\alpha)\left(-1-\frac{r_a^2}{r^2}\right) \tag{2.10}$$

$$\phi_p(r,\alpha)=U\cos(\alpha)\left(r+\frac{r_a^2}{r}\right) \tag{2.11}$$

with U_r the velocity in radial direction and U_α the velocity in tangential direction. And thus:

$$\begin{aligned}F_{it}=\int_0^{2\pi}r_a\rho\frac{\partial U}{\partial t}\left(r+\frac{r_a^2}{r}\right)\cos^2(\alpha)\,d\alpha\\ =2\pi r_a^2\rho\frac{\partial U}{\partial t}\end{aligned} \tag{2.12}$$

The drag is by definition related to the viscosity, which is absent for potential flow. Integrating the equation underneath results in zero if calculated over the entire circle; this is known as the D'Alembert paradox. However, the parameters to which the drag force on the body is related is of interest, so calculating F_d only over

-pi/2 tot pi/2 reveals the related quantities.

$$F_d = \int_{\pi/2}^{\pi/2} -\frac{1}{2}\rho\left(U^2 - (-2U\sin(\alpha))^2\right)\cos(\alpha) r_a \, d\alpha \\ = \frac{1}{3}\rho r_a U^2 \tag{2.13}$$

Finally, the drag force can be written in the following form, in which C_d represents the body shape- and viscosity related drag coefficient.

$$F_d = \frac{1}{2} C_d \rho D U^2 \tag{2.14}$$

The inertia force F_{it} can be rewritten in terms of a body-shape depending inertia coefficient C_m as well.

$$F_{it} = C_m \rho \pi r_a^2 \frac{dU}{dt} \tag{2.15}$$

Combining both terms gives the total, theoretical force on the body. C_m can be determined analytically for inviscid, irrotational flow.

$$F_x = C_m \rho A_0 \frac{dU}{dt} + \frac{1}{2} C_d \rho D U^2 \tag{2.16}$$

The inertia force F_{It} consists of a buoyancy part and a part due to entrainment of the fluid. The coefficient C_m is can therefore be split in $1 + C_a$, in which 1 relates to the buoyancy part and C_a to the added mass. The buoyancy part consists of a pressure gradient acting on the body due to the fluid's acceleration. This force is equal to the mass of the fluid displaced by the structure times the acceleration of the flow. It is therefore called a buoyancy force. The added mass component is the force due to entrainment of fluid by the body. The magnitude of the force depends on the acceleration of the flow, the fluid density and a body's shape. The body's shape is captured in the added mass coefficient C_a. The drag works in the opposite direction of the body's velocity. (Shafiee-far, 1997) (Blevins, 1990). (Sarpkaya and Isaacson, 1981)

2.2.3. Real loads on bluff bodies

Equation 2.16 is derived using potential flow theory and is assumed to be valid for laminar, unseparated flow. When flow separation occurs, time-dependent viscous hydrodynamic forces become important and their characteristics depend on the wake pattern around the bluff body (Ikeda, 1983). The analytically determined load coefficients in equation 2.16 are not valid any more, as is the equation itself, theoretically.
The drag coefficient may change due to shed vortices that add additional pressure gradients on the body. Besides that, the cyclic initiation of the generation of vortices may add additional loads on the bluff body (Sarpkaya and Isaacson, 1981).
Also the inertia coefficient is not necessarily equal to the potential flow load coefficient. The changes in the added mass are not a direct result of separation but originate from changes in the state of the flow.
Experimental studies showed that the equation can still describe sinusoidal loads on bluff bodies, if the load coefficients are adapted to account for the time-dependent viscous forces (Keulegan and Carpenter, 1958). Numerous experimental studies are executed to determine the load coefficients for various bodies with diverse edges under a range of sinusoidal loading conditions.

Sinusoidal flow around bluff bodies The first subsection showed that oscillatory flows are often found in offshore problems; waves cause an oscillating flow on structures and vessels are prone oscillating motions. An oscillating flow is often represented by a simple sine function. This implies that the loads on the body reverse direction every half cycle. Vortices may therefore be generated in alternating directions as well. Their sizes and strength depends among others on the frequency of oscillation. In oscillations with a small amplitude, vortices may not be shed, where in oscillations with a large amplitude a full Von Karman vortex street may be generated.

2.3. Establishment of the Morison model

Loads on oscillating bluff bodies are governed by separation of the flow and the formation of vortices. This makes it rather complex to calculate the loads on the body. Therefore calculation models are developed to

approximate these loads. The most commonly used model is the Morison model, which predicts the loads without describing the detailed, separated flow patterns. This section starts off with the derivation of the Morison model. Subsequently the load coefficients required in this model are derived by means of a Fourier analysis. Finally an extension of the Morison model is discussed, known as the Morison model with higher harmonics.

2.3.1. The Morison model for unsteady flow

The Morison model is established in 1950 as a model that approximates the forces on fixed cylinders in a time varying flow field. The model uses the undisturbed flow velocity and acceleration and geometry of the body. The latter is included by empirical coefficients. The model predicts the load with a two-coefficient Fourier fit, assuming higher order effects can be neglected. The strength of this model is its simplicity and convenience in use, as only load coefficients and the undisturbed flow description is required.
Although the prediction is a coarse approximation, research showed that loads on cylinders are predicted accurately (Tanaka *et al.*, 1982). Keulegan and Carpenter found this formula applicable to flat plates as well, although the accuracy of the prediction was significantly lower. Limitations in describing the exact force history were found as well as an underestimation of the peak force. The inclusion of higher order Fourier terms improved the accuracy. (Keulegan and Carpenter, 1958) (Van 't Veer *et al.*, 2012) (Sarpkaya and Storm, 1985)

Equation 2.16 shows the in-line forces on a body in steady flow. The undisturbed velocity $U(t)$ of a sinusoidally oscillating flow can be presented by:

$$U(t) = -U_m \cos(\omega t) \tag{2.17}$$

with U_m the maximum flow velocity during an oscillation cycle and ω the angular velocity in radians per second. The angular velocity is related with the oscillation period by $\omega = \frac{2\pi}{T}$. The time t is in seconds. The fluid acceleration is the time derivative of 2.17:

$$\frac{dU(t)}{dt} = \omega U_m \sin(\omega t) \tag{2.18}$$

The motion is expressed in terms of the maximum velocity per oscillation by:

$$x(t) = -\frac{U_m}{\omega} \sin(\omega t) \tag{2.19}$$

Equation 2.18 and 2.19 are both depending on the sine, although they have opposing signs. The inertia load acts in phase with the acceleration and is thus acting opposite to the motion. The velocity is described by a cosine term. The drag, related to the velocity $U(t)$, has a positive phase shift of $\frac{\pi}{2}$ compared to the motion. Compared to the inertia term, the drag has a phase lag of $\frac{\pi}{2}$. Expressing all equations in sine form, clearly shows the phase shifts relative to the motion:

$$\begin{aligned} x(t) &= -x_a \sin(\omega t) \\ U(t) &= -U_m \sin\left(\omega t + \frac{\pi}{2}\right) \\ \frac{dU(t)}{dt} &= -\omega U_m \sin(\omega t + \pi) \end{aligned} \tag{2.20}$$

The Morison model is obtained by substituting equation 2.17 and 2.18 in equation 2.16, which is principally designed for circular cylinders:

$$F_m(t) = C_m \rho V_0 U_m \omega sin(\omega t) + \frac{1}{2} C_d \rho A_s U_m^2 |cos(\omega t)| cos(\omega t) \tag{2.21}$$

In this equation A_s is substituted by V_0, the reference volume of the body, and D is substituted by A_s, the frontal area of the body. The force $F_m(t)$ is the in-line force on the cylinder. The equation can be written per unit body length by replacing A_s with the diameter D and V_0 with the sectional area.

2.3.2. Derivation of the load coefficients

For use of the Morison equation the drag- and inertia coefficients are required. Due to viscous flow separation, it is not possible to determine them analytically. Empirical studies are executed to determine them from

time traces of measured forces. This section elaborates the methods for deriving the coefficients from time traces. For periodic functions, a Fourier series expansion can be used as an approximation of the measured loads. The load coefficients C_m and C_d are related to the first two Fourier-coefficients. (Journée *et al.*, 2015) As the undisturbed flow velocity is periodic, the measured force is assumed periodic and symmetrical as well. Writing this assumption in a mathematical way shows (Keulegan and Carpenter, 1958):

$$F(\omega t) = -F(\omega t + \pi) \tag{2.22}$$

This symmetrical form implies that only the odd-numbered Fourier coefficients are taken into account for a Fourier-series expansion (Keulegan and Carpenter, 1958) (Journée *et al.*, 2015):

$$F = A_1 \sin\omega t + A_3 \sin 3\omega t + A_5 \sin 5\omega t + ... + B_1 \cos\omega t + B_3 \cos 3\omega t + B_5 \cos 5\omega t + ... \tag{2.23}$$

A_1 and B_1 are the first order terms and related to the inertia- respectively drag coefficient of the Morison equation. At the location of the dots in equation 2.23, higher order terms can be added. It is assumed that these have a minor influence and therefore ignored.

Obtaining the Fourier coefficients The two most used methods for determining the coefficients of equation 2.23 are time-averaging Fourier analysis and the method of Least Squares. The time-averaging Fourier analysis establishes the coefficients by evaluating the following integrals (Keulegan and Carpenter, 1958):

$$A_n = \frac{1}{\pi}\int_0^{2\pi} F \sin(n\omega t)\, dt \tag{2.24}$$

$$B_n = \frac{1}{\pi}\int_0^{2\pi} F \cos(n\omega t)\, dt \tag{2.25}$$

The method of Least Squares uses linear algebra to obtain the coefficients, through which it is convenient numerical method for large time traces. The method minimizes the difference S_{LSQR} between the assumed solution $f(A_1, B_1, A_3, B_3, A_5, B_5)$ and the measured load F. The length of the vector denoting the difference between the solution and the measured load is thereby diminished (Lay *et al.*, 2016):

$$S_{LSQR} \equiv \sum \left(F - f_i(a_1, b_1, a_3, b_3, a_5, b_5)\right)^2 \tag{2.26}$$

The expected form of the prediction function is required; this is the Fourier expansion of equation 2.23. A elaborated explanation of the algebraic steps used to obtain the 'least squares fit' is included in B.2. The input parameters for the Least Squares fit of the Fourier coefficients are described in section B.2.2.

Construction of the load coefficients To obtain the drag- and inertia coefficients as used in the Morison equation, the Fourier coefficients need a multiplication. The relation between the load coefficients and the Fourier coefficients is obtained by a comparison of equation 2.21 and equation 2.23. The relation between A_1 and the inertia coefficient follows directly from this comparison (Keulegan and Carpenter, 1958) :

$$C_m = \frac{A_1}{\rho V_0 U_m \omega} \tag{2.27}$$

The Morison equation is not equal to the 2-coefficient Fourier fit, as the Morison equation contains the $\cos(\omega t)|\cos(\omega t)|$ term in stead of a single cosine term. The Fourier coefficient B_1 therefore needs an additional correction to be consistent with the cosine term in the Morison equation. To determine this correction, $|cos(\omega t)|cos(\omega t)$ is replaced by itss Fourier series expansion. It is obtained from its inner product ratio (Keulegan and Carpenter, 1958) (Van 't Veer *et al.*, 2015):

$$\begin{aligned} |cos(\omega t)|cos(\omega t) &= \sum_{n=0}^{\infty} \frac{\int_0^{2\pi} |cos(\omega t)|cos(\omega t)cos(n\omega t)dt}{\int_0^{2\pi} cos^2(n\omega t)dt} \\ &= a_0 + a_1 cos(\omega t) + a_2 cos(2\omega t) + a_3 cos(3\omega t) + ... \end{aligned} \tag{2.28}$$

In this relation, the coefficients of the odd numbered n are defined by:

$$a_n = (-1)^{\frac{n+1}{2}} \frac{8}{n(n^2-4)\pi} \tag{2.29}$$

And thus $a_1 = \frac{8}{3\pi}$, $a_3 = \frac{8}{15\pi}$ and $a_5 = -\frac{8}{105\pi}$. The coefficients of all even numbered n are equal to zero. The equation $|\cos(\omega t)|\cos(\omega t) = a_1\cos(\omega t) + a_3\cos(3\omega t) + a_5\cos(5\omega t)$ is subsequently substituted into the desired form of the cosine part Morison equation $B_1'|\cos(\omega t)|\cos(\omega t) + B_3'\cos(3\omega t) + B_5'\cos(5\omega t)$. A corrected coefficient B_n' is used for B_n. This gives:

$$\begin{aligned} B_1'\big(a_1\cos(\omega t) + a_3\cos(3\omega t) + a_5\cos(5\omega t)\big) + B_3'\cos(3\omega t) + B_5'\cos(5\omega t) \\ = B_1' a_1 cos(\omega t) + (B_1' a_3 + B_3')cos(3\omega t) + (B_1' a_5 + B_5')]cos(5\omega t) \end{aligned} \tag{2.30}$$

The term $B_1' a_1$ should be equal to the B_1 term of the Fourier series expansion 2.23 and the term $B_1' a_3 + B_3'$ to B_3. The corrected coefficients are thus (Keulegan and Carpenter, 1958):

$$\begin{aligned} B_1' &= \frac{B_1}{a_1} = \frac{3\pi}{8}B_1 \\ B_3' &= B_3 - \frac{a_3}{a_1}B_1 = B_3 - \frac{1}{5}B_1 \\ B_5' &= B_5 - \frac{a_5}{a_1}B_1 = B_5 + \frac{1}{35}B_1 \end{aligned} \tag{2.31}$$

The drag coefficient as used in the Morison equation, equation 2.21, is thus related by Fourier coefficient B_1 by:

$$C_d = -\frac{3\pi}{4\rho A_0 U_m^2}B_1 \tag{2.32}$$

2.3.3. Morison model with higher harmonics

The 2-coefficient Morison model is very well applicable to cylinders (Keulegan and Carpenter, 1958) (Shafieefar, 1997). If the model is used for flat plates, the Morison model often underestimates the peak load (Keulegan and Carpenter, 1958) (Van 't Veer *et al.*, 2015). Keulegan and Carpenter (1958) found that the difference between the measured force and the force described by the 2-coefficient Morison equation is mainly a function of four higher order Fourier coefficients. Keulegan and Carpenter (1958) speaks of this as the 'remainder function':

$$\Delta R = a_3\sin(3\omega t) + B_3'\cos(3\omega t) + a_5\sin(5\omega t) + B_5'\cos(5\omega t) \tag{2.33}$$

The accuracy of the load prediction model can be increased by extending the Morison equation with this 'remainder part'. This function is shown underneath and throughout this thesis is will be referred to as the 6-coefficient Morison model:

$$\begin{aligned} F(t+\epsilon_m) = C_m\rho V_0 U_m\omega\sin(\omega t) + \frac{1}{2}C_d\rho A_0 U_m^2|\cos(\omega t)|\cos(\omega t) \\ + A_3\sin(3\omega t) + B_3'\cos(3\omega t) + A_5\sin(5\omega t) + B_5'\cos(5\omega t) \end{aligned} \tag{2.34}$$

In some cases, the Morison model could be used in its 4-coefficient format, which includes the coefficients C_m, C_d, a_3 and B_3' are used.

2.4. Experimental studies towards the load coefficients

For use of the Morison equation, the drag- and inertia coefficients of the body are required. Due to viscous flow separation, it is not possible to determine them analytically. The load coefficients found by Keulegan and Carpenter (1958), by Ridjanovic (1962) and by Tanaka *et al.* (1982) are of high interest for this study. The next subsections discusses them.

2.4.1. Load coefficients of infinite length flat plates

Keulegan and Carpenter (1958) did extensive experimental research to the load coefficients of cylinders and flat plates. The experiments were conducted in a water basin with a standing wave in which they placed cylinders and flat plates with their length nearly equal to the basin's width. The cylinders and flat plates are therefore regarded as of infinite length, through which the results considered for two-dimensional bodies. A schematic drawing of the test set-up is shown in figure 2.7a. Keulegan and Carpenter found that the magnitude of the load coefficients depends on the oscillation's frequency. They captured this frequency in the non-dimensional period parameter, which is afterwards named the Keulegan-Carpenter number:

$$KC = \frac{U_m T}{D} \tag{2.35}$$

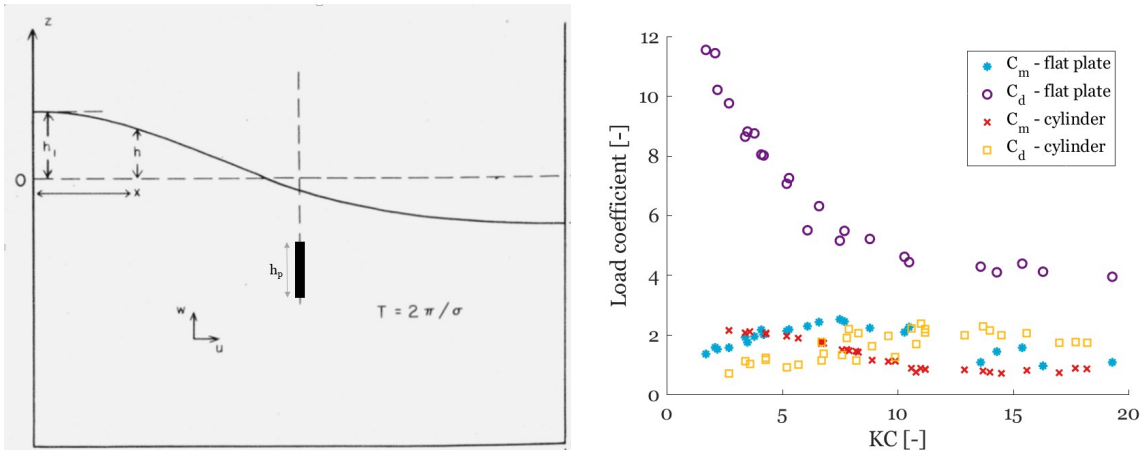

(a) Schematic test set-up of the experiments of Keulegan and Carpenter (1958). Adapted from Keulegan and Carpenter (1958).

(b) Drag coefficients of a flat plate and cylinder of infinite length, found by experimental research of Keulegan and Carpenter (1958)

Figure 2.7: Test set-up and results of the experimental tests by Keulegan and Carpenter (1958).

U_m is the maximum oscillation velocity, T the period of oscillation and D diameter of the cylinder of the plate's height h_p (Keulegan and Carpenter, 1958).

The tests were executed for a large range of KC numbers. Several cylinder- and flat plate models were used to account this large range. The results of the drag- and inertia coefficients are shown in figure 2.7b. This figure only shows the data for KC < 20, but Keulegan and Carpenter (1958) tested up till a KC number of 125. The load coefficients are defined as in equation 2.32 and 2.27.The graph shows that the drag on the flat plates drastically increases for decreasing KC numbers. The drag on the cylinder shows a more moderate course and has a maximum of approximately 2. The inertia coefficients of the cylinder increases towards a steady-state value of 2. The differences between the drag coefficients of the cylinder and the flat plate are explained by the formation of vortices. At small amplitudes, no vortices are generated around the cylinder. Around the sharp edges of the flat plate, vortices are always generated, resulting in a drastic drag coefficient increase.

2.4.2. Load coefficients of finite length flat plates

Ridjanovic (1962) tested flat plates with varying aspect ratios, defined as the plate length over the plate height, connected to a swinging pendulum. He obtained the drag on the plate by decay analysis by assuming that the dissipated energy per swing is a result of the drag acting on the plate. He ignored the fluids' mass inertia component. It is possible that the drag coefficients obtained by Ridjanovic are therefore found larger, as they may include a part of the inertia load as well. He defined the drag coefficient as:

$$C_{d,ridj} = \frac{-2F}{\rho h_p c U_m^2} \tag{2.36}$$

with c the width of the plate. A selection of his results are shown in figure 2.8. The KC number uses c as characteristic body length. The graph shows that for large KC numbers, the drag coefficient tends towards of 2. The drag of the low aspect ratio plates decrease more drastically than the high aspect ratio plates. Ridjanovic observed that the energy of a vortex generated by an oscillating plate is about 1.8 times larger than the energy of a vortex in a vortex trail.

Ridjanovic observed that flow separation took place around all edges. He concluded that the smaller the aspect ratio of the plate, the more energy is lost and the smaller the drag. This phenomenon is known as the 'end effects' of a body. The higher drag coefficients in oscillatory flow compared to steady flow is, according to Ridjanovic, due to the periodic formation of starting vortices and the partially formed wake. (Ridjanovic, 1962)

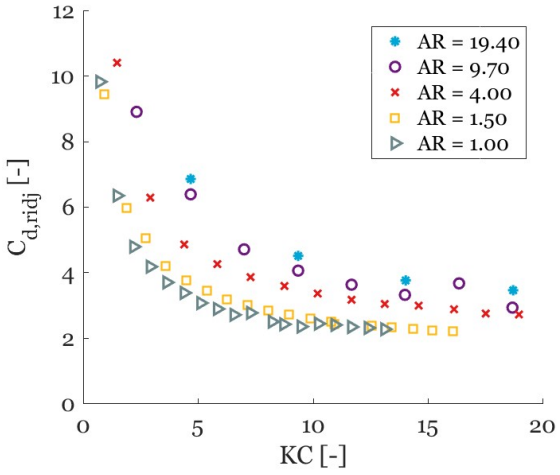

Figure 2.8: Drag coefficients of flat plates with different aspect ratios, found by Ridjanovic (1962).

2.4.3. Load coefficients cylindrical bodies & corner radii' influence

Research on oscillating cylindrical bodies is executed by Tanaka *et al.* (1982). Cylindrical bodies refer to round cylinders, squares and plates with various thickness. The two-dimensional bodies were oscillated horizontally in a water tank. The corner radii are varied moreover. Figure 2.9a and figure 2.9b show the load coefficients measured for plates with a thickness over plate ratio of 0.3 respectively 0.2. The corner radii of the plates are varied and defined by a ratio $2r/h$, in which r is the radius of curvature and h the height of the plate. The minimum ratio was 0, referring to a 90 degrees edge, and the maximum ratio defined an edge as a quarter circle of radius r.
Figure 2.9a shows the results of the thicker plate. The figure shows that the drag coefficient does not increase drastically for small KC-numbers, as observed for the flat plates of Keulegan and Carpenter (1958) and Ridjanovic (1962). The drag coefficient shows a similar trend as Keulegan and Carpenter's cylinder, but is somewhat larger in magnitude. Plate D, with a thickness over height ratio of 0.2, does follow the flat plate trends, but with a more moderate course. For both C and D, the plates with sharp edges have larger load coefficients than those with rounded edges.

Bearman (1984) studied cylindrical cylinders at the same moment as Tanaka *et al.* (1982). He tested two dimensional square cylinders with various corner radii, varying from a sharp edged cylinder to a circular cylinder. He found equal results as Tanaka *et al.* (1982); both the drag as the inertia coefficient decreased for an increasing rounding of the edge. He stated that due to the oscillatory flow, the wake is swept back around the body, which may lead to a fully turbulent fluid around the body. Further, he stated that turbulence delays separation. He suggests that a rounded edge causes the boundary layer to separate further downstream. (Bearman, 1984)

2.4.4. Research on oscillating bilge keels

FPSO's are prone to roll motions. Therefore, bilge keels are fitted to the hull to increase the roll damping. The bilge keels oscillate with the roll frequency of the ship and are often simple flat plates. This makes that the loads on bilge keels have similarities with the loads on the rudder. Several researches are executed to obtain insights in the flow behaviour around bilge keels and to predict the magnitude of the bilge keel damping. Ikeda *et al.* (1979) established an empirical equation to predict the drag coefficient of a bilge keel. The only variable in this equation is the KC number, in which he used twice the bilge keels' plate height (Ikeda *et al.*, 1979):

$$C_d = \frac{22.5}{KC} + 2.4 \tag{2.37}$$

Sarpkaya and O'Keefe (1996) executed research on oscillating flow around bilge keels as well. He tested both two- and three dimensional flat plates adjacent to a wall and tested a free plate for reference as well. The bilge keels had a higher drag coefficient than a similar sized free plate, especially at small amplitudes of oscillation.

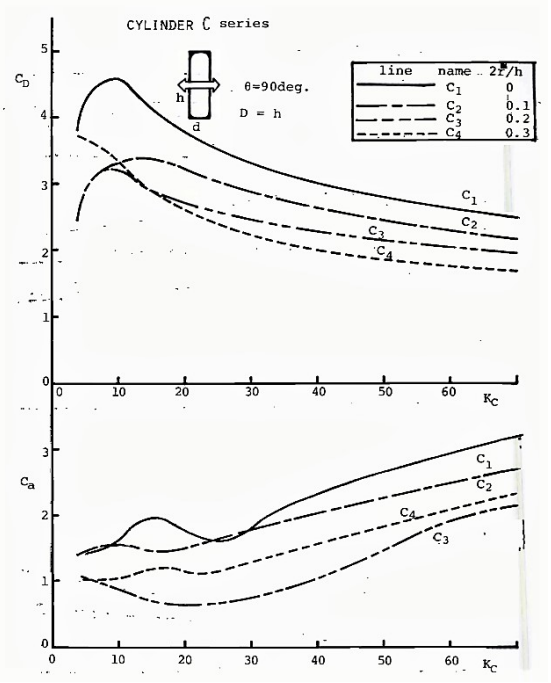

(a) Load coefficients of oscillating square cylinders with a thickness/height ratio of 0.3 and varying edge rounding, found by Tanaka *et al.* (1982).

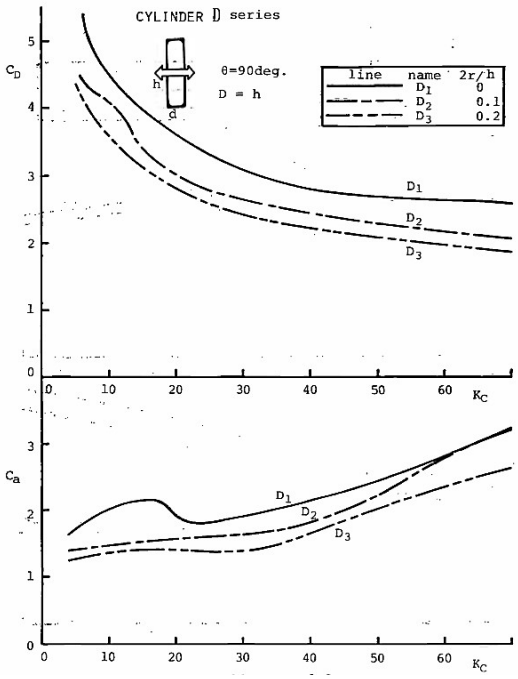

(b) Load coefficients of oscillating square cylinders with a thickness/height ratio of 0.2 and varying edge rounding, found by Tanaka *et al.* (1982).

Figure 2.9: Load coefficients of oscillating square cylinders, found by Tanaka *et al.* (1982).

They found that the wall acts as a symmetry plane for vortices. A bilge keel should therefore be treated as a free plate of twice the height of a bilge keel, defining the KC number by twice the plate height instead of once. The trend of the inertia coefficient showed a different behaviour as well. The trends are shown in 2.10. In these graphs, the coefficients of a infinite length bilge keel is presented, as well as two square bilge keels. The infinite length bilge keel shows a distinctively larger drag coefficient than the square bilge keels. Also the inertia coefficient is slightly larger.(Sarpkaya and O'Keefe, 1996)

In the past two decades, several researches are done on bilge keels at FPSO's, both experimentally as numerically. Van 't Veer *et al.* (2011) published a research in which model tests of two FPSOs in irregular waves were executed. A clear trend was found between the drag coefficient on the bilge keel and the KC number, which coincided with the empirical measurements on flat plate drag. Furthermore it was stated that the size and intensity of the detached vortex are good qualitative indication of the amount of roll damping. (Van 't Veer *et al.*, 2011)

2.4.5. Research on load prediction models for co-existing flow fields

Loads on offshore structures depend rarely of only wave or roll oscillations. Swaying of the ship or the presence of an offshore current can impose a steady flow on the model. This gives rise to a co-existing flow field: a flow combined of time-dependent oscillations and steady current. Superimposing the oscillating load and the steady load is not likely to give a good prediction model as the load on the rudder is governed by separating vortices (Sarpkaya and Isaacson, 1981). The separation is directly influenced by the ambient flow, so a combined flow field is likely to alter the loads. However, little research is done on bluff bodies in co-existing flow fields. The few studies executed are shortly mentioned hereafter and include studies to circular cylinders and bilge keels.

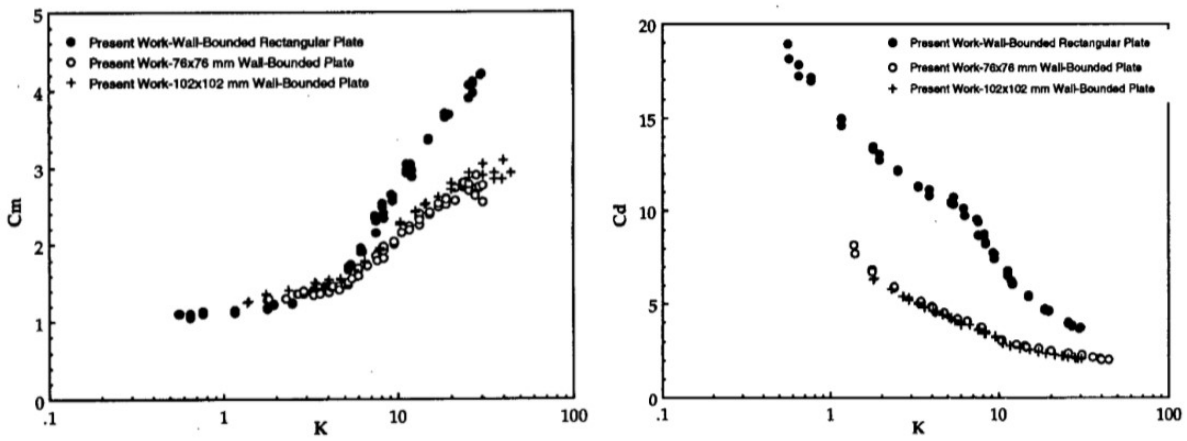

(a) Inertia coefficients of oscillating bilge keels, found by Sarpkaya and O'Keefe (1996).

(b) Drag coefficients of oscillating bilge keels, found by Sarpkaya and O'Keefe (1996).

Figure 2.10: Load coefficients of oscillating bilge keels, found by Sarpkaya and O'Keefe (1996).

Sarpkaya and Storm (1985) did research on the forces on a translating cylinder in an oscillating fluid. They adapted the Morison equation to describe the force-history (Sarpkaya and Storm, 1985):

$$F_{m,cur} = \rho C_{mc} A_0 \frac{dU}{dt} + 1/2 \rho C_{dc} D (V_c - U_m \cos(\omega t)) |V_c - U_m \cos(\omega t)| \tag{2.38}$$

This model is often referred to as the 'relative velocity' Morison model, as it does not superimpose the various flow fields, but captures these fields in a combined flow field. The force-history and the prediction by the 'relative velocity' Morison model for a smooth cylinder in low-speed current and a KC number of 12, is shown in figure 2.11. Sarpkaya and Storm (1985) found that the equation 2.38 describes the force well, but only if load coefficients obtained in non-zero current conditions, C_{mc} and C_{dc}, are used. Regarding these load coefficients, they found that the drag coefficient drops with increasing translating velocity and that the inertia coefficient increases. Furthermore they found that for KC < 30, the Morison drag equation is only applicable with load coefficients obtained in non-zero current conditions. For cases with KC > 30, the zero-current load coefficients can be used.

An extensive dissertation study on oscillating cylinders in a steady current is executed by Shafiee-far (1997). He compared a broad range of prediction models and found that only the 'relative velocity' Morison model shows a proper agreement with the force-history. 'Absolute velocity models', which take each velocity component separately into account, were misinterpreting the exact force history.

Ikeda *et al.* (2004) published a paper on the effects of steady flow on the vortex shedding of oscillating bilge keels. They found that, due to the steady flow, the drag on the bilge keel increased. Furthermore, the roll damping moment shows a non-symmetrical course over one oscillation and is not proportional to the roll angular velocity any more. The applicability of the Morison model is not directly assessed in this study.

2.4.6. Pressures in oscillating flows

In their research on bilge keel damping, Ikeda *et al.* (1979) measured the hull surface pressure created by bilge keels. They assumed that the pressures measured on the hull close to the bilge keels represented the pressure on the bilge keel surface as well. It was found that the pressure in front of the bilge keel was almost constant for different KC numbers. The pressure on the wake side of the bilge keel depended on the vortices shed and therefore the KC number. As the integrated pressure over both the front- and back side of the bilge keel is theoretically equal the normal force on the bilge keel, the following dependency was obtained (Ikeda *et al.*, 1979):

$$C_{p,d} = C^{+}_{p,d} - C^{-}_{p,d} \tag{2.39}$$

in which $C_{p,d}$ is the pressure coefficient and the + and − sign represents the bilge keels front- respectively wake-side. The coefficient $C^{+}_{p,d}$ approximated the constant value of 1.2. Ikeda *et al.* (1979) used the following

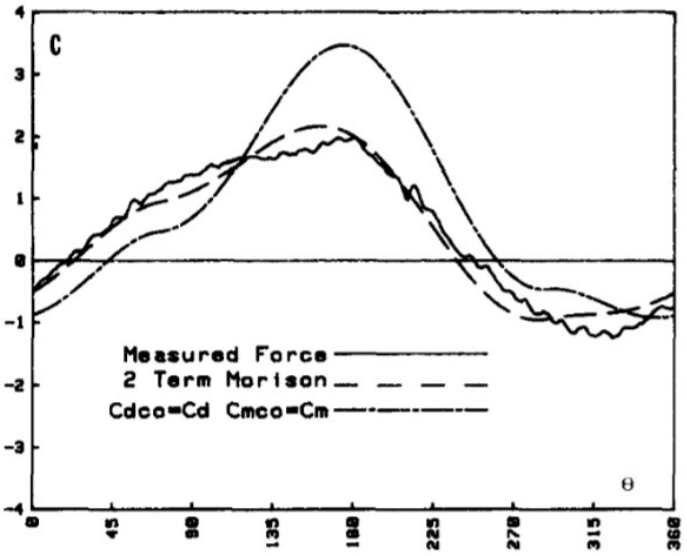

Figure 2.11: Force history and relative-velocity Morison's fits of a translating cylinder in oscillatory flow with KC=12.

definition for the pressure coefficient. He took the pressure P_d at the moment of maximum velocity U_m, so at the moment that the pressure is drag-dominated.

$$C_{p,d} = \frac{P_d}{1/2\rho U_m^2} \tag{2.40}$$

A similar definition for the inertia coefficient can be used. Ikeda did not take this coefficient in account, but it will be used in this way in this study.

$$C_{p,I} = \frac{P_I}{1/4\pi D\rho\omega U_m} \tag{2.41}$$

In this equation, P_I is the pressure at the maximum acceleration ωU_m. The relation is derived from $F_I = P_I \cdot A_0 = C_m \rho V_0 \omega U_m$, in which V_0 is the reference volume, set to $\frac{\pi D^2}{4} h$ and $A_0 = Dh$ the frontal area. The instantaneous inertia coefficient is defined as:

$$C_{p,m} = C_{p,I}^{+} - C_{p,I}^{-} \tag{2.42}$$

with $C_{p,I}^{+}$ the pressure coefficient at the front surface and $C_{p,I}^{-}$ the pressure coefficient at the wake side.

2.5. Knowledge gaps

The previous section discussed the current state of knowledge regarding the loads on oscillating bodies. According to this current state, knowledge gaps are identified. Many studies were executed to obtain the load coefficients of various bodies in oscillating motion. The quality of the Morison model was assessed in some studies as well. However, as stated in the first section of this chapter, the oscillating fluid load is not likely to have an uniform velocity profile over the rudder's span. No research on how to account for this varying, oscillating velocity distribution flow field is executed so far. It is expected that the steady current has a definite influence on the eddy-shedding behaviour. However, its influence on the rudder loads is unknown. The knowledge gaps are summarized below. They apply to both flat plates and lift profiles in an oscillating flow.

- Inertia coefficients are only known for two- and three edge separation and not for four edge separation.
- The influence on the loads on an object with a varying flow velocity and acceleration over its length is unknown.
- The free surface influence is unknown.
- The loads in a combined flow field of steady currents and oscillating flow are unknown.
- The possibilities of using a simple engineering model to estimate the oscillating loads including the influences listed above are unexplored.

2.6. Objectives

With the knowledge gap and the research goal, the research objectives are set and listed underneath.

- To quantify and explain the loads on the rudder in regular sway oscillation.
- To quantify and explain the loads on the rudder in regular sway oscillation and currents, acting perpendicular to the rudder's blade.
- To quantify and explain the loads on the rudder model in regular roll oscillation, with and without low-speed currents, acting perpendicular to the rudder's blade.
- To quantify and explain the loads on the rudder in a combined regular roll-sway oscillation.
- To analyse the influence of surface effects and oscillation frequency on the loads on the oscillating rudder model.
- To propose a load prediction model for a rudder in regular sway oscillation and include the required load coefficients.
- To propose a load prediction model for a rudder in an oscillation with a varying velocity magnitude over its span and include required load coefficients.
- To propose a load prediction model for a rudder in regular sway oscillation and current and include the required load coefficients.

3

Experimental method

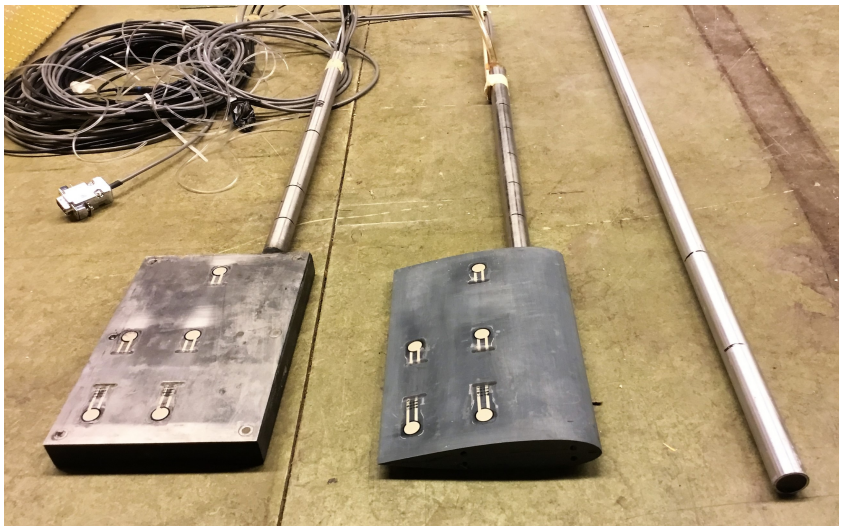

Figure 3.1: The models used for the experiments. Left: flat plate model. Mid: Lift profile. Right: 18 mm aluminium rod.

The objectives of this research consist of determining the loads on the rudder in sway- and in roll oscillation. The effect of current during this oscillation is analysed as well. To assess these objectives, towing tank experiments are executed. Oscillations in roll and sway are imposed by an hexapod underneath the towing tank's carriage. Currents are simulated by driving the carriage at constant speed. This chapter elaborates the set-up of the experiments. Consecutively, the models, the test facilities and the test matrix are discussed.

3.1. Description of the models

The experiments are executed with a rudder model only. This isolates the problem and reduces the complexity of the flow. The main advantage is the avoidance of hull radiation and diffraction, through which the undisturbed flow can be derived by a simple sinusoidal function. The presence of a known undisturbed flow makes it more feasible to draw generic conclusions. This is preferable, as hull diffraction- and radiation flow patterns vary ship by ship.

The research objectives consist among others of explaining the loads during oscillation. For this, in depth knowledge of the local flow is required. The rudder model is therefore fitted with membrane pressure sensors. These sensors require a significant amount of space inside the model. Due to this, the rudder model is designed as a thin, rectangular box. It is the left model of picture 3.1. The model is symmetric and has four identical edges. The amount of geometrical variables is thus limited. However, literature shows that loads on sharp edged models in in-plane oscillation are much higher than those on rounded edged models (Tanaka

Table 3.1: Main dimensions of flat plate model and lift profile. The stock location is the distance between the leading edge and the stock axis.

	Flat plate model	**Lift profile**
Thickness [mm]	20.0	25.2
Chord length [mm]	125	125.3
Stock location [mm]	31	31
Diameter pressure sensor hole [mm]	40.0	-

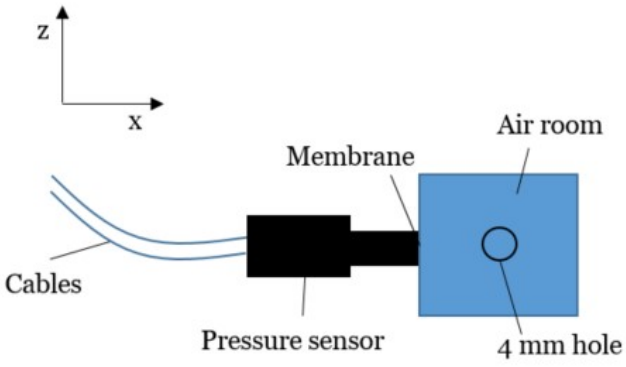

Figure 3.2: Schematic view of the membrane pressure sensor connected to the air-room

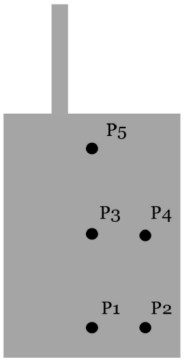

Figure 3.3: Numbering of the membrane pressure sensors

et al., 1982). The loads on a lift profile, which is a typical conversion FPSO rudder shape, might thus differ with the flat plate model. Therefore, a lift profile is tested to obtain a more reliable estimate of the forces. In this model, no membrane pressure sensors could be fitted.

Rudder geometries The main dimensions of the models are defined using four conversion FPSO's as reference. For confidential reasons, the dimensions of these ships are not included in this report. A height over chord ratio of 1.5 is used, as this is a common ratio for FPSO rudders and experimental validation data is available for this aspect ratio (Ridjanovic, 1962). The main dimensions of both models are shown in table 3.1. The thickness of the flat plate model is limited by the size of the membrane pressure sensors. A minimum thickness over chord length ratio of 0.2 was required for obtaining flat plate characteristics instead of box- or cylinder characteristics (Tanaka *et al.*, 1982). The flat plate model has a ratio of 0.16.

The NACA0020 shape is used as lift profile. For large, sea-going vessels, the NACA00 series tends to be the most standard shape (Molland and Turnock, 2007). The thickness varies between 15 to 25 percent of the chord length. Figure A.1 in appendix A.1 shows that the NACA0020 shape with a thickness over chord length ratio of 0.2 and the simplified rudder root contour of a conversion FPSO are in good agreement (Hyundai Heavy Industries, 2014) (Ladson *et al.*, 1996). The ordinates and shape equation of the NACA0020 shape are shown in appendix A.1. Drawings of the two models are included in appendix A.2, figure A.2a and A.2b.

Pressure sensors Five membrane pressure sensors of type PDCR 42 S/N 4432 are fitted in the flat plate model. The membrane connects to a small room with air. This room is in open connection to the surrounding water by a small hole with a diameter of 4.0 mm. These holes are visible in figure 3.3. The numbering of the sensors is also included in this figure. The most often used way to fit membrane pressure sensors in a ship model, is by placing the membranes in direct connection to the surrounding water. The use of a room with air might alter the measured loads slightly. Capillary effects can influence the measured pressure and the rooms may add a small damping term. The reason for using this set-up is the model's thickness. By using of a room, the sensor could be fitted parallel to the rudder's chord instead of perpendicular to the chord. This resulted in a model with a much smaller thickness.

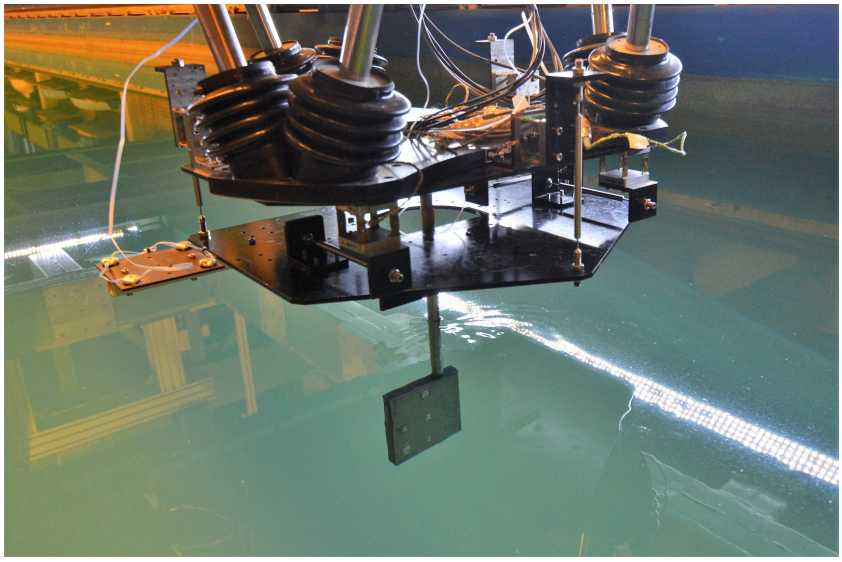

Figure 3.4: Flat plate model supported to six component frame underneath the Hexamove.

On both models piezoresistive point load cells, of type FlexiForce Standard A201, were glued as a try-out. Figure 3.1 shows the models with these additional sensors. Unfortunately the signals were not clear enough to include in this study. Most likely they failed due to a wrong gluing process.

The water tightness of the flat plate models is modelled by a humidity sensor. This sensor was fitted at the lowest point inside the model. A leakage can increase the mass of the model and, when it comes into contact with the pressure sensors, the resistance of the sensors may change. To monitor the water tightness of the models, a humidity sensor was fitted at the lowest point inside the model.

3.2. Description of the test facilities

The experiments are executed in towing tank no. 1 of the TU Delft. Oscillations of the model were imposed by an oscillator, called the Hexamove. The set-up of the experiment is shown in figure 3.4. The Hexamove can impose oscillations in all six degrees of freedom. These motions are measured with a Certus motion camera, which measures the location of four led lights on a plate connected to the model. This led light plate is the most left square plate on figure 3.4. Certus is calibrated prior to performing the tests. Specifications of the tank and the Hexamove are included in appendix A.3. Underneath the Hexamove, a frame is attached to measure the forces in all six degrees of freedom. To the lower plate of the frame, the model is fixed with a clamp that constrains the model vertically. A laser is used to align the model horizontally with respect to the measurement frame. A picture of this set-up is included in appendix A.4 figure A.3.

Six component frame The measurement frame underneath the oscillator is a six component frame. It consists of two horizontal plates, six load cells and connecting rods. The upper plate is connected to the oscillator's platform. Six load cells are connected to this upper plate. The connecting rods connect the load cells to the lower plate, to which the model is connected. Loads acting on the model and then transmitted to the lower plate of the six component frame, which transmits the loads via connecting rods to the load cells. The connecting rods transmit the loads in a specific direction, which is either x, y or z. A horizontal rod in x-direction transmits loads in x-direction, a horizontal rod in y-direction transmits the loads in y-direction and vertical rods connect to load cells that measure forces in the z-direction. The six load cells are fitted in such a way, that they measure the loads in all six degrees of freedom. The upper plate is assumed to have a rigid connection to the oscillator's platform. The alignment of the frame relative to the oscillation- and towing direction is measured by dragging the 18 mm aluminium rod through the tank. Rotating the frame for 0.65 degrees gave no forces in y-direction.

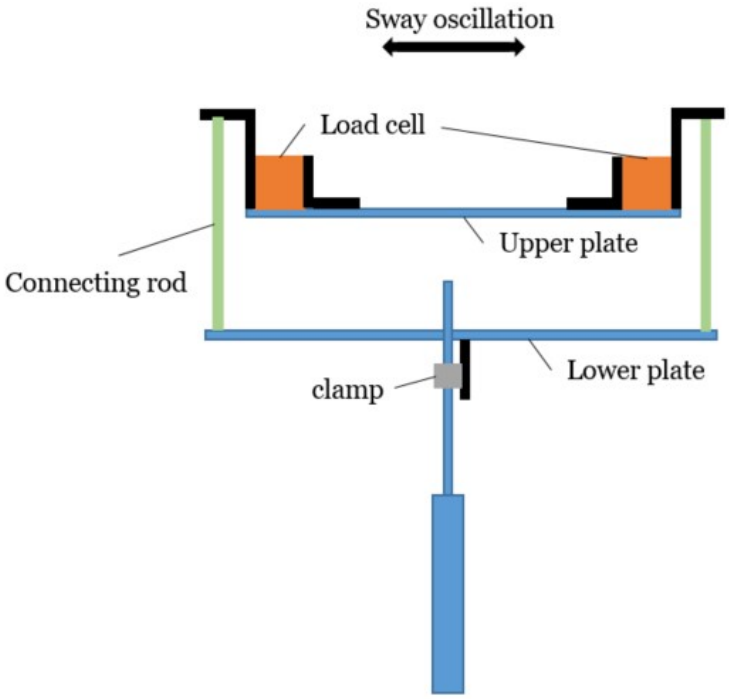

Figure 3.5: Graphic of the six component frame with two load cells in z-direction

Calibration of sensors The six load cells consist of two 5-kg load cells in x-direction and one 5-kg load cell in y-direction. In z-direction, three 10-kg load cells are used. They are calibrated by conventional means and contain a deviation between the calibration factor and the measured data of 0.5 percent at most. The hysteresis of the individual load cells was negligible. The membrane pressure sensors are calibrated with hydrostatic pressure tests. A deviation between the calibration factor and the measured data is 2.5 percent at most. A description of the calibration measurements in included in appendix A.5, as well as graphs describing the linearity of the sensors.

Signal processing All load cells and pressure sensors measure a voltage for every applied load. This is a very small and analogue signal. Therefore, all signals are amplified first and filtered at 100 Hz. Subsequently, they are sampled at 1000 Hz to convert the analogue signal into a digital one. The signals of the motion camera are sampled at 100 Hz.

3.3. Test matrix

The test matrix is shown in table 3.2. The loads in steady- and unsteady motion are measured in sway and roll motion. Roll-oscillations either used the rudder root as center of rotation (root-roll) or the ship's virtual center of gravity (CoG-roll). This virtual center of gravity is estimated 60 mm above the root, regarding geometries of reference FPSO's. The next paragraphs substantiate the choices made in the test matrix.

Roll oscillations With the roll oscillation experiment, the objective was to find the inertia- and drag coefficients for a non-uniformly undisturbed flow, and to verify if the Morison model is applicable for this undisturbed flow. Roll oscillations are executed around two points of rotation. A 'pure roll' situation is examined by rotating around the rudder's root. This roll oscillation is an academic set-up, as it is not likely to happen in reality. A more realistic case is roll oscillation around a virtual CoG. This oscillation consists of both a translation and a rotation for all points on the rudder blade. The results of both tests can be compared, and used to establish an engineering model that estimates the loads on a plate or rudder with varying KC numbers over the height of the plate.

Table 3.2: Test matrix

Oscillation mode	Frequency	Current velocity	Draught	**Flat plate** No. of amplitudes	**Lift profile** No. of amplitudes
Sway	0.31 Hz	-	237.5 mm	5 amplitudes	
		-	287.5 mm	3 amplitudes	
		-	337.5 mm	1 amplitude	
		-	387.5 mm	10 amplitudes	7 amplitudes
		0.06 m/s	387.5 mm	5 amplitudes	2 amplitudes
		0.11 m/s	387.5 mm	5 amplitudes	2 amplitudes
		0.17 m/s	387.5 mm	5 amplitudes	2 amplitudes
	0.62 Hz	-	287.5 mm	1 amplitude	
		0.06 m/s	387.5 mm		5 amplitudes
		0.11 m/s	387.5 mm		5 amplitudes
		0.17 m/s	387.5 mm		5 amplitudes
		-	387.5 mm	9 amplitudes	9 amplitudes
Root-roll	0.31 Hz	-	187.5 mm	1 amplitude	
		-	237.5 mm	5 amplitudes	5 amplitudes
		0.06 m/s	237.5 mm		5 amplitudes
		0.11 m/s	237.5 mm	4 amplitudes	5 amplitudes
		0.17 m/s	237.5 mm		5 amplitudes
		-	287.5 mm	2 amplitudes	
	0.62 Hz	-	237.5 mm		3 amplitudes
		0.06 m/s	237.5 mm		2 amplitudes
		0.11 m/s	237.5 mm		2 amplitudes
		0.17 m/s	237.5 mm		2 amplitudes
		-	287.5 mm	1 amplitude	
		0.11 m/s	287.5 mm	2 amplitudes	
CoG-roll	0.31 Hz	-	237.5 mm	6 amplitudes	5 amplitudes
		0.06 m/s	237.5 mm		1 amplitude
		0.11 m/s	237.5 mm		1 amplitude
		0.17 m/s	237.5 mm		1 amplitude
	0.62 Hz	-	237.5 mm		3 amplitudes
		0.06 m/s	237.5 mm		1 amplitude
		0.11 m/s	237.5 mm		1 amplitude
		0.17 m/s	237.5 mm		1 amplitude

Scaling The experiments are executed on scale. The model's dimensions, the current velocities and the oscillation frequencies are scaled with Froude scaling. This means that the Froude number is kept equal for both full- and model scale. The Froude number is defined by the undisturbed velocity divided by the square root of the gravitational constant times a characteristic body length. This implies that gravity is kept constant and that the fluid viscosity is not scaled properly. Experimental research showed that there is little or no effect of the Reynolds number, a measure of viscosity's influences (Keulegan and Carpenter, 1958). Therefore it is assumed that the improper scaled viscosity does not noticeably affect the results.
The model scale current velocities represent offshore currents of a maximum of three knots. The tests with current are limited to current directions perpendicular to the rudder plane. This is believed to be the harshest condition. Furthermore, in this condition the flat plate resistance, which is governed by viscosity, is negligible. The flat plate resistance due to currents that act on the rudder under an angle, the viscosity might not be neglected.

Oscillations' frequencies The tests are mainly executed at 0.62 Hz. This is a typical, scaled, natural frequency of roll for FPSO's. The natural period of roll of FPSO's varies between 11 and 16 seconds, which among others depends on their ballast condition. This period is moreover an often-occurring wave periods in the North Atlantic Ocean (International Association of Classification Societies, 2001). It is thus likely that vessels may encounter this frequency. Unfortunately, 0.62 Hz is a quite demanding frequency for the

oscillator, and not all amplitudes can be reached at this frequency. Therefore tests at 0.31 Hz are executed as well, as experimental research showed that the frequency of oscillation has minor or negligible influence on the dimensionless loads. This assumption is will be verified with experiments.

KC numbers' ranges A range of amplitudes is tested for every case, as a KC number dependency is foreseen. The general definition of the KC number is defined in equation 2.35. In this study, the models make sinusoidal motions. Therefore it is convenient to express the KC number in terms of the oscillation's amplitude. The maximum velocity in a cycle U_m is equal to the amplitude y_a times the angular velocity of the oscillation ω. The period T is equal to $\frac{2\pi}{\omega}$. For rudders, the chord length c is used as characteristic dimension. In sway motion, the KC-number can thus be defined as:

$$KC = \frac{2\pi \cdot y_a}{c} \tag{3.1}$$

In roll motion, it is convenient to rewrite the equation in terms of the roll amplitude. The maximum velocity of the model is during one cycle is equal to the roll amplitude ϕ_a times angular velocity ω times the distance between the center of rotation and the model's geometrical center r_d. Using this definition, the KC number is defined by:

$$KC = \frac{2\pi \cdot \phi_a \cdot r_d}{C} \tag{3.2}$$

The range of KC numbers should consist of number that can be encountered by a moored FPSO. The expected environmental conditions are therefore examined. Regarding the wave scatter diagram of the North Atlantic Ocean, the highest significant wave height is 16.5 m. The corresponding wave period is 11.5 seconds. The maximum expected wave height in a 3-hour storm condition is by a rule of thumb equal to 1.86 times the significant wave height. The maximum wave height is then 15.3 m. A rudder chord of 10 m, a dimension estimated from reference FPSO's dimensions, results in a KC number of 9.6. (Journée *et al.*, 2015) (Holthuijsen, 2007) (International Association of Classification Societies, 2001)
Waves combined with ship motions eventually result in higher KC numbers. Therefore, the maximum KC number would ideally be larger than the maximum KC number calculated by the expected wave occurrences. The range is limited by the oscillator's reach and the model's dimensions. In sway, amplitudes up to 250 mm can be reached. In roll the reach is up to 21°. The minimum used amplitudes are 10 mm for sway and 6° for roll. This equals KC numbers between 0.5 to 12.6 in sway and 0.8 to 2.8 in roll .

Draught variations Variations in draught are included to obtain insights in possible free surface effects. Most of the tests are executed at the largest draught to minimize the surface effects. For rotation, this maximum draught is smaller due to limitations of the oscillator. The free surface effects in roll are assumed smaller than in sway, as the model has no large motions near the surface. In this report, the draught will often referred to as 'the root's submergence', D_r. The dimension is defined as the distance between the root and the water level.

Duration of the tests Tests were performed for 180 seconds. The time between two subsequent tests depended on on the disturbance of the water; small oscillation amplitudes only caused little disturbances of the ambient water. When no waves were observed visually and no underwater waves were measured by the pressure sensors, a new test run was started. The time in between two subsequent tests varied from 3 to 20 minutes.

4

Signal corrections and uncertainties

The raw signals measured in the experiments need post-processing. The signals are first filtered. The filtering method is explained in section 4.1. Thereafter, the force signals are corrected for the mass inertia and hydrodynamic loads of the rudder stock. This is explained in section 4.2. Section 4.3 presents the corrections of the pressure signal. The last section of this chapter discusses the uncertainties of the experiments.

4.1. Signals' post-processing

The load signals contain significant noise and are therefore filtered with a Butterworth filter. Graphs of the normalized spectral density of load cell 2 and pressure sensor 3 are shown in figure 4.1. The signal of the load cell mainly contains high frequency noise. The pressure sensor's signals shows a small energy peak around a frequency of 7 Hz. Besides high frequency noise, low frequency noise may be present too. This can be caused by low frequent waves in the tank, which may especially be present at the end of a test day or -week. The high frequency bound is 7 Hz, the low frequency bound 0.06 Hz. The signals of the motion camera are filtered with a Butterworth low-pass filter. These signals did not contain noise, but occasionally showed small discrepancies. The signals were filtered at 1 Hz. A detailed explanation of the Butterworth filter is included in appendix B.1.

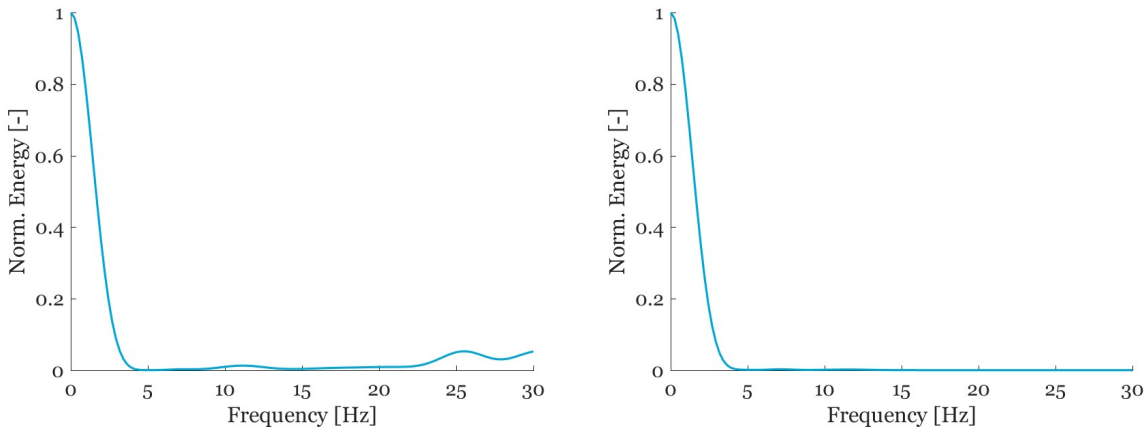

(a) Normalized spectral density of load cell F2 at 0.31 Hz 100 mm oscillation.

(b) Normalized spectral density of sensor P3 at 0.31 Hz 100 mm oscillation.

Figure 4.1: Normalized spectral density.

The method of Least Squares is a calculation method to find the 'best fit' solution for a mathematical problem. This method is used in this study to calculate the Fourier coefficients and to correct for the phase of the model's oscillation. In appendix B.2.1, the method of Least Squares is elaborated.

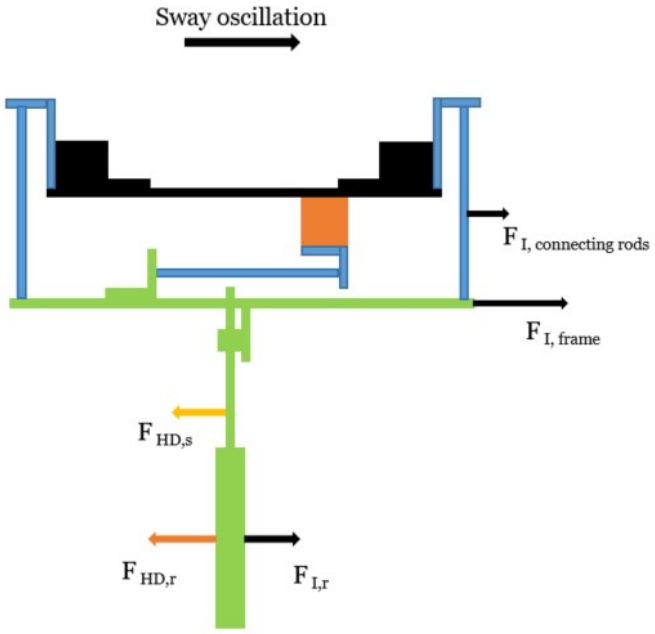

Figure 4.2: Schematic view of all loads measured by a load cell in sway direction

4.2. Force corrections

In the experimental set-up the rudder and the six component frame itself are oscillated. By Newtons second law, a mass inertia force is therefore acting on the oscillated body. This force is the same force as experienced when sitting in a accelerating or braking car. The magnitude of this force depends on the mass of the body and the acceleration magnitude. The Morison equation only accounts for the hydrodynamic loads on the body. The mass inertia loads are thus be subtracted from the measured loads first. This accounts for both the sway- and the roll motion, although the corrections are not the same for both oscillation types. The mass inertia correction in sway motion is described in subsection 4.2.1 and the correction in roll motion in subsection 4.2.2. Furthermore, hydrodynamic loads are acting on the rudder stock. Although these loads may be present in real conditions, a correction is desired to compare experiments at different draughts and to validate the results with other experimental studies. The correction method of the rudder stock is described in subsection 4.2.3.

A schematic view of the test set-up and the forces acting on it is shown in figure 4.2. Is shows the forces when the model decelerates. The conceptual force components are written in equation 4.1. In order to capture the hydrodynamic forces acting on the rudder, $F_{HD,r}$, the signal of the load cells F_{signal} is corrected with the mass inertia force $F_{I,b}$ and the hydrodynamic loads of the rudder stock $F_{HD,s}$. The mass inertia force $F_{I,b}$ is composed of the terms $F_{I,r}$, $F_{I,frame}$ and $F_{I,connectingrods}$ shown in figure 4.2.

$$F_{signal} = F_{HD,r} - F_{I,b} + F_{HD,s} \tag{4.1}$$

4.2.1. Mass inertia loads in sway oscillation

According to Newtons second law, the mass inertia force is a function of the body mass and its acceleration. The mass inertia force $F_{I,b}$ can therefore be described by equation 4.2:

$$F_{I,b2} = m_{eq2} \cdot \ddot{y} \tag{4.2}$$

in which $\ddot{y}$ is the body's acceleration and m_{eq2} the equivalent mass of the body. The subscript 2 denotes that sway oscillation is considered. An equivalent mass is used instead of the real body mass, because the accelerating mass is not completely equal to the total mass of the frame. Figure 4.2 shows parts of the set-up in green, blue and black. This is a schematic view of the different masses and their assumed contribution to the mass

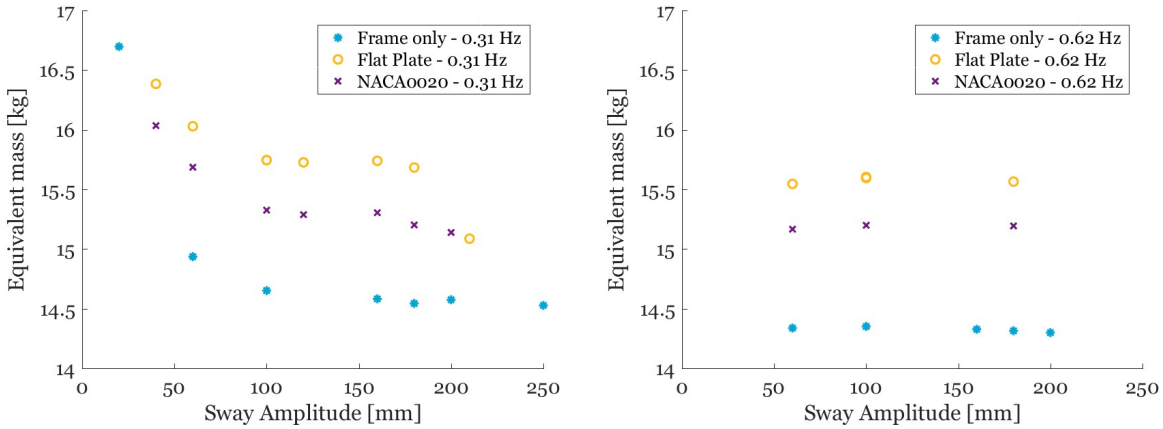

(a) Equivalent masses of models and frame in sway oscillation at 0.31 Hz

(b) Equivalent masses of models and frame in sway oscillation at 0.62 Hz.

Figure 4.3: Equivalent masses of the six component frame only, the frame with flat plate model and the frame with the lift profile

inertia force. The green parts are assumed to fully contribute to the mass inertia force. The connecting rods and parts connecting to the load cells, shown in blue, are not surely contributing to the mass inertia force. Another factor that may cause deviations between the equivalent mass and the absolute mass are swinging of cables. To obtain the equivalent mass, oscillations in air in air are executed. They include oscillations with the six component frame only, the flat plate model and the lift profile at both 0.31 Hz and 0.62 Hz for a range of amplitudes.

In air, drag is assumed nil. Therefore the measured force is expected to be in-phase with the acceleration:

$$F_{I,b2} = -m_{eq2} \cdot y_a \omega^2 \sin(\omega t) \tag{4.3}$$

To verify this assumption, the measured loads are fitted to a sine- and cosine component:

$$F_{I,b2}(t) = A_{I,b2} \sin(\omega t) + B_{I,b2} \cos(\omega t) \tag{4.4}$$

The coefficients $A_{I,b2}$ and $B_{I,b2}$ are obtained with the Least Squares method. The coefficients $A_{I,b2}$ and $B_{I,b2}$ are included in appendix C, figure C.5 and C.6. The coefficient $A_{I,b2}$ shows a nearly linear trend. The coefficient $B_{I,b2}$ shows a large scatter for both frequencies and is at most 5 percent of $A_{I,b2}$. Due to the large scatter and small magnitude, the drag term is neglected. The measured force is thus congruent with its expected form shown in equation 4.3. The equivalent mass is subsequently derived by dividing $A_{I,b2}$ by the acceleration's amplitude $y_a \omega^2$:

$$m_{eq2} = \frac{A_{I,b2}}{y_a \omega^2} \tag{4.5}$$

Figure 4.3a and figure 4.3b show the equivalent masses in 0..31 Hz respectively 0.62 Hz oscillations. The figures show that for amplitudes larger than 60 mm, the equivalent masses are nearly constant. Furthermore, the figures show that the equivalent masses deviate slightly for the two frequencies. At 0.62 Hz the mean equivalent mass is 0.2 kg lighter. It is expected that the measurements at 0.62 are more accurate, as the loads are higher and the load cells are therefore loaded in their midrange which lowers their noise-to-signal ratio. In appendix C two inertia runs are included. Figure C.1 shows the load F_y for a 0.31 Hz oscillation with an amplitude of 20 mm. Figure C.2 shows a 0.62 Hz run with an amplitude of 250 mm. The noise to signal ratio's differ significantly. In these graphs, two mass inertia fits are plotted as well. One fit has an equivalent mass of 14.3 kg and the other a mass of 14.6. The differences of the fits are marginal and one can easily observe that both lines fit the 0.31 Hz oscillation equally well. The 0.62 Hz equivalent masses are therefore used.

The equivalent masses are 14.3 kg for the measurement frame only, 15.2 kg for the lift profile and 15.6 kg for the flat plate model. The differences between the masses are by approximation similar to the measured weights of the models, which are 0.8 kg respectively 1.2 kg. The cables above the end of the stock are not taken into account in this measurement, but they can add a some weight as well.

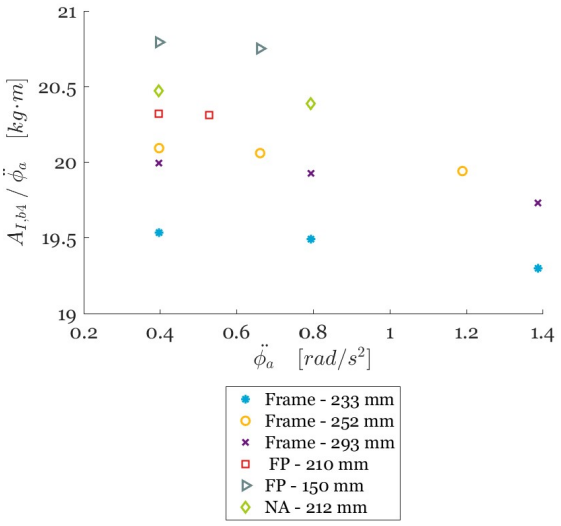

(a) $A_{I,b4}/\ddot{\phi}_a$ of load cell 2 in 0.31 Hz oscillation.

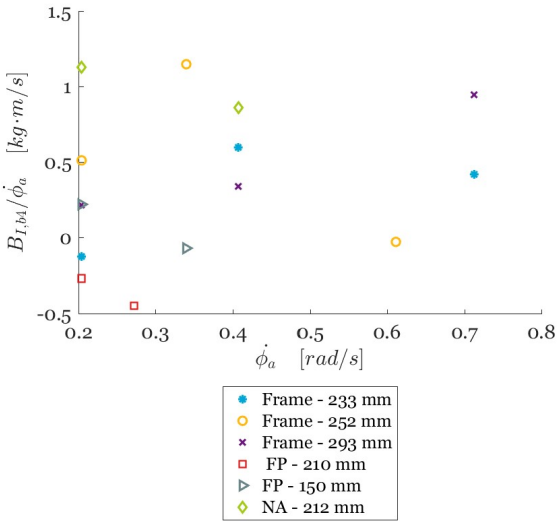

(b) $B_{I,b4}/\dot{\phi}_a$ of load cell 2 in 0.31 Hz oscillation.

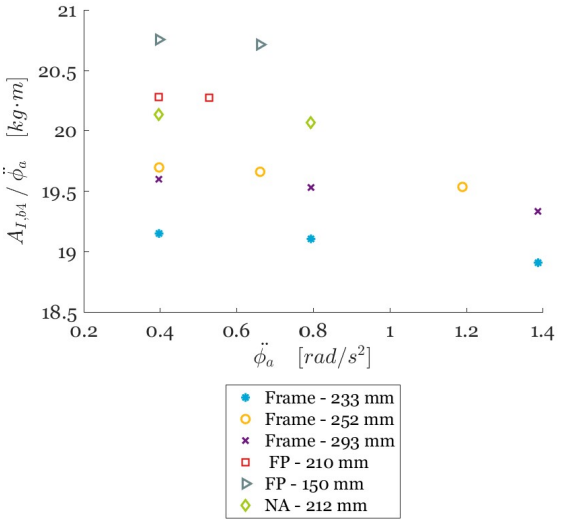

(c) $A_{I,b4}/\ddot{\phi}_a$ of load cell 2 in 0.31 Hz oscillation

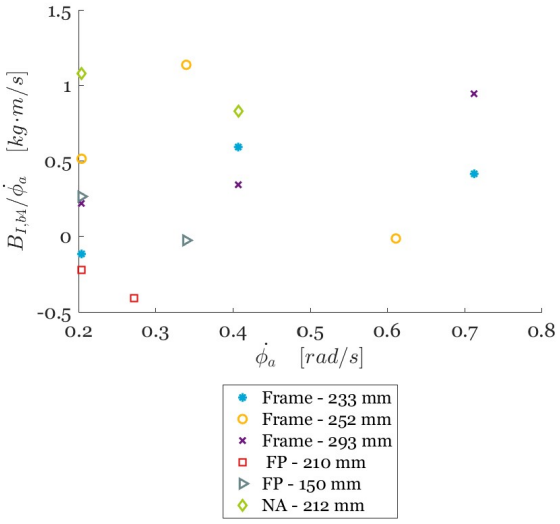

(d) $B_{I,b4}/\dot{\phi}_a$ of load cell 3 in 0.31 Hz oscillation

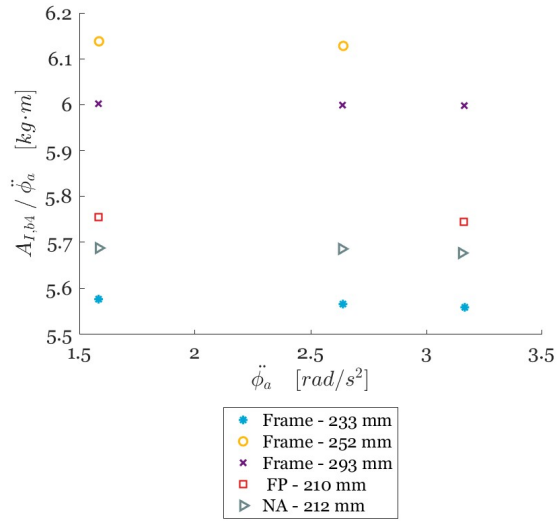

(e) $A_{I,b4}/\ddot{\phi}_a$ of load cell 2 in 0.31 Hz oscillation

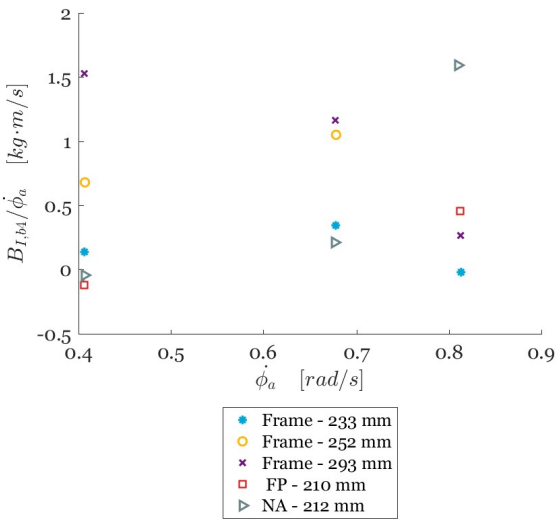

(f) $B_{I,b4}/\dot{\phi}_a$ of load cell 2 in 0.62 Hz oscillation

Figure 4.4: Results of roll oscillations in air of the six component frame, the frame with flat plate model and the frame with the lift profile

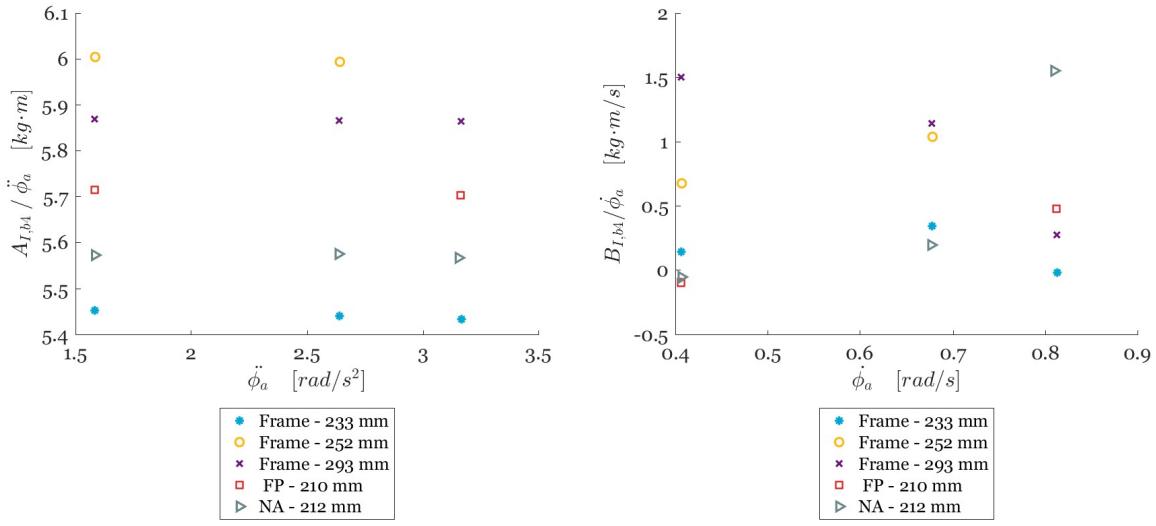

(a) $A_{I,b4}/\ddot{\phi}_a$ of load cell 3 in 0.62 Hz oscillation

(b) $B_{I,b4}/\dot{\phi}_a$ of load cell 3 in 0.62 Hz oscillation

Figure 4.5: Results of roll oscillations in air of the six component frame, the frame with flat plate model and the frame with the lift profile

4.2.2. Inertia loads in roll oscillation

The roll oscillations are executed by rolling the oscillators platform, the model and the frame around an arbitrary Center of Rotation (CoR). Also for this oscillation type, mass inertia forces are important and are subtracted from the measured force. The most straightforward way to do so, is by distracting the loads per individual load cell. This approach uses the 'body-bound' coordinate system, a coordinate system that rotates with the frame or model. For this research the forces in the body-bound system are of interests, as the loads are predicted for locking the rudder machine. However, gravity and buoyancy forces are static forces that always act in the 'earth-bound' z-direction. Depending on the instantaneous roll angle, these forces are thus partly measured by load cells in z-direction and in y-direction.
The buoyancy force is not measured for oscillations in air, and can thus not be subtracted directly with the air measurements. The static buoyancy force is equal to the submerged volume of the body times the density of the water times the gravitational constant. For the flat plate, this is 4.7 N. This is 3 percent of the mass inertia force, $15.6 \cdot 9.81 = 153$. The influence of the varying buoyancy force over the roll angle is therefore neglected. It is thus possible to correct the mass inertia correction in the body-bound coordinate system.

Roll oscillations in air are executed for a range of amplitudes and for different CoR's. Oscillations are executed with the six component frame only and the frame with one of the models attached to it. The load cells measuring the inertia loads in y-direction showed clear sinusoidal signals. Their amplitude and phase are determined with the method of Least Squares:

$$F_{I,b4} = A_{I,b4} \sin(\omega t) + B_{I,b4} \cos(\omega t) \tag{4.6}$$

In rigid body dynamics, the force in y-direction due to rotation around the x-axis is known as the tangential acceleration of mass. One can write this into:

$$\begin{aligned} F_{I,b4} &= m_{eq4} \ddot{y} \\ &= m_{eq4} d_m \ddot{\phi} \\ &= m_{eq4} d_m \phi_a \omega^2 \sin(\omega t + \epsilon_{I,b4}) \end{aligned} \tag{4.7}$$

with m_{eq4} the equivalent mass in x-direction during the roll oscillation and d_m the distance between the center of mass and the center of rotation. $A_{I,b4}$ is thus equal to $m_{eq4} d_m \phi_a \omega^2$, so dividing $A_{I,b4}$ by $\phi_a \omega^2$ gives $m_{eq4} d_m$ with unit $kg \cdot m$, a parameter that should be constant. Figure 4.4a and 4.4e show $A_{I,b4}/\ddot{\phi}_a$ in 0.31 Hz respectively 0.62 Hz oscillation for load cell 2, figure 4.4c and 4.5a for load cell 3.
These figures show that $A_{I,b4}/\ddot{\phi}_a$ is approximately constant over the range of angular velocities. However, a

variation of the magnitude of the parameter is observed for the different models and the different CoR's. For the frame-only measurements at 0.31 Hz, $A_{I,b4}/\ddot{\phi}_a$ of load cell 2 is the lowest for the the smallest distance between the oscillator's platform and the CoR, followed by the largest distance and subsequently the intermediate distance. No explanation can be found for this observation and therefore no clear trend between the models' masses and CoR's can be derived.
The amplitude of the cosine term of equation 4.8 divided by the angular velocity $B_{I,b4}/\dot{\phi}_a$ is shown in figure 4.4b and 4.4f for load cell 2 and in figure 4.4d and 4.5b for load cell 3. The results are scattered between -0.5 and 1.2 $kg \cdot m/s$. No trend is distinguished for these results.

As no clear equivalent inertia parameter could be established for roll oscillations, the experiments are the lowest and highest obtained values. These are equal to 18.9 respectively 20.8 $kg \cdot m$ for $A_{I,b4}/\ddot{\phi}_a$ and -0.5 respectively 1.2 $kg \cdot m/s$ for $B_{I,b4}/\dot{\phi}_a$. For both load cells in y-direction, the same values are found. The influence of this spread is discussed in section 4.4.3.

4.2.3. Rudder stock loads

The supporting arm or 'rudder stock' adds an hydrodynamic load to the total load and is preferably subtracted. Oscillation experiments are executed with an aluminium rod of the same diameter as the rudder stocks of the models. Sarpkaya and Isaacson (1981) and Keulegan and Carpenter (1958) describe the hydrodynamic loads on a circular cylinder with the 2-coefficient Morison model. A simplified model on this is used here:

$$F_{HD,s} = A_{HD,s} \sin(\omega t) + B_{HD,s} \cos(\omega t) \tag{4.8}$$

For a 0.31 Hz oscillation at 200 mm draught, the measured loads are governed by mass inertia loads. The load cells were not sensitive enough to measure the drag component properly. As the acceleration-depended terms showed some results, this term - the added mass term - is taken into account only. The rudder stock loads is thus simplified by:

$$F_{HD,s} = m_a \cdot \ddot{y} \tag{4.9}$$

The added mass is often expressed as a function of the displacement V_{rod} and the water density ρ (Sarpkaya and Isaacson, 1981):

$$m_a = C_m \cdot \rho \cdot V_{rod} \tag{4.10}$$

in which C_m is the inertia coefficient of the cylinder. Several empirical studies found inertia coefficients fluctuating around 2 for KC numbers between 0 and 15 (Keulegan and Carpenter, 1958) (Tanaka *et al.*, 1982). The best fit of the inertia coefficient of the experiments in this study is $C_m = 6$. This is higher than the coefficients found in literature. The total force due to this component is still small, so the higher value can be caused by inaccurate measurement equipment. An inertia coefficient of 6 accounts for an added mass of 0.3 kg for a draught of 200 mm.

In sway oscillation, the influence of the hydrodynamic rudder stock loads is thus very minor, although small waves were visibly generated during the oscillations. The rod is also oscillated in roll oscillation, at 50 mm and 100 mm draught. No visible waves were generated. As the influence of the hydrodynamic rods in sway oscillation were little, the hydrodynamic loads on the rod in roll oscillation neglected.

4.3. Pressure signal corrections

The hydrostatic pressure varies in roll oscillation over the oscillation cycle. Therefore, the measured pressures need corrections. The hydrostatic pressure is determined by the water column height above the sensor times the water density times the gravitational constant. The varying water column is equal to the distance between the sensor and the CoR, $d_{|Pn-CoR|}$, times the cosine of the time-depending roll amplitude. The time-varying hydrostatic pressure is thus:

$$\Delta p_{hs}(t) = \left(d_{|Pn-CoR|} - d_{|Pn-CoR|} \cdot \cos(\phi(t))\right) \rho \cdot g \tag{4.11}$$

$\Delta p_{hs}(t)$ is added to the pressure signal, as this signal is corrected for the mean pressure in its mid-position. The signal and corrected signal of sensor P3 for a 0.31 Hz root-roll oscillation with 14° amplitude is shown in figure 4.6a. The corrected signal is still a double frequent signal. This behaviour is not as expected and is also observed for the other sensors and in the other tests as well. Besides that, the noise of the pressure signals in

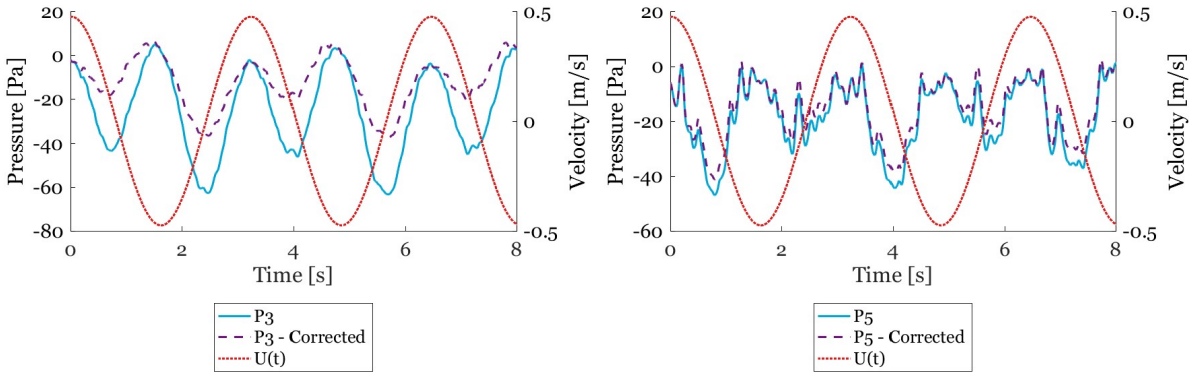

(a) P3 in 0.31 Hz root-roll with 14° amplitude.

(b) P5 in 0.31 Hz root-roll with 14° amplitude.

Figure 4.6: Pressure signals in roll oscillation and their hydrostatic correction attempt.

roll oscillation is significant, as the distances travelled in y-direction by the pressure sensors were very little compared to the swaying oscillations. Figure 4.6b shows the signal of P5. This signal contains more noise as the undisturbed velocity is even smaller near the root. It is not known if the observed double frequent signal is a result of the high noise grade, faults in the post-processing of the hydrostatic pressure or has a different source. The signals cannot be used for further analysis.

4.4. Uncertainty Analysis

For the validation of the experiments, it is important to make an estimate of the uncertainty of the experiments. For these experiments, the influence of the uncertainty on the load coefficients is of importance. The standard method of examining the uncertainty is via the ITTC 2008 regulation for planar motions. This method is used as a guideline, but in this section only the practical outcomes, the uncertainties of the load coefficients, are included.

4.4.1. Influence of the time traces' length

The force signals of two runs at 0.62 Hz oscillation with an amplitude of 60 mm are shown in figure 4.7. The signals are both filtered first and subsequently corrected for the mass inertia of the six component frame and the model. In both graphs, the tops and troughs are encircled. The circles indicate a significant variation in the tops and troughs over the time. This variation can be quantified by the standard deviation. Eleven runs of 100 mm sway oscillation at 0.31 Hz are executed. The standard deviation of their tops and troughs is calculated with the following equation:

$$\sigma = \sqrt{\frac{(F_{i,peak} - F_{mean,peak})^2}{N_{peak} - 1}} \tag{4.12}$$

in which N is the number of input arguments, in this case the tops and troughs. The eleven runs all have a duration of 160 seconds. When the entire time trace was used to calculate the standard deviation, the standard deviation was larger than when only the first 80 seconds were used. This indicates an increasing inaccuracy over the time. A larger amount of input arguments with a similar accuracy should cause a decrease of the standard deviation. The inconsistency of the signal can be caused by the disturbances of the water or diffractions against the towing-tank's walls. Therefore, only the first 80 seconds of the signals will be used in the data analysis.

4.4.2. Variation of load coefficients

The load coefficients of all repeat runs are determined and compared. This gives a practical way of assessing the measurement accuracy's influence on the load coefficients. Figure 4.7a and figure 4.7b show the results of identical oscillations. Their mean peak height varies, it is 2.65 respectively 2.76. Figure 4.8a shows 10 seconds of the force histories of both runs. The graph clearly shows that the signal of run 898 has larger

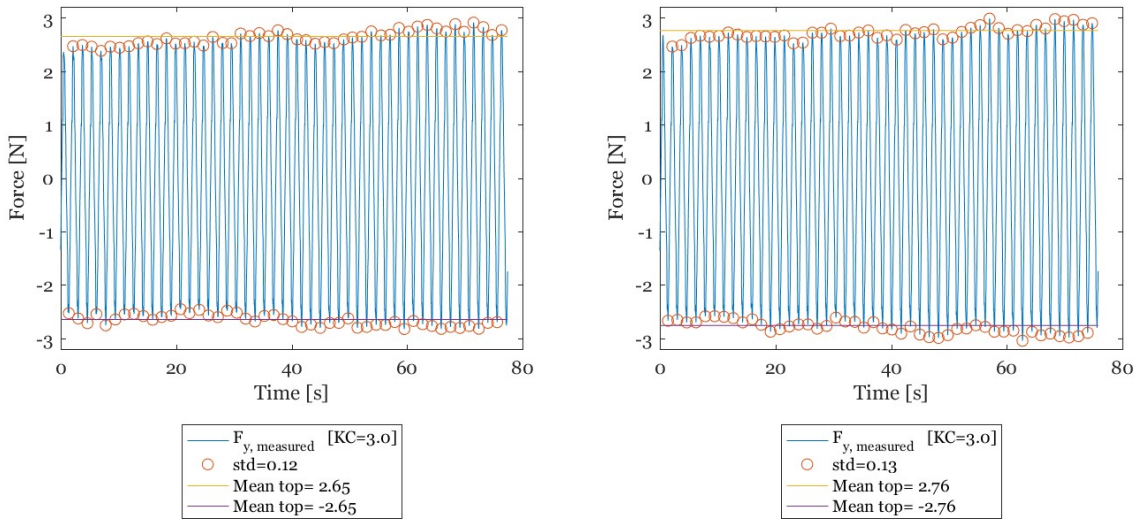

(a) Run 736: deviation of sway load's tops and troughs, filtered at 7 Hz

(b) Run 898: deviation of sway load's tops and troughs, filtered at 7 Hz

Figure 4.7: Deviation of sway load's tops and troughs of two similar runs.

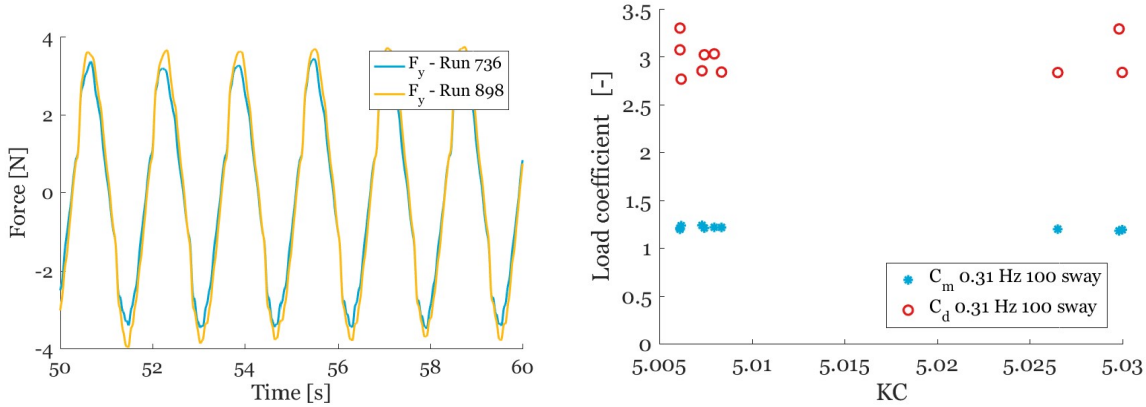

(a) Force history comparison of run 736 and 898.

(b) Load coefficients of eleven 100 mm amplitude 0.31 Hz repeat runs.

Figure 4.8: Visualisation of measurement accuracy: comparing repeat runs.

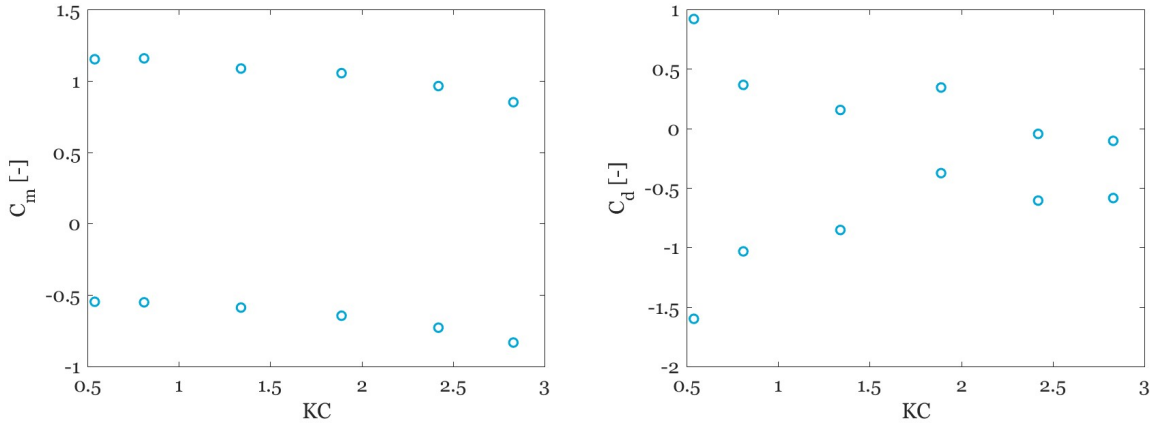

(a) Spread of the flat plate's inertia coefficient in CoG-roll at 0.31 Hz with $A_{I,b4}/\ddot{\phi}_a$ varying from 18.9 to 20.8 $kg \cdot m$

(b) Spread of flat plate's drag coefficient in CoG-roll at 0.31 Hz with $B_{I,b4}/\ddot{\phi}_a$ varying from -0.5 to 1.2 $kg \cdot m/s$

Figure 4.9: Spread in load coefficients in roll oscillation

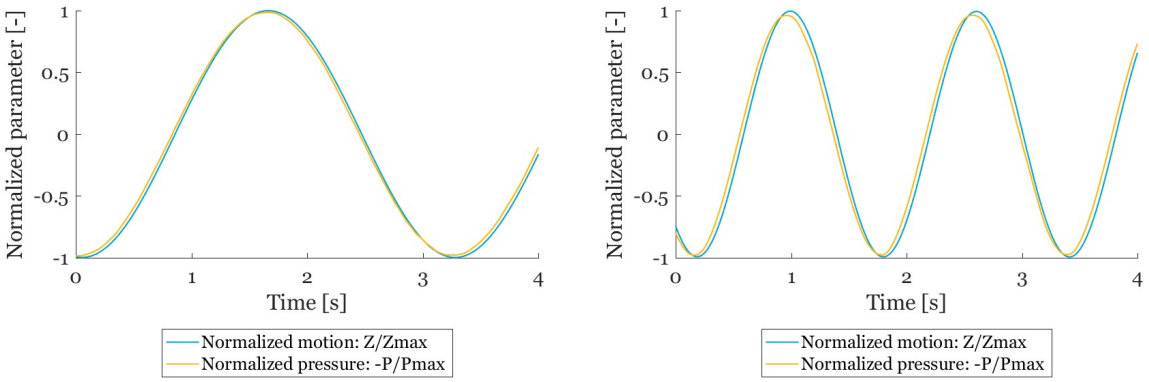

(a) Normalized pressure of sensor 3 and motion of 0.31 Hz vertical oscillation

(b) Normalized pressure of sensor 3 and motion of 0.62 Hz vertical oscillation

Figure 4.10: Phase delay of pressure sensor 3

tops and troughs. The difference between the peaks of the two runs is on average 0.4 N. This accounts for approximately 10 percent of the total signal's height. This rather large deviation has a small influence on the inertia coefficient. The deviation between the both coefficients is only 0.004 [-]. The influence on drag coefficient is larger, 3.1 for run 736 and 3.3 for run 898.
The time traces of the repeat runs of the 100 mm 0.31 Hz oscillations contain more noise than run 736 and 898, as the loads are in the lower range of the load cells. The largest difference between two peaks is 0.3 N. The repeat runs show the same load coefficient trends as observed for run 736 and 898. The load coefficients belonging to the measured forces of the repeat runs are shown in figure 4.8b. Only marginal deviations in the inertia coefficient are found, but the deviations of the drag coefficient are significant. Their magnitude varies between 2.7 and 3.4.

4.4.3. Influence of the inertia corrections in roll

Section 4.2.2 showed a large uncertainty of the magnitude of the mass inertia in roll oscillation. For this study, the influence of the uncertainty on the load coefficients is key. Therefore, these are therefore calculated for two cases: the minimum and the maximum obtained mass inertia. The results of these two cases for the CoG-roll at 0.31 Hz of the flat plate are shown in figure 4.9a and figure 4.9b. The figures show that the spread of results is very large. For the inertia coefficient a spread of 1.5 is found and the spread of the drag coefficient varies between 2.5 and 0.5. This is obviously too large to draw conclusions from. Moreover, 4.9b shows the trend that most drag coefficients are negative.

This means that no conclusions regarding the global load coefficients and the force history of the of the load cells can be drawn. It can thus not be concluded, whether the Morison model is applicable when the undisturbed flow pattern shows a varying velocity over the height of the model. With that, it is not possible to establish an engineering model that accounts for a non-uniformly undisturbed flow pattern. Analysis of the roll oscillations with current is not executed, as this gives the same inaccuracies.

4.4.4. Accuracy of the 10 kg load cells

The moments are measured by the three 10 kg load cells. For determining the loads on the rudder locking system, the moment around the z-axis is of highest interest. This moment is measured by three 10 kg load cells. The individual load cells therefore measure a small force. Due to this, the signals of the 10 kg load cells contain a lot of noise and their signals have a too poor quality to take into account for analysis. The same counts for the moments around the other axis.

4.4.5. Accuracy of pressure signals

On one side of the flat plate model, 5 pressure sensors are fitted. In an initial state of the test series, the model suffered from a leakage. Sensor 1 and 2 had their electronic wires connected inside the model. To check if

the sensors were working properly after the leakage, additional accuracy checks are executed by means of a vertical sinusoidal oscillation. The signals of sensor 1 to 5 for a 0.31 Hz vertical oscillation with an amplitude of 75 mm are shown in figure C.7 in appendix C. The graphs clearly show that sensor 1 and 2 do not give the expected sinusoidal signal, which sensor 3, 4 and 5 do give. Sensor 5 has slightly more noise than sensor 3 and 4. The noise has a bandwidth of approximately 60 Pa for sensor 3 and 4, and 100 Pa for sensor 5.

The sensors are connected to a room with air, which is connected by a 4.0 mm hole to the surrounding water. Therefore, capillary effects may occur. One of these effects can be a delay in the pressure signal. The vertical oscillation is believed to cause an hydrostatic pressure difference only. Little water is disturbed, through which the assumption is made that additional pressures due to flow separation and vortex generation can be neglected. In figure 4.10a and 4.10b the normalized pressure signals and motion signals are shown. The figures show that the phase delay of the 0.31 Hz oscillation is very minor, but clearly shows the delay for the 0.62 Hz oscillation. A second reason for the phase delay between the signal and the motion measured by the motion camera might be the difference in the sampling rate. The pressure signals are sampled at 1000 Hz and the camera's signal at 100 Hz.

5

Analysis of sway oscillation

This chapter discusses the experimental results of the sway oscillations without currents. Hereby the focus is laid on four research objectives:

- To quantify and explain the loads on the rudder in regular sway oscillation.
- To analyse the influence of the oscillation frequency on the loads on the oscillating rudder model.
- To analyse the influence of surface effects on the loads on the oscillating rudder model.
- To propose a load prediction model for a rudder in regular sway oscillation including the required load coefficients.

The chapter starts with analysing the force histories measured in sway direction and validating the Morison equation on these measured loads. Subsequently, the pressures measured on the flat plate model are used to clarify the perceived loads. In section 5.3, the load coefficients of the Morison equation are compared with coefficients of other experimental studies. This is an important validation of the executed experiments. Variations in draught and frequency as well as the differences between the models are debated in this section as well. Section 5.4 contains a general discussion of the findings of this chapter.

5.1. Force history and Morison fits

In this section the force histories are discussed first. The differences between the histories at various KC numbers are stressed. Secondly, the quality of the Morison fit is assessed, through which the validation of the Morison model as appropriate load prediction model is studied.

5.1.1. Force histories

Figure 5.1 shows the force histories of two runs in blue. In figure D.1 and figure D.1 in appendix D, the force histories of the lift profile in 0.62 Hz oscillation are presented for the entire range of tested KC numbers. The two time traces at the lowest KC numbers are governed by noise and therefore lack reliability. The most striking observations of figure D.1 and figure D.1 are summarized below:

- None of the signals is clearly sinusoidal.
- Most signals show a peak load in between the moment of maximum acceleration and maximum velocity; in the figures shown at T = 60.3 s, 61.1 s, 61.9 s, ...
- For KC < 4.0, a local dip is observed at the moment of maximum velocity.
- For KC ≥ 6.0, a small shoulder is observed at the moment of maximum velocity. The larger KC, the more definite the shoulder.

These observations give room to explain the nature of the Keulegan-Carpenter number; a quantity explaining the relative importance of the drag forces over the inertia forces in oscillatory flow. For KC < 8, the loads are

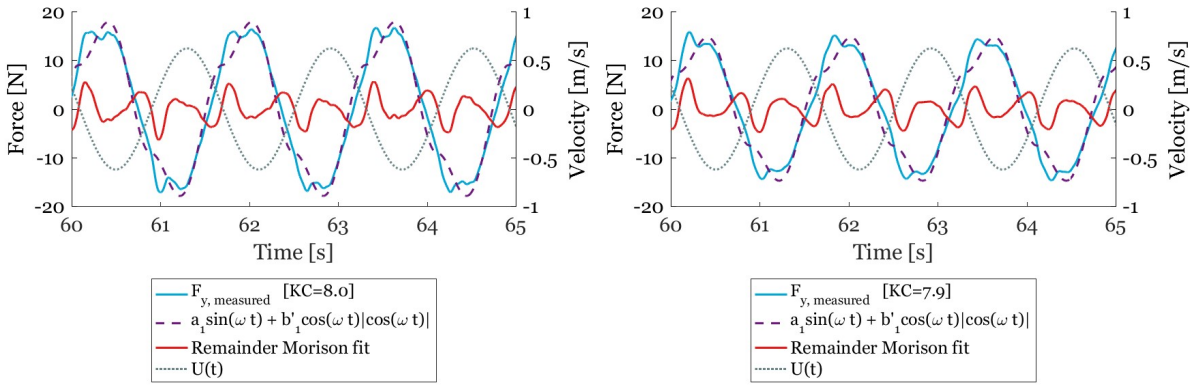

(a) Force history and the Morison fit of the flat plate model in 160 mm sway oscillation at 0.62 Hz

(b) Force history and the Morison fit of the lift profile in 160 mm sway oscillation at 0.62 Hz

Figure 5.1: Force history of both models in 0.62 Hz sway oscillations its Morison- and Fourier fits

classified as 'inertia-dominated', whereas KC > 13 accounts for a drag-dominated load. KC numbers in between are often titled as drag-inertia-dominated, a regime in which both have significant importance (Sarpkaya and O'Keefe, 1996).
The presence of a dip at the moment of maximum velocity at KC < 4 stresses the small impact of the viscous drag forces. The enlarging hump at the moment of maximum velocity when KC rises, shows an increasing influence of the drag.

Figure 5.1 shows the force history of both models in 0.62 Hz oscillation with an amplitude of 160 mm. The time traces are coarsely the same. The signal of the flat plate model is a little larger in amplitude. Both models have their peak load at the same moment in the cycle. Clearly, the flat plate model has a more distinct shoulder at the moment of the maximum velocity. This relates to a larger drag's influence, provoked by the larger amount of sharp edges of the flat plate model, inciting a more fierce generation of vortices.

5.1.2. Morison- and Fourier fits

Figure 5.2 shows the force histories of the lift profile in a 0.62 Hz oscillation with amplitudes of 60 mm and 200 mm. The force histories are compared with the normal 2-coefficient Fourier fit, the 2-coefficient Morison model and the 6-coefficient Morison model, the latter denoted in equation 2.34. Little differences between the force histories of the lift profile and the flat plate model are observed. Therefore only the fits on the lift profile are included and discussed. Moreover, the fits on the lift profile are more relevant for the main research goal.

The force histories are visualised by the blue line, the load prediction equations by the broken purple line and the remainder function, the difference between the force history and the fit, by the red line. The 2-coefficient Morison equation does not represent the force history well. The peak loads are underestimated, especially for the oscillation at KC = 3.0. Further, the fit has a wider form than the force history just after the up- and downward zero-crossing. The 2-coefficient normal Fourier fit shows limitations in terms of predicting the exact force history too. It underestimates the peak load likewise. However, the remainder function of the 2-coefficient Morison fit is found twice as large as the the 2-coefficient Fourier fit for the oscillation at KC = 10.0.
The 6-coefficient Morison equation describes the loads with much higher precision. The peak load is predicted with a high accuracy as well. A comparison of the 4- and 6-coefficient Morison fit is included in appendix D, figure D.3 en D.4. At KC = 3.0, the difference between the 4- and 6 coefficient fit is very limited. At KC = 10.0, the 6-coefficient fit describes the peak force with a significant higher precision.

The underestimation of the peak loads by the Morison model is widely known for flat plates. Keulegan and Carpenter (1958) concluded that the third and fifth term cannot be disregarded for flat plates. They

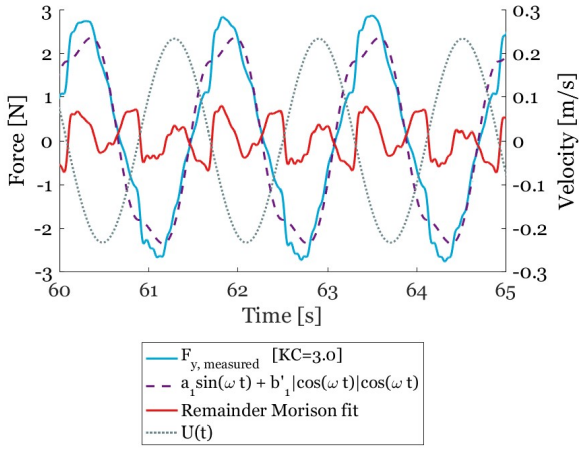

(a) F_y and Morison fit of lift profile in 60 mm sway oscillation at 0.62 Hz

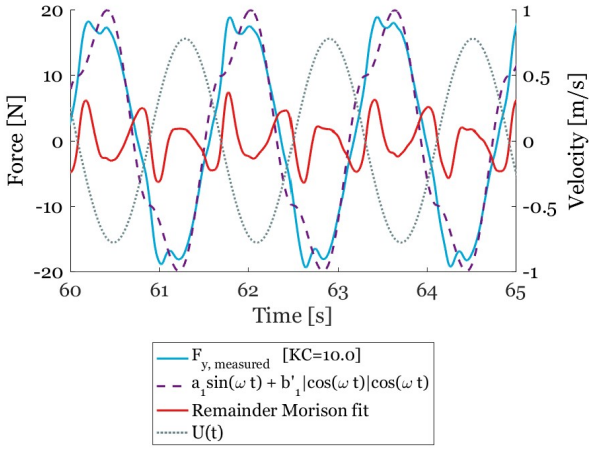

(b) F_y and Morison fit of lift profile in 200 mm sway oscillation at 0.62 Hz

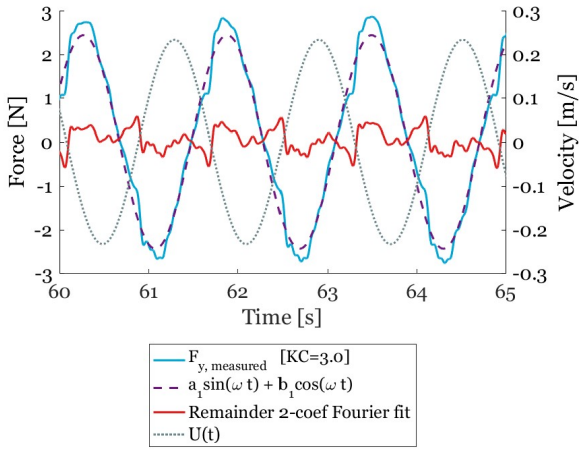

(c) F_y and 2-coefficient Fourier fit of lift profile in 60 mm sway oscillation at 0.62 Hz

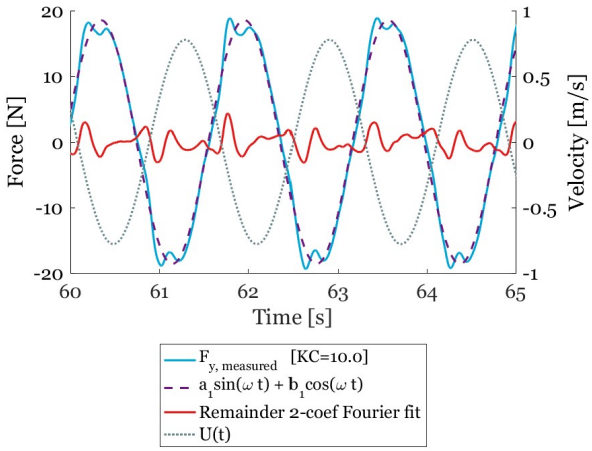

(d) F_y and 2-coefficient Fourier fit of lift profile in 200 mm sway oscillation at 0.62 Hz

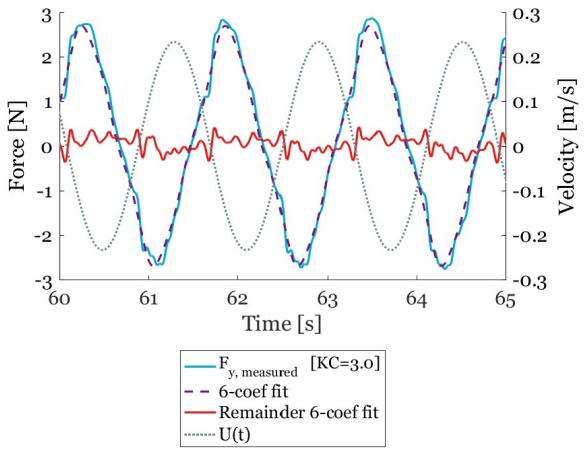

(e) F_y and 6-coefficient Fourier fit of lift profile in 60 mm sway oscillation at 0.62 Hz

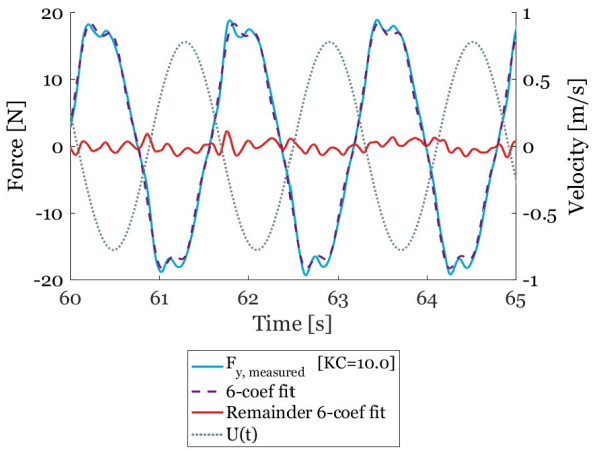

(f) F_y and 6-coefficient Fourier fit of lift profile in 200 mm sway oscillation at 0.62 Hz

Figure 5.2: Force history of the lift profile in 0.62 Hz sway oscillations its Morison- and Fourier fits

recommended to use the 6-coefficient Morison fit. A recent study by Van 't Veer *et al.* (2015) underlines the importance of higher order coefficients for peak loads at bilge keels. For cylinders, the 2-coefficient Morison model describes the time history with much higher precision than observed for flat plates (Sarpkaya and Isaacson, 1981). This is justified with the edge rounding of the body. The results of this section accentuate the similarities between the infinite length flat plates and the model with aspect ratio 1.5. Moreover, the lift profile shows similar characteristics in terms of the Morison's fit as flat plates and bilge keels.

5.2. Analysis of pressures

This section first discusses the pressures measured at a constant root submergence D_r of 200 mm. In the second subsection, the pressures measured at different draughts are compared.

5.2.1. Regular sway at constant draught

The time traces of the three working pressure sensors in sway oscillation at 0.31 Hz with a root-submergence of 200 mm are shown in figure 5.3 to figure 5.5. Sensor P3 is the fitted in the middle of the model, P4 is fitted close to the edge on the right side of sensor P3 and P5 is fitted above sensor P3, near the root. The sensors are placed on one side of the model, so one sensor observes subsequently the pressure-side and the wake-side within one cycle. A positive oscillation's velocity loads the sensors on the pressure-side of the model and a negative velocity loads them on the wake-side.

Analysis of peaks The highest positive pressure is mostly observed at the moment of maximum, positive acceleration. After this peak, the pressure declines gradually, although a shoulder is observed at the moment of maximum velocity. The pressures at the moment of maximum velocity are quite constant and equal 10, 20 and 50 Pa for P3 in the presented figures. The corresponding pressure coefficients $C^+_{p,d}$, obtained with equation 2.40, are 1.5, 1.1 and 1.0. Ikeda *et al.* (1979) found a value of 1.2 for bilge keels. The obtained coefficients in this study show reasonable coincidence. Ikeda *et al.* (1979) presumed that the variations in the load coefficients for varying KC numbers are governed by vortex separation and therefore by pressure variations in the wake. With this reasoning, a constant inertia coefficient $C^+_{p,I}$ at the pressure side is expected too. The height of the pressures at the moment of maximum acceleration over several cycles is considerably constant and show pressures of 20, 50 and 75 Pa for P3. These correspond to the coefficients 0.9, 1.3 and 1.3, which are relatively constant too.

The height of the negative peaks is highly variable, especially at P4. This sensor shows a rapid increase of the troughs. The large, sharp, in height varying troughs indicate a disorganised wake. Their location at P3 and P4 is often at the moment of maximum, negative, velocity. The largest eddies are shed at the moment of the highest velocity. The amplitudes of the wake peaks are a reasonable result of eddy-shedding event. The circulation velocity of an eddy is by a rule of thumb twice the undisturbed velocity. An undisturbed velocity of 0.3 m/s results by Bernoulli's approximation in $\frac{1}{2}\rho \cdot 0.3^2 = 45$ N and in $\frac{1}{2}\rho \cdot 0.6^2 = 180$ N when an eddy is shed. The large negative peaks of the wake-side signals can thus be a reliable consequence of eddy-shedding. The location of the peak is thus as expected. The larger the KC number, the deeper the troughs. At KC = 3.0, the positive tops are almost twice as large as the troughs, whereas at KC = 8.0 the troughs are twice as large as the tops. The appointed inertia- versus drag-regimes are thus conspicuous in the pressure time traces as well.

Differences between the sensors' signals The differences between the sensors are pronounced. P3 and P4 show resonable similarities, but P5's time trace is peculiar. Firstly, the tops of sensor P5 are much larger than the other two sensors and the troughs have a substantially lower magnitude. Secondly, the location of the negative peaks differs. This sensor is close to the rudder stock, around which eddies are visibly shed. This causes additional pressure gradients in general. The vicinity of the rudder stock may also increase the form-drag, as it may obstruct the flow pattern over the edges. The moderate troughs reveal that no large eddies are shed in the vicinity of the sensor. The troughs of P5 are often at the moment of maximum, negative acceleration instead of at the moment of maximum, negative velocity. It seems that the pressure at P5 is more inertia- than drag-dominated. The pressures at P5 may not be a representable pressure in terms of a pressure on a oscillating flat plate due to the rudder stock's neighbourhood.

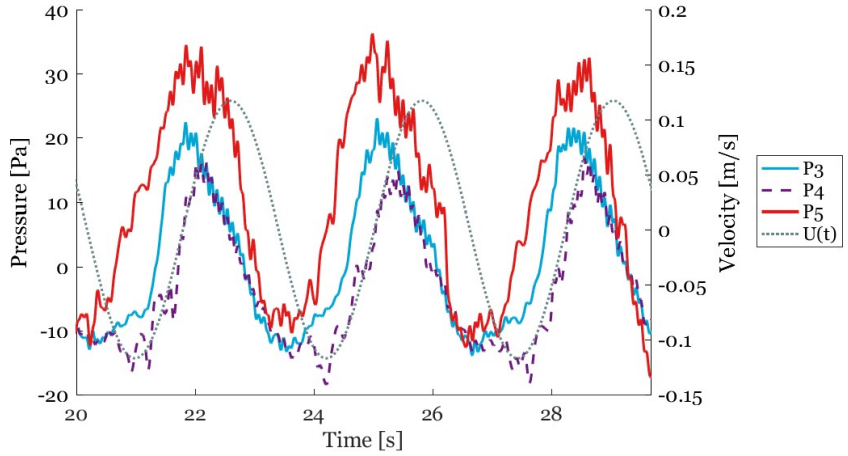

Figure 5.3: Pressure measurements 60 mm sway oscillation at 0.31 Hz

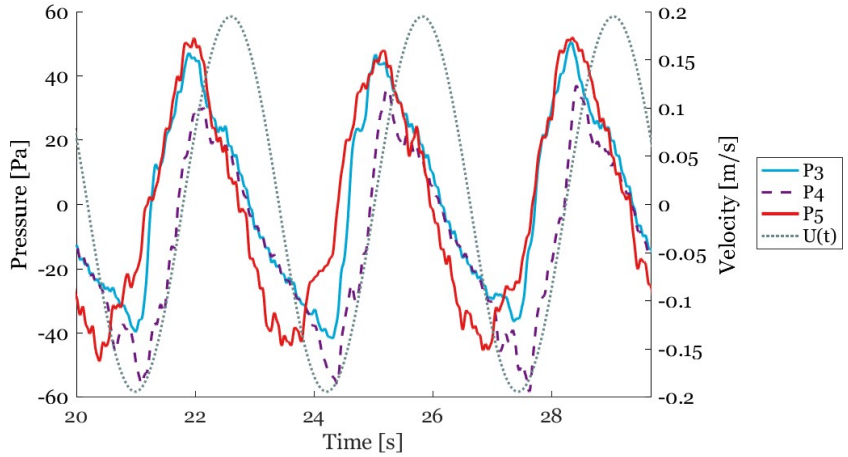

Figure 5.4: Pressure measurements 100 mm sway oscillation at 0.31 Hz

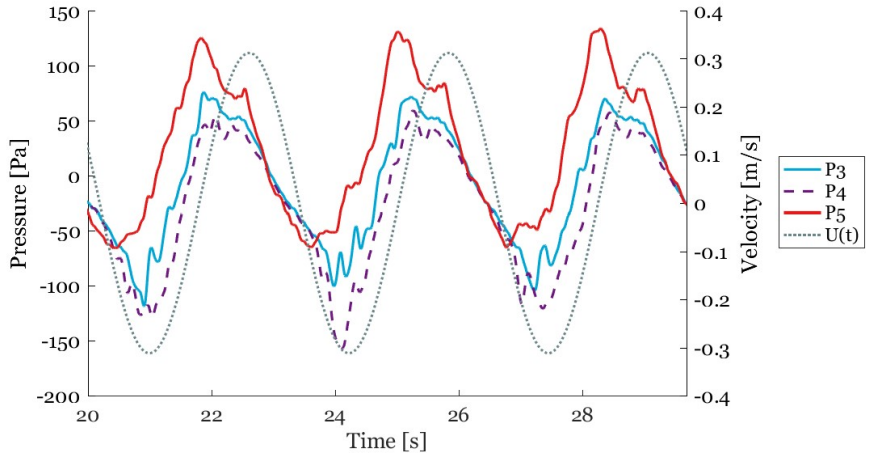

Figure 5.5: Pressure measurements 160 mm sway oscillation at 0.31 Hz

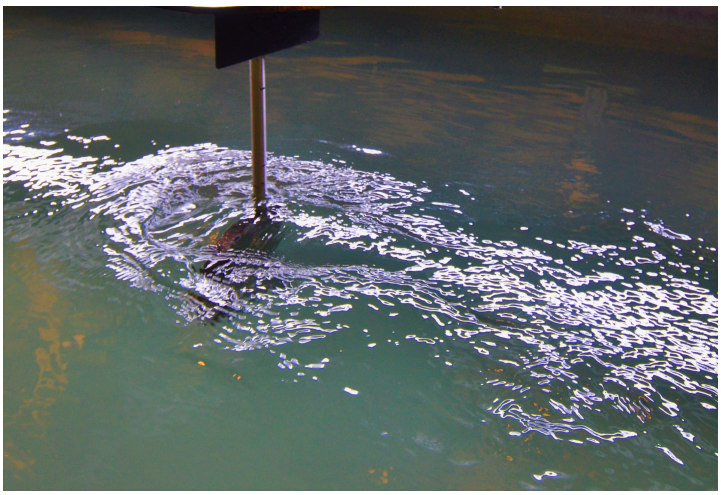

Figure 5.6: Surface effects of 160 mm sway at 50 mm root submergence

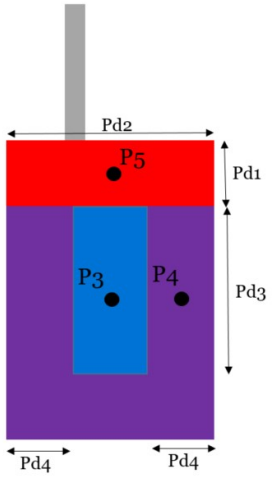

Figure 5.7: Representative areas of pressure sensors

The courses of P3 and P4 show comparison. P4 is close to the edge, through which the the, possibly irregular, shedding of eddies has a large influence on the pressure measured by this sensor. The rapid increase of the wake peak confirms this assumption, as a shedding eddy decreases the pressure sharply. P3 is experiences these pressure differences as well, but as this sensor is placed in the middle of the profile, pressure differences are a result of a much broader spectrum of sources. Peaks are therefore expected to be more moderate.

Ambient pressure During the loading on the pressure-side, that is when the oscillation's velocity is positive, the pressure decreases gradually to a negative value. Before the sensors are loaded as 'wake-side' sensors, the pressure has already become negative. This accounts for all sensors, through which it is believed that a lower ambient pressure is present during the oscillations than in still water. This can be caused by a dynamic pressure or turbidity in the ambient flow, which is not present in still water. Another theory for the pressure drop is that the model may decelerate more rapidly than the entrained fluid decelerates, through which vortices are bend around the model before the velocity has become zero. The presence of the near eddies can cause the pressure drop.

The pressures are positive before de sensors are loaded as 'pressure-side' sensors. However, the smaller the amplitude, the closer P4 follows the velocity profile in between the trough and the top. This shows a less disorganised wake. The pressure increase of P3 is ahead of P4, which can be caused by a larger form-drag at P3.

Amplitude variations The exact location of the tops and trough shifts per amplitude. The tops at higher KC numbers are more in-phase with the velocity. At lower KC numbers the tops tend more towards the moment of maximum acceleration. Literature states that at KC numbers smaller than 8, the forces are inertia dominated. At KC numbers larger than 13, they are drag dominated (Sarpkaya and O'Keefe, 1996). When the tops are more in phase with the velocity instead of the acceleration, the load becomes more drag dominated. This conclusion is drawn with the force-signals as well.

Frequency variations Two pressure sensor time traces at 0.62 Hz are included in appendix E, figure D.5 and figure D.6. The courses of these graphs show many similarities with the courses of the same KC number at 0.31 Hz. Only small differences are observed, but these can be due to the sensors' resolutions. The similarities between the frequencies indicate that the loads are not depending on the Reynolds number. The assumption that the loads are governed by separation and eddy-shedding is thus likely to be valid.

5.2.2. Influence of draught on pressures

Sway oscillations are executed on 50 mm, 100 mm and 200 mm root submergence. A comparison between the tests is done by means of inspecting the pressure sensors' time traces. In appendix E pressure sensors'

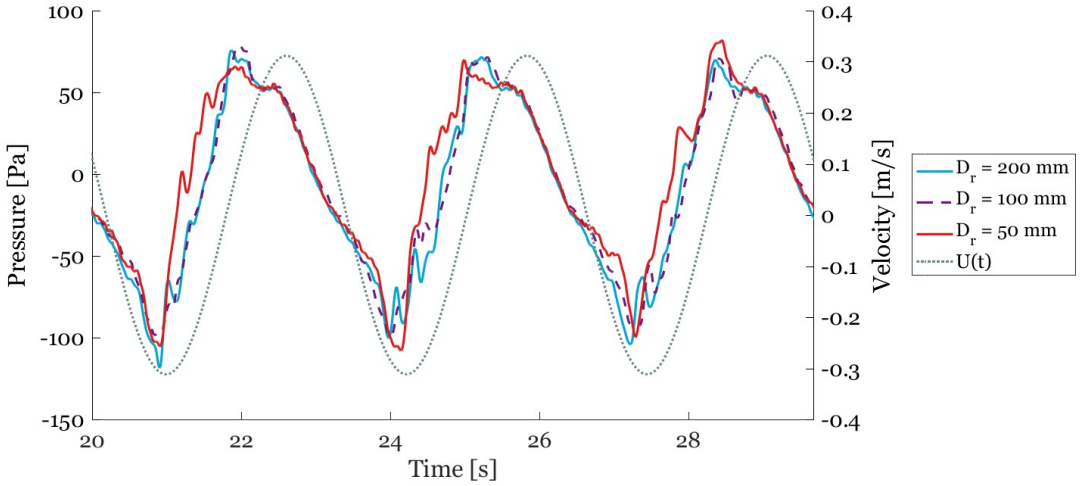

(a) 10 seconds of P3 pressure signal at different draughts for a 160 mm 0.31 Hz sway oscillation

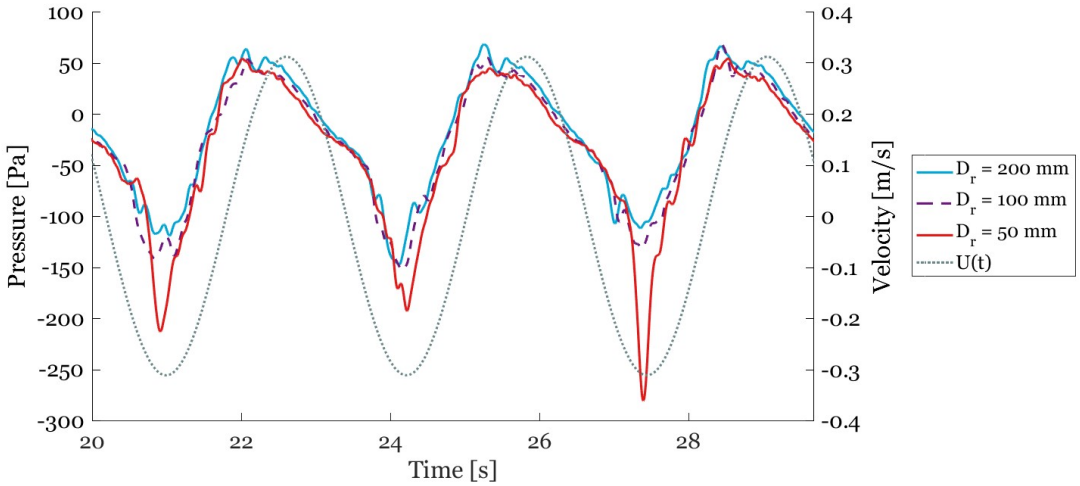

(b) 10 seconds of P4 pressure signal at different draughts for a 160 mm 0.31 Hz sway oscillation

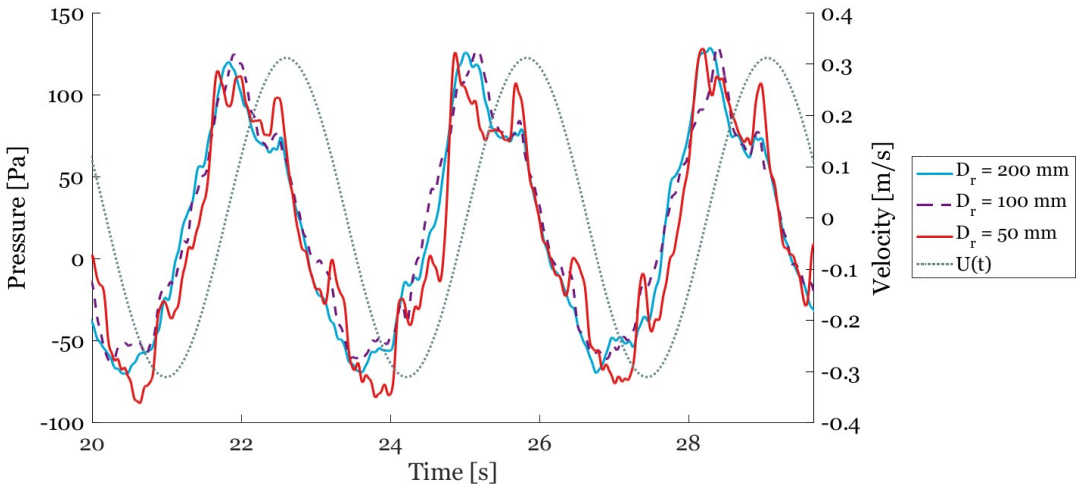

(c) 10 seconds of P5 pressure signal at different draughts for a 160 mm 0.31 Hz sway oscillation

Figure 5.8: Pressure sensor time traces in 160 mm 0.31 Hz oscillations at various draughts

time traces of 20 seconds are shown. The model is tested at 0.31 Hz with amplitudes of 60 mm, 100 mm and 160 mm. A 10 seconds time trace of the 160 mm amplitude is shown in figure 5.8. Bluntly said, the signals at the lowest submergence are the most irregular and contain significantly more peaks than the signals at deeper submergences. The conspicuities of P4 and P5 are elaborated extensively underneath.

P4's signals The most explicit observation of P4's signal are its large excursions at the wake-side at the smallest submergence. The magnitude of the troughs of P4 varies a lot. As the wake of P4 is governed by separating eddies, the irregularity of the signal indicates an unstable pattern of vortices: their size- and strength may vary every cycle. At the lowest draught, the wake peaks of P4 are sometimes much larger, indicating a significant influence of the free surface. The signals and moreover visual observations showed an apparent generated of vortices when the free surface was close. The lower hydrostatic pressure may play a role in this. Some air-suctions were observed during the experiment too.

P5's signals Sensor P5 shows many differences between the smallest and the deeper submergences. Visual observations showed large free surface disturbances at the lowest draught too. An indication of this is shown in figure 5.6. A significant wave was generated and flowed over the model when the model's velocity was at its maximum. At deeper draughts, only a disturbance of the surface was observed by the rudder stock's surface piercing.
P5 shows a positive peak at the moment of maximum deceleration at the smallest submergence. Furthermore, at the moment of maximum velocity, sharp peaks are observed at the smallest submergence. Less distinct peaks at this moment are observed at larger submergences. Positive pressure peaks are observed at the moment of the negative velocity's maximum. These peaks are also to a lesser extend observed for P3. The peaks at the moment of maximum velocity can partly be due to an hydrostatic pressure increase due to the generated wave. The wave had an height of 1 cm at most, which relates to a hydrostatic pressure increase of 100 Pa. This is much more than the actual peak height's rise. Moreover, the hydrostatic pressure should be felt by at least sensor P3 as well, as this sensor is right underneath P5. P3's signal only shows a small increase. The increased pressure can thus not be attributed to a hydrostatic pressure increase only. Therefore, the free surface disturbance increases the dynamic pressure which causes a pressure drop; this flattens the increased hydrostatic pressure.

5.3. Load coefficients

Subsection 5.1.2 stated that the Morison model predicts the loads appropriately if its 6-coefficient form is used. The model uses empirical load coefficients, which are discussed in this section. First, the first-order terms, the drag- and inertia coefficient, are discussed and validated with reference studies. Secondly, the higher order coefficients are presented.

5.3.1. Inertia coefficients

The cycle-averaged inertia coefficients are shown in figure 5.9a. In here the inertia coefficients found by Keulegan and Carpenter (1958) for infinite length flat plates are included as well. The figure clearly shows that the inertia coefficients of the rudder model with aspect ratio 1.5 are lower than the coefficients of the infinite length flat plate. As already stated by Ridjanovic (1962), a limited aspect ratio causes separation around all four edges. Likewise, less fluid is entrained by the model, causing a lower inertia coefficient.

The inertia coefficients of Keulegan and Carpenter (1958) show a distinct dip between $8 < KC < 20$. This dip is absent for the coefficients of the rudder models. Figure 5.11 shows possible vortex shedding patterns for a bilge keel, an infinite length flat plate and a flat plate with aspect ratio 1.5. Around the bilge keel, the shed vortex has by approximation always the same size and strength (Sarpkaya and O'Keefe, 1996). The inertia coefficients of the bilge keel increase gradually and do not show a drop (figure 2.10). In the drag-inertia dominated regime ($8 < KC < 13$), the vortices generated around the edges of the infinite length flat plate are asymmetric; one time the larger vortex is shed around the upper edge, the other time around the lower edge. This 'unstable' situation is believed to cause the drop of the inertia coefficients (Sarpkaya and O'Keefe, 1996) (Li, 1989). For the finite length flat plate, this instability takes place as well and large vortices are shed from different edges. The time trace of P4 at $KC = 8.0$, figure 5.5, shows a significantly varying wake peaks per cycle. However, the dip in the inertia coefficient is absent. This bears the theory that the vicinity of the root and tip has a smoothing function: vortices are nonetheless shed around all edges, creating a quasi-steady flow

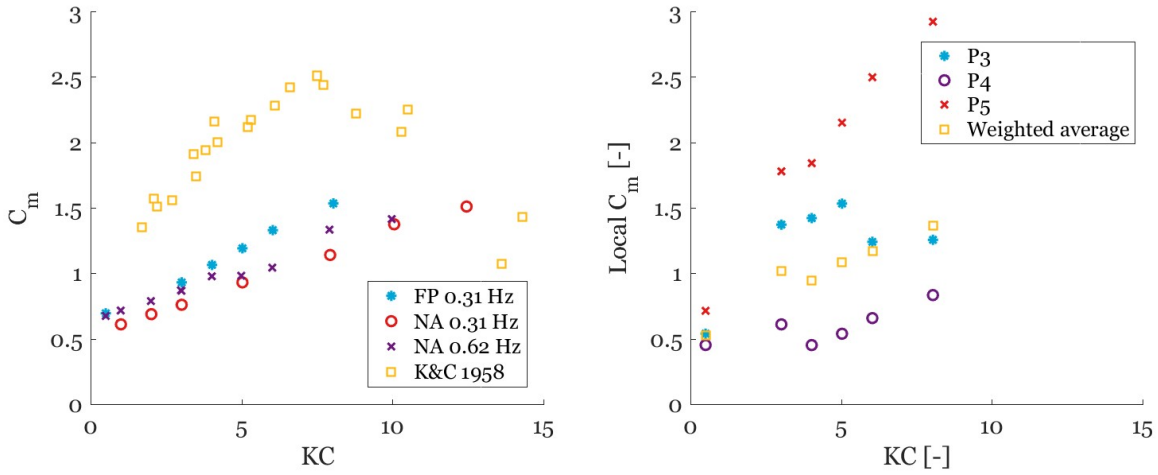

(a) Cycle-averaged inertia coefficients at 0.31 Hz sway oscillations

(b) Instantaneous inertia coefficients derived from pressure measurements at 0.31 Hz sway oscillations

Figure 5.9: Inertia coefficients at 0.31 Hz sway oscillations

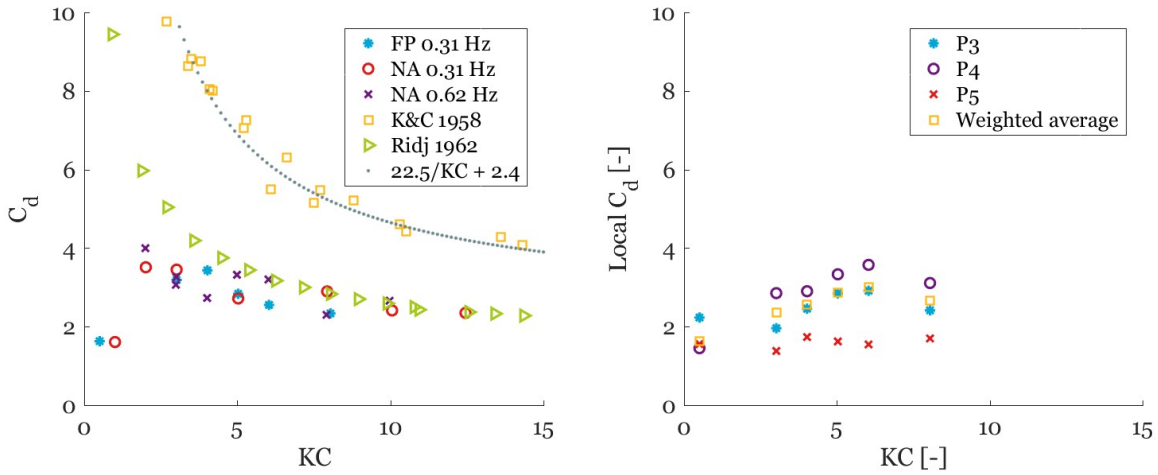

(a) Cycle-averaged drag coefficients of 0.31 Hz sway oscillations

(b) Instantaneous drag coefficients derived from pressure measurements at 0.31 Hz sway oscillations

Figure 5.10: Drag coefficients at 0.31 Hz sway oscillations

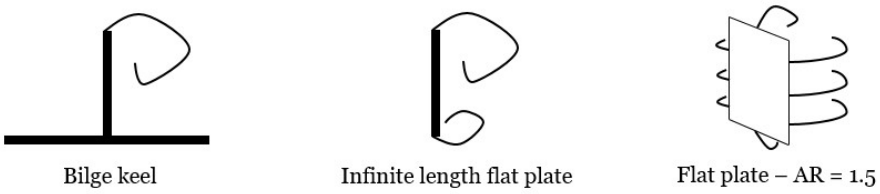

Figure 5.11: Examples of vortex shedding patterns in the drag-inertia dominated regime.

through which a large eddy cannot cause the inertia coefficient to drop.

The inertia coefficients of the 0.62 Hz oscillation are slightly larger than the coefficients at 0.31 Hz. The differences are marginal and it cannot be determined whether or not the difference is a measurement inaccuracy or indicates a Reynolds number dependency.

Instantaneous inertia coefficient An analysis in terms of load coefficients is also executed with use of the pressure sensors. The main purpose hereof is validation of the results and the search to conformity between the measured forces and pressure. The 'instantaneous' load coefficients are determined with the method proposed by Ikeda *et al.* (1979), presented in section 2.4.6. Per sensor, an instantaneous load coefficient is obtained and with the three of them, a representative coefficient is obtained via a weighted average. This weighted average is visualised in figure 5.7. The dimensions denoted by 'Pd' determine the coverage area of a single pressure sensor. Sensor P4 and P5 are located 20 mm from the edge. Therefore a bandwidth of 40 mm is used: Pd1 and Pd4 are both 40 mm. As stated in the previous section, the signal of P5 is likely to be largely influenced by the rudder stock and eventually surface effects may play a role. Therefore P5 only covers the root's edge and P4 covers all other edges. The remaining area in the center is covered by P3.

The coefficients show consistent trends per sensor, although their magnitude differs. P5 distinctively has the largest inertia coefficients, succeeded by P3 and P4. This is consistent with the findings of the previous section, in which P5 had the highest tops, followed by P3 and subsequently P4. The small instantaneous inertia coefficient of P4 relates thus to large shed eddies. At P5 only small vortices are detected, resulting in a large instantaneous inertia coefficient.
The weighted average of the instantaneous inertia coefficient is on average a little lower than the cycle-averaged inertia coefficient found with the load cells. Nevertheless, they show an appropriate agreement. Too little pressure signals were available to draw conclusions on the pressure distribution over the blade.

5.3.2. Drag coefficients

Figure 5.10a shows the drag coefficients elaborated with the force measurements. The coefficients Ridjanovic's flat plate with AR = 1.5, Keulegan and Carpenter's infinite length flat plate and the bilge keel of Ikeda *et al.* (1979) are included as well. For KC > 2.0, the coefficients resemble the coefficients of Ridjanovic, especially for KC > 8.0. A certain relation with the aspect ratio of the model is thus exposed.

For 2 < KC < 8 the measured drag coefficients are a little lower than those of Ridjanovic (1962). According to Tanaka *et al.* (1982), plates with a thickness over height ratio of 0.2 have little lower drag coefficients compared to the ones with smaller thickness over height ratios. This justifies the drag coefficient's trend. The scatter between the results of the experiments indicate a inaccuracy's bandwidth, through which differences between the models cannot be distinguished. The same counts for the frequency's variation.
For KC ≤ 2, measurement inaccuracies are striking; the measured forces contained much noise. Moreover, at small KC numbers, the sensitivity of the inertia correction is tremendous. A inertia's phase's miscalculation of a few hundredths of a second could modify the drag coefficient's magnitude drastically. The trend of the coefficients for KC numbers smaller than 2 cannot be distinguished.

Instantaneous drag coefficients The instantaneous drag coefficients show similar trends as the trends of the cycle-averaged coefficients. The instantaneous drag coefficients of sensor P4 are the largest, followed by P3 an P5. This order is the exact opposite of the order of the instantaneous inertia coefficients. The large mag-

nitude of P4 is caused by the large eddies shed around P4's edge; their wake suctions are mainly aligned with the undisturbed velocity. Moreover, P5 only showed small wake suctions, leading to a small drag coefficient. P3 again shows a moderate behaviour. P3's signal is less directly influenced by the vortices generated around the edges, through which the pressure drop is less distinct. A smaller instantaneous drag coefficient is thus a reasonable result. The averaged coefficient have the same order of magnitude as the cycle-averaged coefficients. Ridjanovic's trend upward-going trend for small KC is not recognized for the averaged coefficient.

5.3.3. Higher-order coefficients

Morison equation's higher order coefficients A_3, B_3', A_5 and B_5' are shown in figure 5.12 and 5.13. The coefficients of the infinite length flat plates of Keulegan and Carpenter (1958) are included as well. The dimensionless coefficients A_3 and B_3 are enlarging when the KC number decreases. When the KC number increases, A_3 tends towards zero for all models except the flat plate in 0.31 Hz oscillation. Here A_3 is slightly negative. A_5 also tends to zero for all cases. The higher order sine terms thus have a minimal influence, especially when $5 <$ KC < 12.6. The lower values of A_3 of the flat plate hint towards a different behaviour of the flat plate compared to the lift profile; slight differences in the remainder functions of figure 5.1 were noticed too.
The coefficients A_5 and B_5' are distinctively smaller than the third order coefficients. They yield negative values. B_5' shows a nearly constant trend, except for KC = 0.5 and KC = 1.0. However, this is possibly caused by measurement inaccuracies. The coefficient A_5 shows a light decrease for declining KC numbers and a spread is found between the results. The coefficients related to the cosine term, B_3' and B_5', are larger than the sine-related coefficients A_3 and A_5. Generally, the trends of the higher order coefficients are clear. This makes the the applicability of a 6-coefficient Morison equation feasible for engineering practice.

5.4. Discussion

The main objective of this chapter is to compose a prediction model for the rudder loads in regular sway oscillation. Hence the loads on the rudder models are quantified and explained, whereby the effects of the oscillation's frequency and the surface effects are evaluated too. The 6-coefficient Morison equation shows an adequate agreement with the measured loads. Lower order fits underestimate the peak loads and show discrepancies with the force history. The normal Morison model is thus found too simplistic to capture the complex, by separation governed loads on the rudder.

The first order load coefficients, the inertia- and drag coefficient, are compared with references studies. A clear KC number dependency is obtained. The inertia coefficients are by approximation half the magnitude of the inertia coefficients of the infinite length flat plate of Keulegan and Carpenter (1958). The obtained coefficients do not show a dip at $8 <$ KC < 13, as observed for infinite length flat plates. These infinite length plates show vortex shedding instabilities in this regime, through which an inertia coefficient dip is generated. The four-edge separation is believed to reduce the asymmetry, which dissolves the dip in the inertia coefficient.
The drag coefficients showed a reasonable resemblance with the flat plates with aspect ratio 1.5 of Ridjanovic (1962) and are significantly smaller than those of infinite length flat plates. The separation around all four edges is causing additional energy dissipation in the wake, which lowers the drag coefficients. The coefficients are slightly lower than the coefficients of Ridjanovic and that is, accordance to Tanaka *et al.* (1982), a likely event due to the increased plate thickness. The aspect ratio's influence thus holds a mayor influence on both the inertia and drag coefficient.
The higher order coefficients show clearly distinguishable trends. This makes the the applicability of a 6-coefficient Morison equation feasible for engineering practice.

The vicinity of the free surface alters the pressures significantly. The wakes increased in irregularity and showed larger pressure dips. The free surface's influence on the forces measured fell in the uncertainty bandwidth. For KC ≤ 2 the results become very unreliable. Further, the drag coefficients were not accurate enough to distinguish differences between oscillation frequencies and the models. Experiments with a higher accuracy are required to study the exact load differences between the models and the trends at low KC numbers.

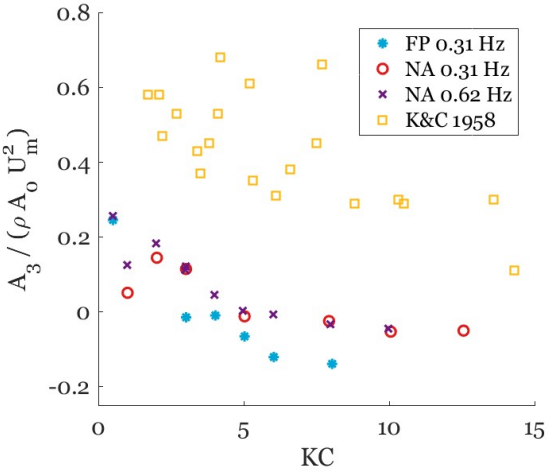

(a) Dimensionless coefficient A_3

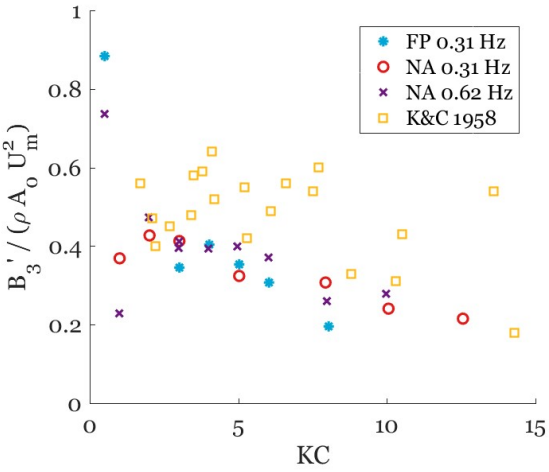

(b) Dimensionless coefficient B_3'

Figure 5.12: Dimensionless coefficients A_3 and B_3'

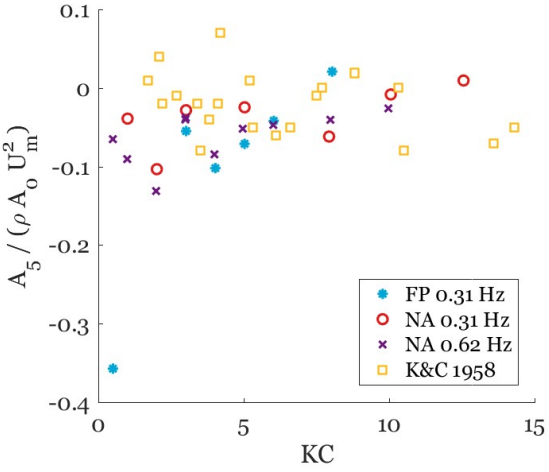

(a) Dimensionless coefficient A_5

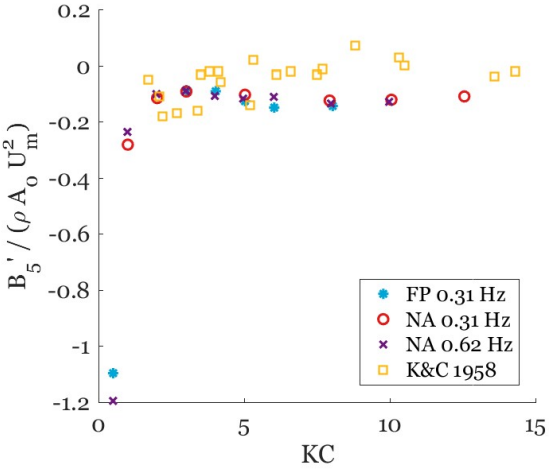

(b) Dimensionless coefficient B_5'

Figure 5.13: Dimensionless coefficients A_5 and B_5'

6

Analysis of sway oscillation in planar current

Currents are practically always present in ocean environments. The previous chapter showed that the wake was greatly related to the forces acting on the rudder. Currents may alter the wake pattern of a body significantly (Sarpkaya and Storm, 1985), therefore this chapter is dedicated to study the current's influence on the loads. This is captured in the following objectives:

- To quantify and explain the loads on the rudder in regular sway oscillation and current, acting perpendicular to the rudder's blade.
- To propose a load prediction model for a rudder in regular sway oscillation and current and include the required load coefficients.

The chapter starts off with an explanation of additional theoretical elements and parameters used for the load analysis in this chapter. Thereafter, the effect of wake biasing is discussed with the pressure sensors' time traces in section 6.2. The current's influence on the loads is discussed in section 6.3, including an analysis of the Morison equation's fit. The trends of the load coefficients are discussed in the section 6.4. The findings of this chapter are reviewed in the last section.

6.1. Additional theoretical elements

6.1.1. Combined velocity profile

Due to the current's presence, the magnitude of the flow velocity experienced by the rudder varies over the oscillation cycle. It is not a regular cosine any more. Figure 6.1 shows the current and oscillation velocities

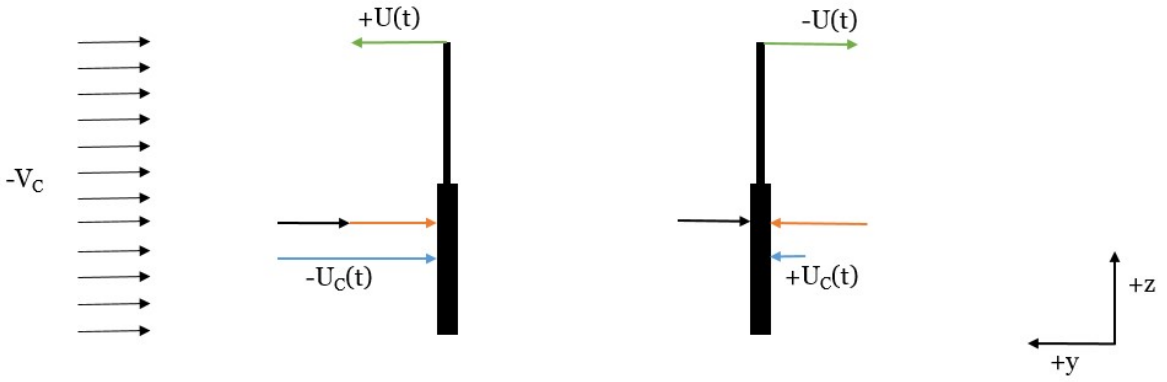

Figure 6.1: Sign conventions of model- and current velocity

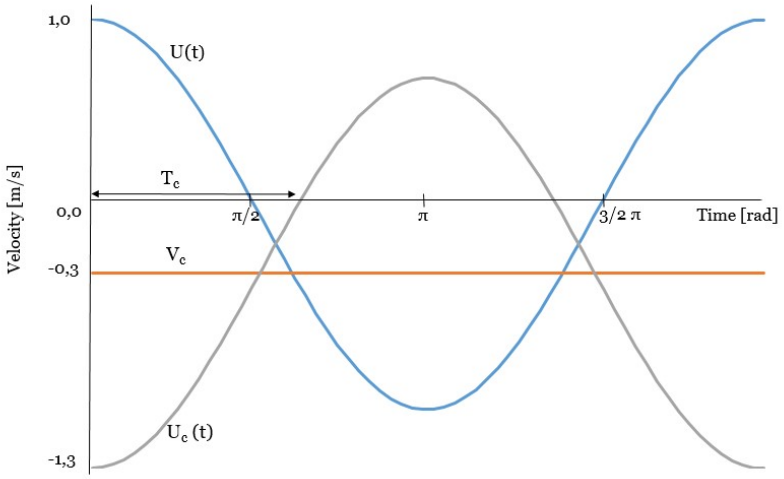

Figure 6.2: Altered velocity profile by a perpendicular current's addition.

with regards to the coordinate system explained in chapter 2. The rudder on left of the figure has a positive velocity $U(t)$ and moves towards the left. Imagine a video camera following the models motion. The camera will record the fluid flowing from left to right, through which the model experiences a fluid velocity with its direction opposite to the model's velocity. In figure 6.1, the model's velocity is shown by the green arrow and the model's fluid velocity 'experience' by the orange arrow.
When current is applied on the model as well, the velocity pattern is altered. For all tests, the current acted perpendicular to the blade and mostly the direction of it was negative, as this is the positive driving direction of the towing tank's carriage. This current velocity is presented by the black arrows in figure 6.1. Superimposing the model's experienced velocity and the current velocity results in a 'combined velocity' vector $U_c(t)$, shown in blue. A positive model's motion and a negative current results in a large negative combined velocity. A negative model's motion and a negative current results in a small positive combined velocity.

Figure 6.2 shows the altered sinusoid $U_c(t)$ by the grey line. The model's velocity is displayed in blue and the current velocity in orange. The combined velocity is the sum of the model's velocity times minus 1 and the current velocity:

$$U_c(t) = -U(t) + V_c \tag{6.1}$$

The combined velocity does not show symmetry over the x-axis. Consequently, the locations of its zero-crossings are altered. The first zero-crossing T_c is derived by:

$$T_c = \cos^{-1}\left(\frac{V_c}{U_m}\right) \tag{6.2}$$

Due to the asymmetry of the flow velocity, the disturbed flow may behave as it should in a higher or lower KC number. When the current flow and the flow caused by the oscillation are aligned, the model is experiences a larger KC number: K^+. The number is defined with $U_m + |V_c|$. The KC number experienced in the opposing stroke is K^-; construed by $U_m - |V_c|$. The K^+ regime has the longest duration; $2 \cdot T_c$.

6.1.2. Wake- and pressure side's pressure signals

The pressure sensors are fitted to one side of the model. Due to the flow velocity's asymmetry, pressure sensors do not measure a complete pressure history over a cycle any more. The sensor is located on either the currents' pressure-side or the currents' wake-side. Two runs are required to obtain the full pressure history, one with a positive current velocity and one with a negative current velocity. A certain duo is shown in figure 6.3 for P3's signal. The signals show distinct differences between oscillations in a negative- respectively positive current.
If a current acts directly on the sensor, such that the sensor is located on the model's front side with respect to the current, the sensor is called a 'Front Side' (FS) sensor. This happens when the current, according to the coordinate system of figure 6.1, is negative. If the current acts to the model and causes the sensor to be in its

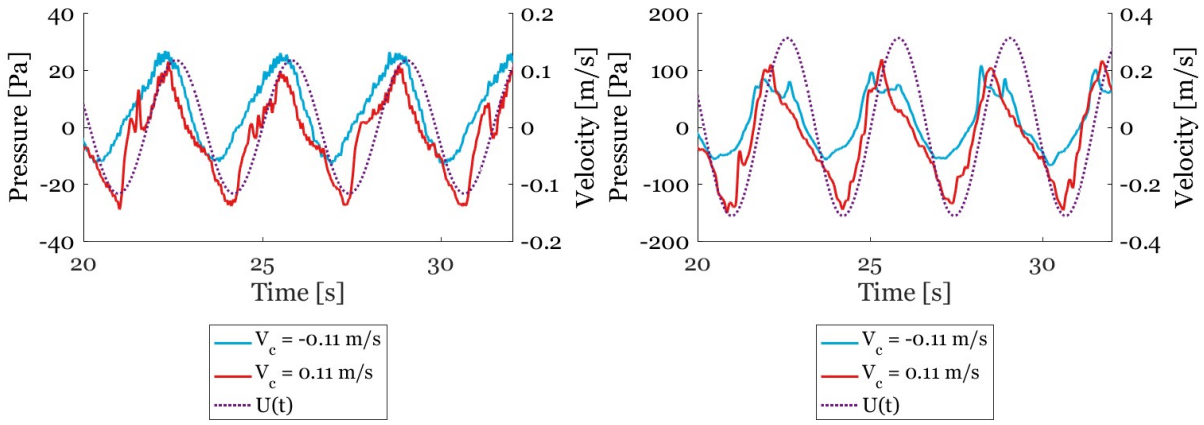

(a) P3 in 60 mm oscillation at 0.31 Hz in positive and negative current of 0.11 m/s

(b) P3 in 160 mm oscillation at 0.31 Hz in positive and negative current of 0.11 m/s

Figure 6.3: P3 in 0.31 Hz sway oscillation in positive and negative current of 0.11 m/s

wake, the sensor is called an 'Aft Side' (AS) sensor. It is hereby not said that an AS-sensor only measures wake. If the current velocity is smaller than the maximum oscillation velocity, the FS-sensor also measures the wake for a period of the cycle. The opposite accounts for the AS-sensor. The names thus only refer to the current's direction.

6.1.3. Additional post-processing of data

The 'relative velocity' Morison model is often used as a prediction model for co-existing (oscillations and current) flow fields. It uses the 'combined velocity' as input for the Morison model's drag term. The inertia term is defined by conventional means. The coefficients of this model are determined with the method of Least Squares, which uses the following format shown in equation 6.3. The coefficient $B_{1,cur}$ is multiplied with $\frac{-2}{\rho \cdot A_0}$ to obtain the drag coefficient.

$$F_{M,cur} = -A_{1,cur}\sin(\omega t) + B_{1,cur}\,(V_c + U(t))\,|V_c + U(t)| \tag{6.3}$$

The velocity of the carriage was not completely steady for all experiments. For oscillations at an high frequency or with large amplitudes, the carriage bore significant vibrations which made the carriage's velocity unsteady. For the most demanding oscillations, velocity variations up to 20 percent were observed. The time-varying speed of the carriage is taken into account.

6.2. Pressure sensors' time traces

This section evaluates the pressure sensors' signals. The first subsection inspects the wake biasing due to the current and the second subsection investigates the current's effect the front-side pressures.

6.2.1. Wake-biasing by current

The P3-AS signals are presented in figure 6.4. The zero-current signals are drawn in these graphs as well. The signals of P4 and P5 are included in appendix F, figure F.1 respectively F.2. Sarpkaya and Storm (1985) reported significant biasing of a cylinder's wake due to currents. This section assesses the rudder model's wake-biasing.

Bluntly, the current's influence depends on its magnitude relative to the magnitude of the oscillations' velocity and its influence can be expressed as the fraction between the current velocity and the maximum oscillation velocity: $\Lambda = \frac{V_c}{U_m}$. This fraction will be referred to as the 'velocity parameter'. For the runs inspected in this subsection, its magnitude is shown in table 6.1. A large velocity parameter accounts for a large influence of the current. A magnitude larger than 1 implies that the current velocity is larger than the maximum oscillation velocity. It is likely that the current has a substantial influence. Contrarily, a small velocity parameter indicates a minor current's influence.

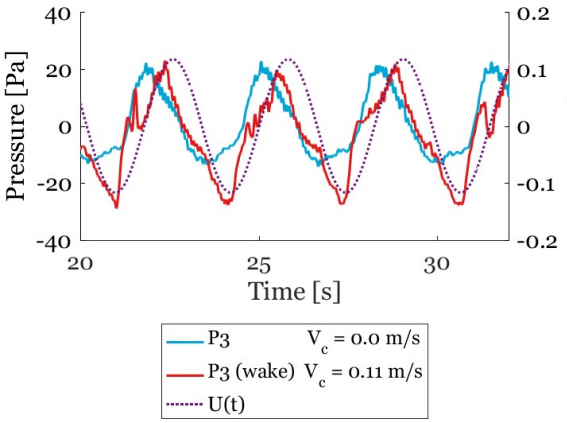

(a) P3-AS in 60 mm oscillation at 0.31 Hz

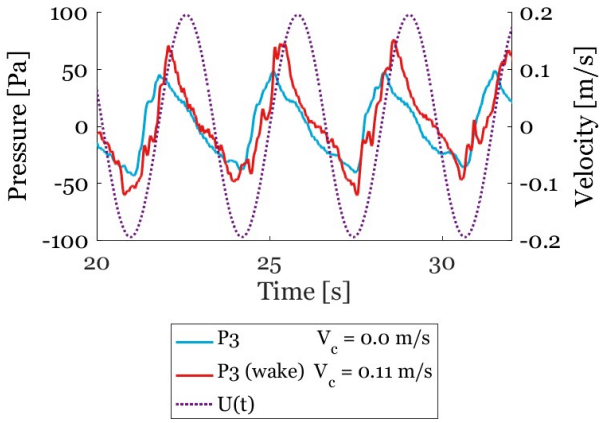

(b) P3-AS in 100 mm oscillation at 0.31 Hz

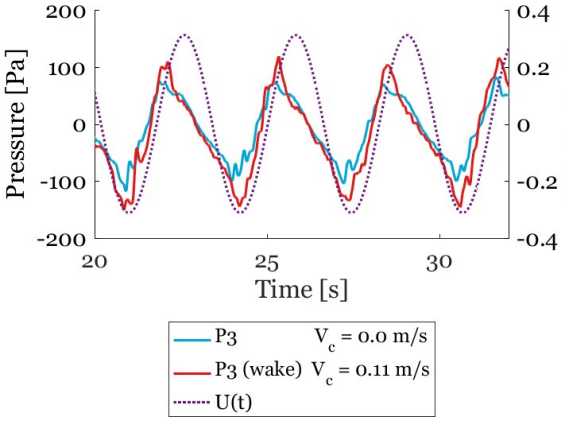

(c) P3-AS in 160 mm oscillation at 0.31 Hz

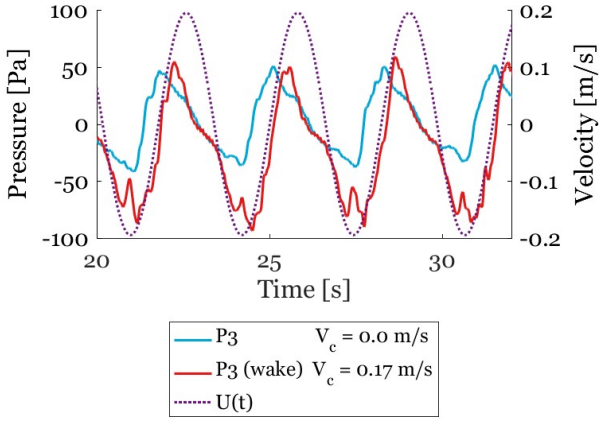

(d) P3-AS in 100 mm oscillation at 0.31 Hz

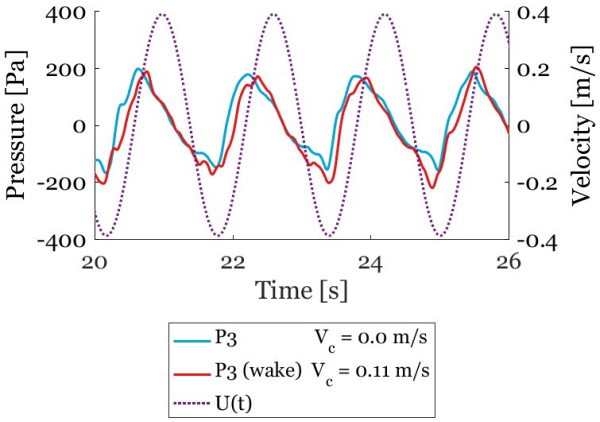

(e) P3-AS in 100 mm oscillation at 0.62 Hz

Figure 6.4: Time trace of P3-AS in current compared with P3 in zero-current

Table 6.1: Velocity parameters for oscillations at 0.31 Hz

	$\frac{V_c}{U_m}$ (0.31 Hz, 0.11 m/s)	$\frac{V_c}{U_m}$ (0.31 Hz, 0.17 m/s)	$\frac{V_c}{U_m}$ (0.62 Hz, 0.11 m/s)
20 mm	2.82	-	-
60 mm	0.94	-	-
100 mm	0.56	0.87	0.28
160 mm	0.35	-	-
250 mm	0.23	-	-

Wake-biasing at P3 and P4 Figure 6.4 compares the zero-current signals of P3 with the wake-side signals in current conditions. Some cases show a large wake-biasing, for instance figure 6.4a and 6.4d. The wake side signals of P4, shown in figure F.1 are even more striking.
The influence of the velocity parameter is clearly visible. The 60 mm 0.31 Hz oscillation in 0.11 m/s current (figure 6.4a) and the the 100 mm 0.31 Hz oscillation in 0.17 m/s current (figure 6.4d), with $\Lambda = 0.94$ respectively 0.87, show the same wake-biasing behaviour. Also the the 160 mm 0.31 Hz oscillation in 0.11 m/s current and the 100 mm 0.62 Hz oscillation in 0.11 m/s current have roughly the same pressure course. Their velocity parameters are 0.35 respectively 0.28. A certain relation with Λ is thus observed for at least these two runs. Moreover, the difference between the zero-current case and the case with Λ = 0.35 en 0.28 is very limited, showing a confined wake-biasing for small velocity parameters.
Further, tops of the AS-signals are larger than the tops of the zero-current's signals for the 100 mm 0.31 Hz oscillation in 0.11 m/s current for P3 and P4. This behaviour is also slightly noticed for the 160 mm 0.31 Hz oscillation in 0.11 m/s current. This may be the effect of a lower dynamic pressure in the ambient flow, as the current may drag the turbulence away from the model. Besides that, a local maximum of P3-AS at the moment of maximum negative velocity for 0.17 m/s current is observed, which is not present for a current velocity of 0.11 m/s. These two cases contain the largest combined velocities, which may have altered the dynamic pressure or influenced the surface effects.

Wake-biasing at P5 In the previous chapter, the observation is made that P5 behaves differently than the other two sensors. In a co-existing flow field, the distinction is magnified. The wake is only slightly larger than in the zero-current condition. None of the cases shows large wake peaks. P5 shows indifferent behaviour due to the current. For some cases, P5 shows higher tops with current than in zero-current. One would expect a lower pressure, as the absolute velocity acting on the sensor is smaller than in the zero-current case. The higher tops are the most striking for the two cases with the highest velocity parameter, which have a KC number of 3.0 and 5.0. A lowering of the ambient dynamic pressure may be the cause, as the current may drag the disturbed water along.

6.2.2. Pressure-side's alteration by current

The signals of the FS-sensors are shown in figure 6.5. In appendix F more signals of the FS-sensor are included figure F.3, figure F.4 and figure F.5.

Cyclic behaviour Most of the FS-signals show a gentler course in a co-existing flow field than in zero-current conditions. For $\Lambda < 1$, the sensor is basically only loaded to its pressure-side, disregarding the large, irregular wake peaks. The lower Λ, the more moderate the signal.
For the 200 mm oscillation in 0.17 m/s current, two distinct peaks are observed, one at the acceleration's maximum and one at the velocity's maximum. In 0.06 m/s current, only a distinct top is observed at the acceleration's maximum and at the velocity's maximum, only a shoulder is distinguished. It is evident that the higher current velocity causes a top at the velocity's maximum. Bernouilli's relation between the pressure and the squared velocity causes that the peaks are profound at large oscillation's amplitudes. Bernoulli's pressure approximation for a 200 mm 0.31 Hz oscillation without current is 80 Pa. A current of 0.06 m/s and 0.17 m/s increases this to 105 Pa respectively 162 Pa. The difference between 0.06 m/s and 0.17 m/s is thus 57 Pa, which is in the same order of magnitude as the tops of both runs. In other words, the combined velocity is required to properly establish the pressure and K^+ may be a useful parameter for describing the flow pattern.

Top height increase The tops of the 40 mm, 60 mm and 100 mm oscillation in 0.17 m/s current show an increase of approximately 15 Pa compared to their zero-current counterpart. Approximating the pressure

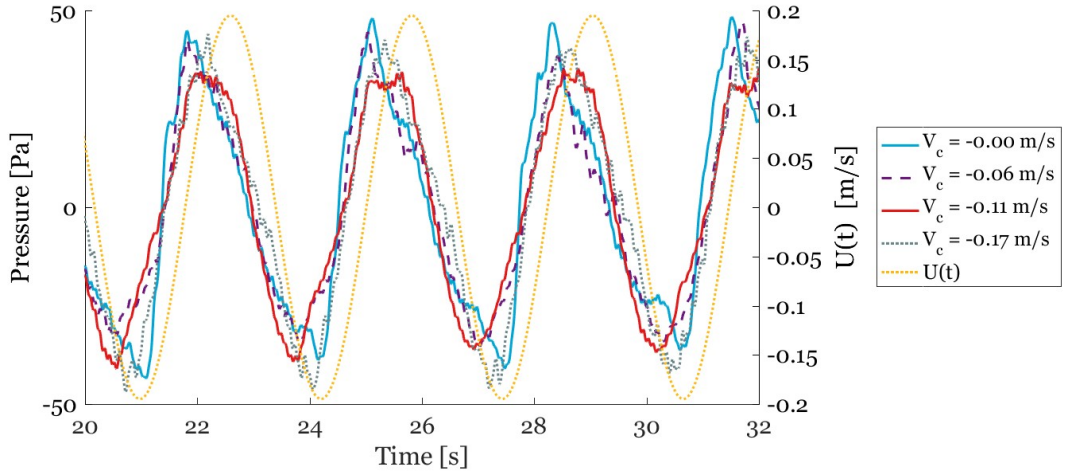

(a) P3-FS of the flat plate in 100 mm sway oscillation at 0.31 Hz with V_c = 0.00, 0.06, 0.11 and 0.17 m/s

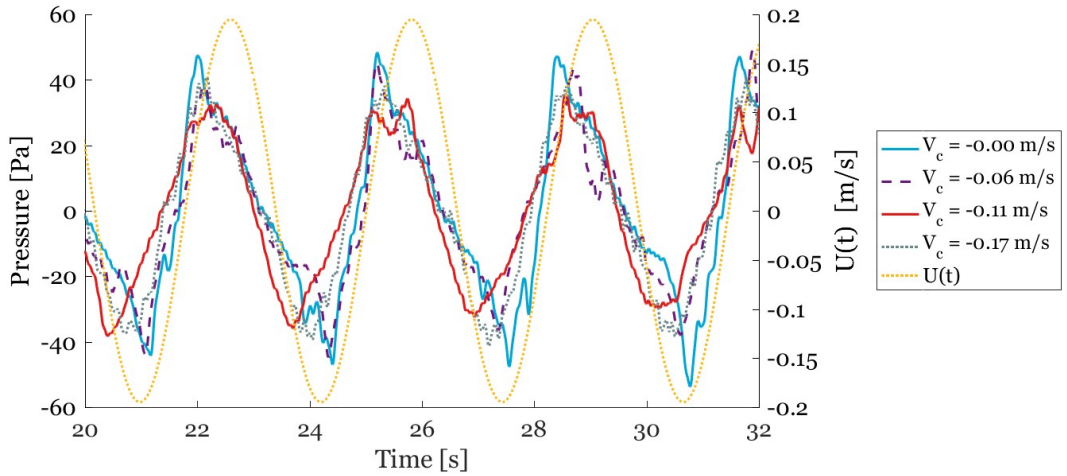

(b) P4-FS of the flat plate in 100 mm sway oscillation at 0.31 Hz with V_c = 0.00, 0.06, 0.11 and 0.17 m/s

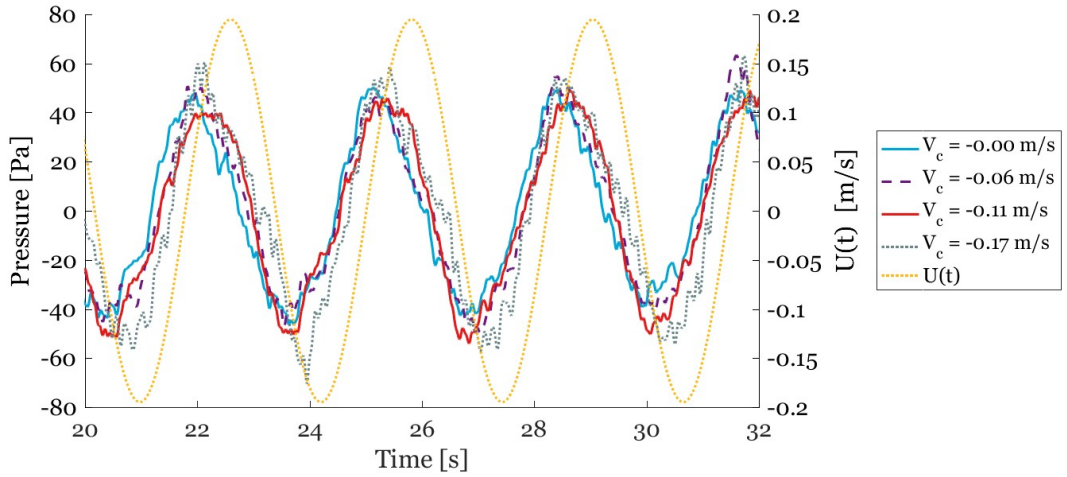

(c) P5-FS of the flat plate in 100 mm sway oscillation at 0.31 Hz with V_c = 0.00, 0.06, 0.11 and 0.17 m/s

Figure 6.5: FS-sensors' time traces in 100 mm sway oscillation at 0.31 Hz in various current speeds

with Bernoulli law gives: $1/2\rho V_c^2$ = 14.5 Pa for a 0.17 m/s current which has the same order of magnitude than the found increase.
The pressure difference in 0.06 m/s and 0.11 m/s current is less distinct. Also the 200 mm oscillation shows less definite differences in top height. The influence of the current is smaller for these cases. A reasonable explanation for the irregularity of the top height in the 40 mm oscillation is the high signal to noise ratio of this case.

Ambient dynamic pressure In 0.17 m/s current, the oscillation velocities of the cases with amplitudes of 40 mm and 60 mm are smaller than the current velocity. Their oscillation velocities are 0.08 m/s respectively 0.12 m/s. This makes that on the FS-sensors always a positive combined velocity is acting, so no wake-side pressures are observed. The FS-signal of P3 and P4 of the 40 mm oscillation is always positive. The 60 mm case shows only small negative pressures. Only P5 of the 40 mm case shows distinct negative pressures. The occurrence of negative pressures although only positive velocities are acting on the sensors is remarkable, although these pressures are small. It shows that a dynamic pressure lowers the pressure in the ambient flow.

6.3. Force history

The pressures discussed in the previous section gave an impression of the local flow behaviour. This section discusses their impact: the actual forces on the blade. It starts off with a discussion on the loads measurement in current-only conditions. Thereafter, the time traces of oscillations in various current velocities are compared. In the last subsection, the usability of the Morison model for oscillations in current is discussed.

6.3.1. Current-only measurements

The measurements in a constant current only are executed to assess individual impact of the current. It is not expected that combining the loads measured with the oscillation experiment and the loads due to a current only predict the loads in a co-existing flow field. Nonetheless, a load estimate of the separated flows broadens the insights in the loads. The current in the tests is always acting perpendicular to the rudder blade. Table 6.2 presents the measured loads of three current velocities for both models. Also, the current loads estimated with the drag equation

$$F_{d,cur} = \frac{1}{2}\rho C_{d,Vc} S_0 V_c^2 \tag{6.4}$$

are denoted to validate the experiment. According to White (2011), a drag coefficient of 1.2 is sufficient for the flat plate. For the lift profile, a coefficient of 1.1 is found by Sheldahl and Klimas (1981). The results in the table show conformity. The pressure measured in steady flow of 0.17 m/s is 15 Pa for P3. Integrating this pressure over the rudder blade results in a load of 0.35 N, showing an agreement between the measured pressures and forces.

Table 6.2: Loads in constant current only, acting perpendicular to the rudder's blade

	Flat plate		**Lift profile**	
V_c	Measured F_y	Estimated F_y	Measured F_y	Estimated F_y
0.06 m/s	0.04 N	0.05 N	0.04 N	0.05 N
0.11 m/s	0.20 N	0.17 N	0.18 N	0.16 N
0.17 m/s	0.44 N	0.41 N	0.40 N	0.37 N

6.3.2. Observations of current velocities' influences

Figure 6.6 shows the force-histories of a 100 mm sway oscillation in different current velocities. The figure shows clear differences in top- and trough height. In 0.11 m/s and 0.17 m/s current, the loads are significantly higher. Most experiments with co-existing flow fields and a significant current's influence ($\Lambda > 0.5$), showed higher tops- and troughs in the force history. However, not all cases show an agreement on this theory, for example the results of a 60 mm oscillation at 0.62 Hz, presented in figure 6.8. No large differences between the force-histories with a non-zero current are observed, and the force-history with 0.17 m/s current seems even slightly smaller than the signals in 0.06 m/s and 0.11 m/s current. The general uncertainty of the experiments is discussed in chapter 4. Here it is stated that similar runs can contain variations in top- and trough height up to 0.4 N for a 60 mm 0.62 Hz oscillation and 0.3 N for a 100 mm 0.31 Hz oscillation.

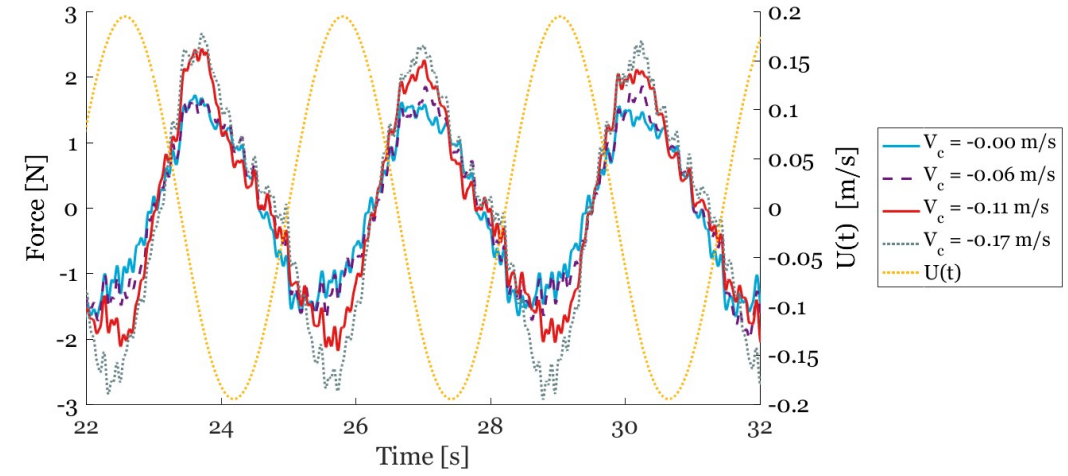

Figure 6.6: Force history of the flat plate in 100 mm sway oscillation at 0.31 Hz with V_c = 0.00, 0.06, 0.11 and 0.17 m/s

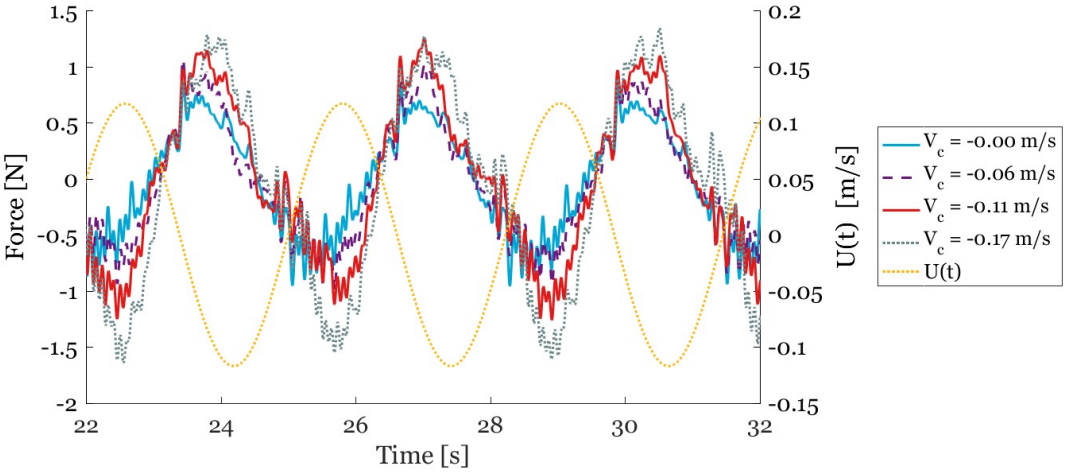

Figure 6.7: Force history of the flat plate in 60 mm sway oscillation at 0.31 Hz with V_c = 0.00, 0.06, 0.11 and 0.17 m/s

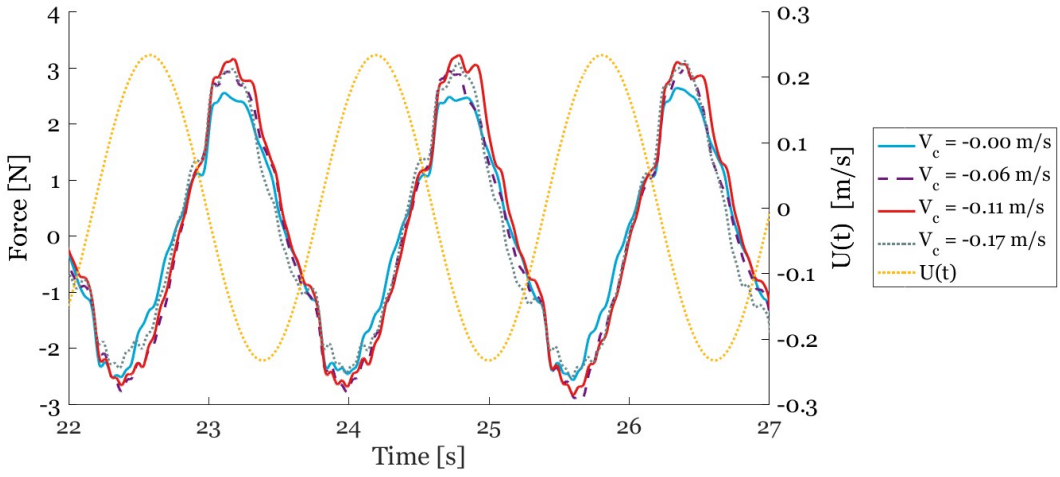

Figure 6.8: Force history of the lift profile in 60 mm sway oscillation at 0.62 Hz with V_c = 0.00, 0.06, 0.11 and 0.17 m/s

The previous subsection showed a current-only load of mostly 0.4 N. It is thus likely that the influence of the current is, at least partly, within the uncertainty bandwidth of the experiment. However, chapter 4 likewise declared the minor influence of the top-height uncertainty on the load coefficients. An analysis of the load coefficients is therefore included nonetheless in section 6.4.
In figure 6.7 the signals contain much noise. In spite of that, two observations are distinguished. Firstly, the force history of the oscillation in 0.17 m/s current shows a much larger asymmetry than the other force-histories do. Secondly, the tops- and troughs of these cases are slightly shifted towards the moment of maximum velocity. This indicates a larger influence of the drag, governed by the formation and shedding of eddies. Generally said, the current's influence is minor. The signal's courses are nearly symmetrical, even for cases in which the current velocity is larger than the maximum oscillation's velocity. This is a striking result, especially as Sarpkaya and Storm (1985) discovered the opposite: they found a large asymmetry in the force-histories of cylinders. The present work reveals that the impact of the current is surprisingly small.

6.3.3. Morison fits

The 'relative velocity' Morison model is often found better applicable for co-existing flow fields than the normal Morison model (Sarpkaya and Storm, 1985) (Li, 1989). It uses the 'combined velocity' $(V_c+U(t)|V_c+U(t)|$. This obviously causes a asymmetric load prediction. Two runs of sway oscillations in current are shown in figure 6.11. Both graphs display the load predictions by both the 'relative velocity' Morison model and the Morison model depending on the oscillation flow only. The normal Morison model clearly shows more resemblance than the 'relative velocity' Morison model, which is not a surprising result regarding the symmetrical force history. Nonetheless, it is highly unexpected regarding studies of cylinders in co-existing flow fields (Sarpkaya and Storm, 1985).

Besides that, the pressure sensors' signals showed significant wake-biasing effects due to the current. To validate the results, the pressure measured at P3 is integrated over the rudder's blade. The FS-signal and the AS-signal of P3 are subtracted from each other, through which a time trace of the 'resultant' pressure over the model's midpoint is obtained. This pressure difference is multiplied by the blade area: the rudder's span times its chord. Figure 6.9 shows a proper resemblance between the measured force and the integrated pressure. This confirms the observation that the loads are not asymmetrical, although this is reported repeatedly for cylinders.

The question arises where this thorough difference originates from. Obviously, cylinders and flat plate hold completely different separation patterns and load coefficients. Separation takes places around an oscillating flat plate already at very low KC numbers. Moreover, the vortices are shed distinctively at the plate's edges. Vortex-shedding around a cylinder requires a minimum undisturbed flow velocity. The flat plates' drag coefficients found by Keulegan and Carpenter (1958) can be four times as large as cylinders' drag coefficients for KC < 20. Both the flat plate's and the cylinder's inertia coefficients have an equal order of magnitude as the cylinder's drag coefficient. The drag component is thus larger for flat plates. Further, the drag is governed by vortex separation. Current can cause larger vortices due to the larger undisturbed velocity, but it may also drag the vortices along with the current. This can lower the suction force of the vortices, and with that lower the forces on the model. For a flat plate, dragging of vortices may be more profound than for cylinders, as the effect of the vortex shedding is simply larger for plates.

Although the symmetry of the loads on the rudder model are surprising regarding loads found on cylinders, the results are valid. They reveal that striking differences in load patterns exist between cylinders and plates, peculiarly in co-existing flow fields.

6.4. Load coefficients

Section 6.3 stated that the normal Morison model gives better load predictions than the 'relative velocity' Morison model for the rudder model in current. Both the cycle-averaged load coefficients as the instantaneous, pressure dependent, load coefficients presented in this section are therefore determined by the same means as in zero-current conditions.

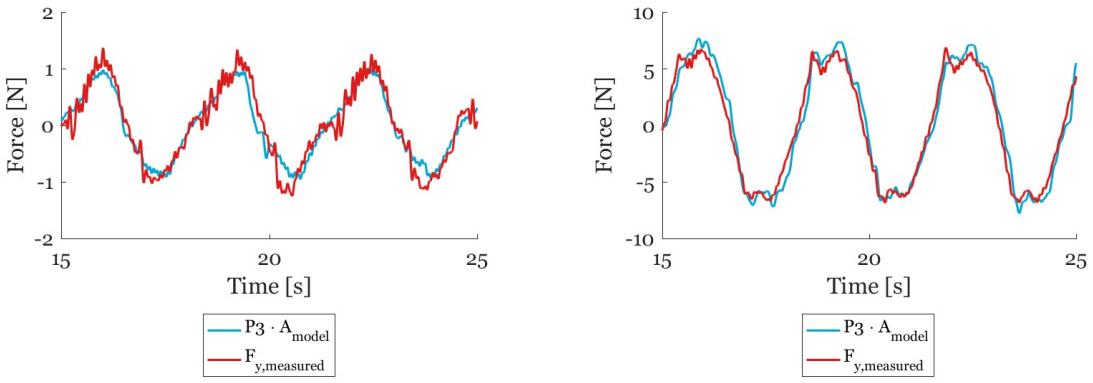

(a) Force history and P3 times the blade area for KC = 3.0 and V_c = 0.11 m/s

(b) Force history and P3 times the blade area for KC = 12.6 and V_c = 0.11 m/s

Figure 6.9: Agreement between the force measured by the load cells and the integrated pressure difference of P3

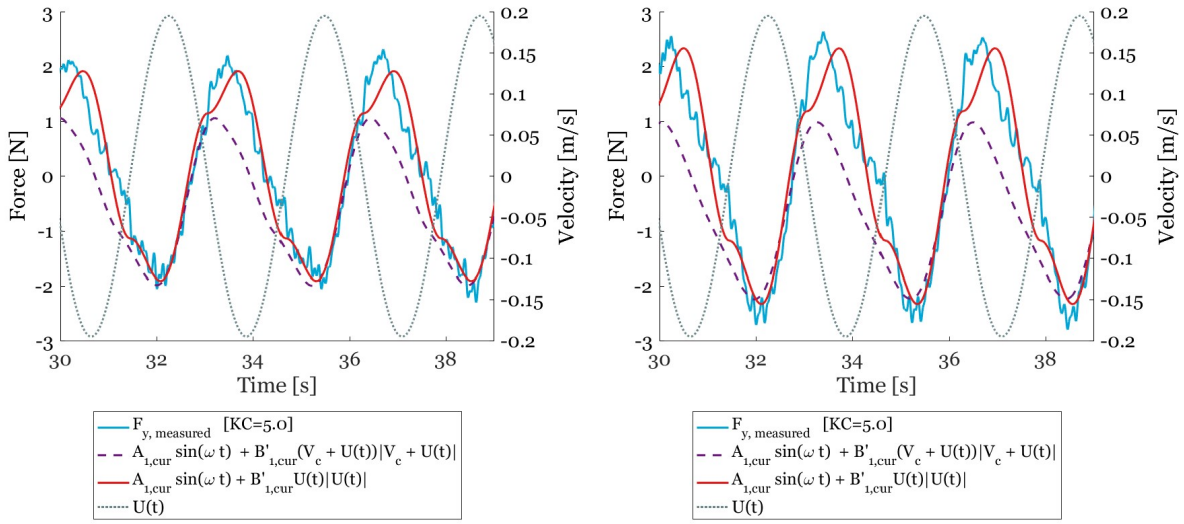

(a) Morison fits of 100 mm oscillation in 0.11 m/s current

(b) Morison fits of 100 mm oscillation in 0.17 m/s current

Figure 6.10: Morison fits of loads in co-existing flow fields

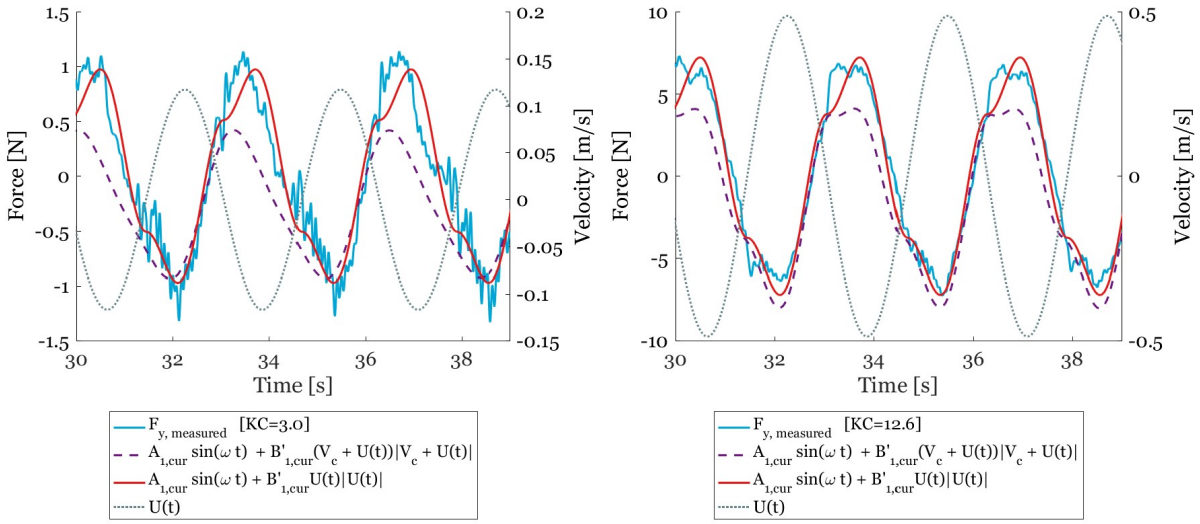

(a) Morison fits of 60 mm oscillation in 0.11 m/s current

(b) Morison fits of 250 mm oscillation in 0.11 m/s current

Figure 6.11: Morison fits of loads in co-existing flow fields

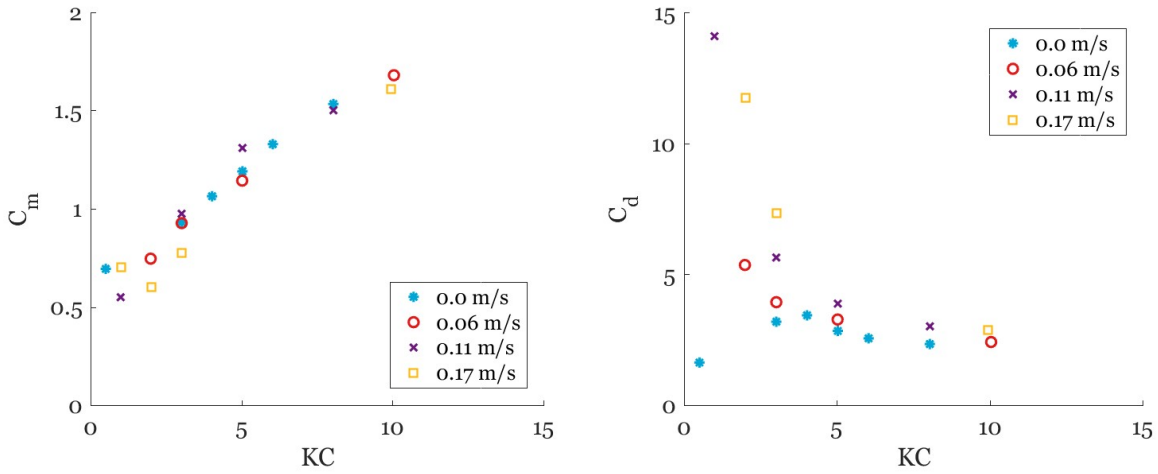

(a) Cycle-averaged inertia coefficients of oscillations at 0.31 Hz in current

(b) Cycle-averaged drag coefficients of oscillations at 0.31 Hz in current

Figure 6.12: Cycle-averaged load coefficients of oscillations at 0.31 Hz in current with the flat plate model

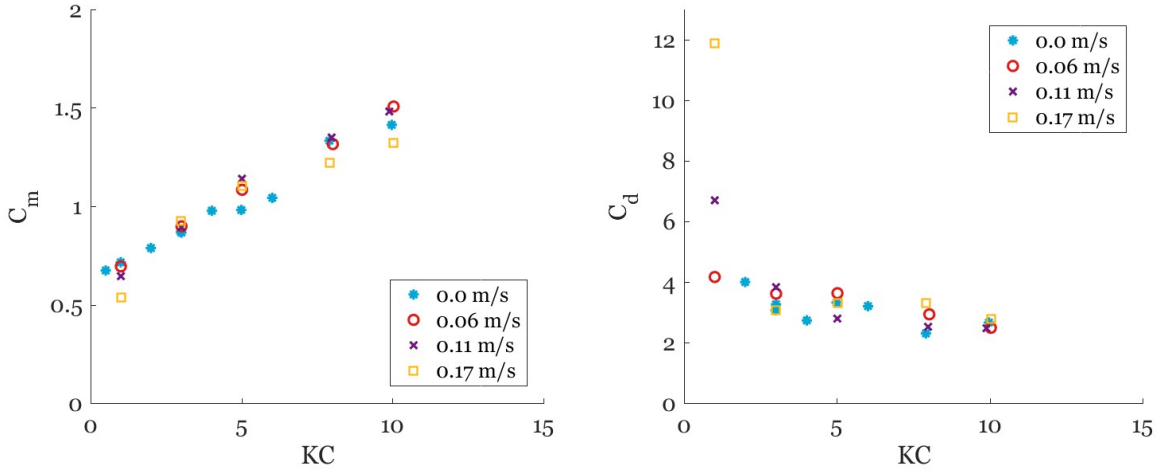

(a) Cycle-averaged inertia coefficients of oscillations at 0.62 Hz in current

(b) Cycle-averaged drag coefficients of oscillations at 0.62 Hz in current

Figure 6.13: Cycle-averaged load coefficients of oscillations at 0.31 Hz in current with the flat plate model

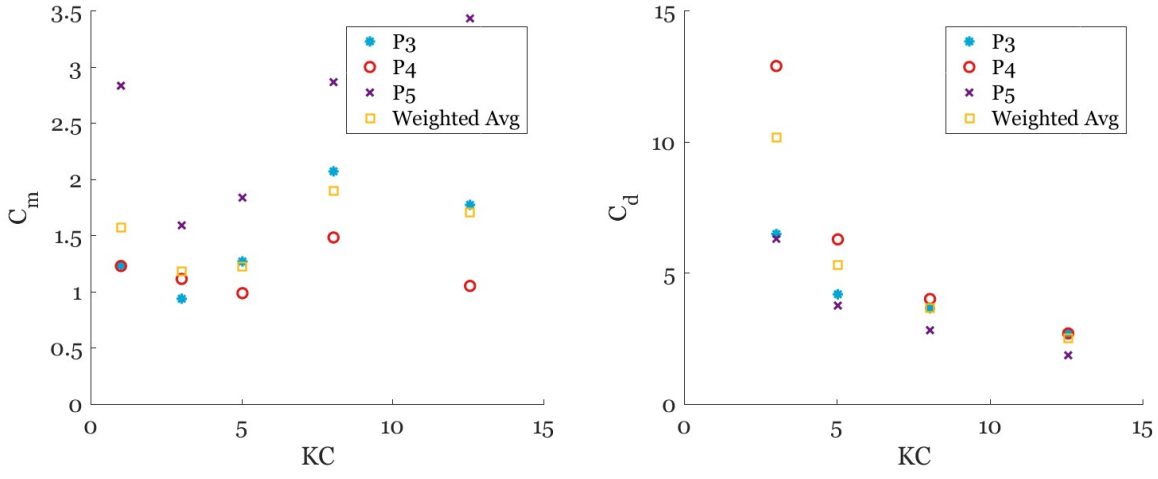

(a) Instantaneous inertia coefficients of oscillations at 0.31 Hz in 0.11 m/s current

(b) Instantaneous drag coefficients of oscillations at 0.31 Hz in 0.11 m/s current

Figure 6.14: Instantaneous load coefficients of oscillations at 0.31 Hz in 0.11 m/s current

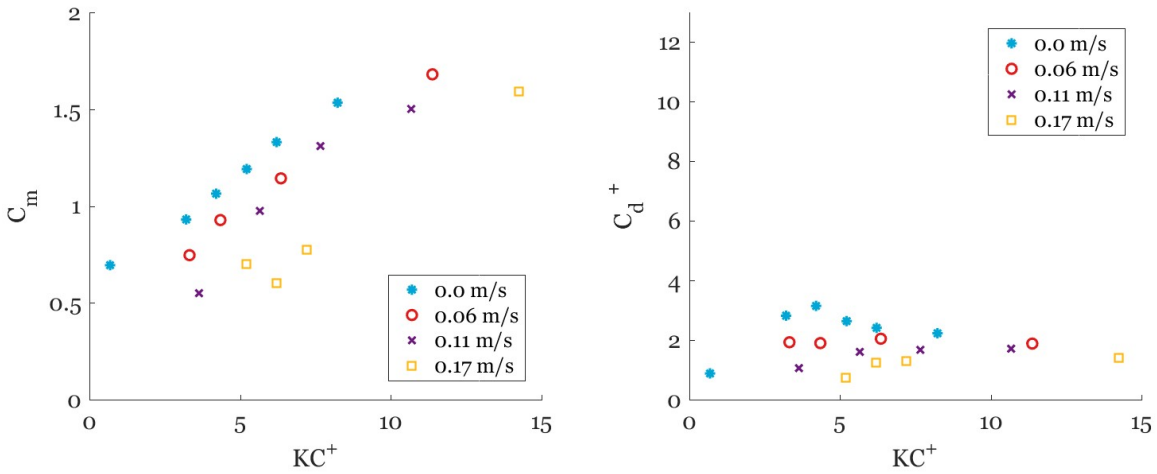

(a) Cycle-averaged inertia coefficients of oscillations at 0.31 Hz in current presented against K^+

(b) Cycle-averaged drag coefficients of oscillations at 0.31 Hz in current presented against K^+

Figure 6.15: Load coefficients of 0.31 Hz oscillations of the flat plate model in various current speeds presented against K^+

6.4.1. Inertia coefficients

Figure 6.12a and figure 6.13a draw the inertia coefficients of oscillations in current relative to the KC number. For both the 0.31 Hz oscillation as the 0.62 Hz oscillation a clear trend is present. The variations between the coefficients for the different the current velocities are marginal and fall within the uncertainty bandwidth. The instantaneous inertia coefficients for oscillations in 0.11 m/s current are presented in figure 6.14a. The trend is less clear, but the coefficients have the same order of magnitude and all lay between 1 and 2. The cycle-averaged coefficients have magnitudes between 0.5 and 1.5.

The inertia coefficient is also plotted versus the K^+ parameter. For current conditions, K^+ has a larger magnitude than the normal KC number. This shifts the coefficients obtained under current conditions to the right. This presentation increases the deviation of the coefficient. This is a likely occurrence as the inertia coefficient should not be dependent on the current. For use in engineering practices, the most straightforward presentation is preferred, which is the normal KC number.

6.4.2. Drag coefficients

Figure 6.12b and figure 6.13b draws the drag coefficients of oscillations in current relative to the KC number. Figure 6.12b shows that the drag coefficient enlarges when the current velocity increases. In figure 6.13b, the oscillations at 0.62 Hz, a similar trend is observed, although some coefficients show deviations. The smaller the oscillation's velocity or KC number, the larger the drag coefficient's increase.

The instantaneous drag coefficients of the flat plate in 0.31 Hz oscillation in 0.11 m/s current are shown in figure 6.14b. The presented trend is surprisingly clear and similar to trends found in literature. All sensors follow the increase of the drag coefficient when KC drops. The weighted average of the drag coefficients is even a bit larger than the drag coefficients found by Ridjanovic (1962). This is foreseen as the 2-coefficient Morison equation underestimates the peak load. These peaks are used to determine the magnitude of the instantaneous coefficients so they are expected to be a little larger than the cycle-averaged coefficients.

The drag is plotted versus K^+ in figure 6.15b and figure 6.16b. The Fourier coefficient is divided by $(|V_c| + U_m)^2$ instead of U_m^2 and thus uses the current velocity in its definition. This may represent the loads more in line with their physical behaviour, as the K^+ regime is believed to govern the drag loads. The graphs distinctively show different trends. All the coefficients are smaller than 4 and generally, the larger the current, the smaller the coefficient. The trends in 0.11 m/s and 0.17 m/s current are nearly horizontal.

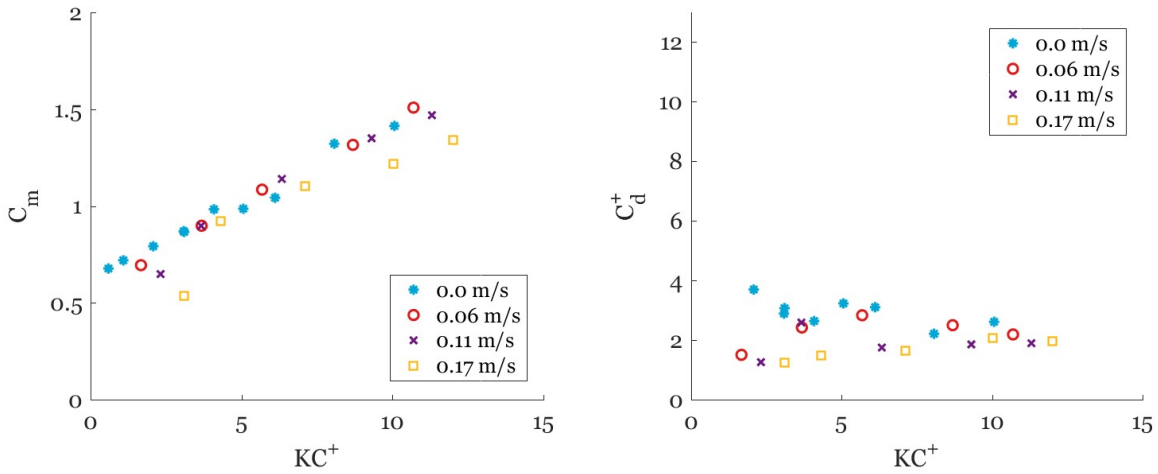

(a) Cycle-averaged inertia coefficients of 0.62 Hz oscillations in current presented against K^+

(b) Cycle-averaged drag coefficients of 0.62 Hz oscillations in current presented against K^+

Figure 6.16: Load coefficients of 0.62 Hz oscillations of the lift profile in current presented against K^+

6.4.3. Higher order coefficients

The third- and fifth order coefficients of the flat plate in 0.31 Hz oscillation and the lift profile in 0.62 Hz oscillation are included in appendix G. Like in zero-current conditions, reasonable trends are distinguished. It is due to this, that the applicability of the Morison model in its 6-coefficient form is feasible.

6.5. Discussion

The main objective of this chapter was to propose a load prediction model for the rudder in co-existing flow fields of sway oscillations and planar current. To do so, the loads in this conditions are quantified by force measurements and explained by pressure measurements.

The load prediction by the 'relative velocity' Morison's model did not show good comparison with the measured loads. This is a striking result, as this model is often recommended for cylinders in similar flows. It appeared that the more heavily separating flow around the sharp edged models caused a significantly different load pattern than observed for cylinders. It is due to the nearly symmetrical force history, that the Morison model that ignores the current, predicts the loads the most accurate.
The inertia coefficients obtained in oscillation with current conditions did not show clear differences. However, a clear increase of the drag coefficient is observed for an increasing velocity parameter. Mainly the drag, which governed by separation and vortex generation, is thus altered by the current. More resemblance between the drag coefficient is observed, when they are presented against the K^+ numbers and moreover non-dimensionalized with both the oscillation velocity and the current. The pressure signals showed large gradients in the wake, indicating an extensive wake area governed by shedding eddies.

For very small amplitude oscillations in large current, the quality of the fit reduces. However, in engineering applications, heavy loading situations are more relevant. For heavy load cases, the large amplitude oscillations and large currents, the prediction with the Morison's model is satisfactory. The prediction model in low-speed currents may be highly relevant, as Sarpkaya and Storm (1985) suggests that wave orbital motions and currents have similar effects on the drag coefficients as they both cause wake-biasing. He regarded them both as 'primary mitigating effects of the ocean environment'. The loads of the oscillations with current may thus be more effective in predicting the loads.

The striking difference between cylinders and plates shows the need for extensive research on this topic. The detailed insights in the wake-biasing is required to fully understand the loads on the rudder.

7

Conclusions

Offshore moored FPSO's face many challenges with rudder-locking. Little is known of the load-magnitude that FPSO-rudders have to endure while moored. The loads caused by waves oscillations and currents are expected to be complex and governed by flow separation. This study started off with the question whether it is possible to predict these complex rudder loads with a calculation model that only requires the undisturbed flow pattern and body-shape depending load-coefficients. The problem was limited to regular sway oscillation combined with a steady flow, acting perpendicular to the rudder's blade.

The results of the towing tank experiments show that only the Morison model - extended with the third and fifth term of its Fourier's expansion – gives an appropriate description of the force history in sway oscillation. The regular 2-coefficient form of the Morison model underestimates the peak loads, which is of vital importance. It is only due to the peak loads possible to study the fatigue and ultimate strength of the rudder locking system.
When flow fields of sway oscillations and currents perpendicular to the rudder's blade are combined, the 'relative velocity' Morison model – depending on both flow velocities – is expected to present the most accurate load prediction. However, the model shows large discrepancies with the measured force histories. This is a striking result, as the 'relative velocity' Morison model is found best applicable in similar studies to cylinders. The measured force histories are - despite the presence of the current - surprisingly symmetrical over the oscillation' cycle. Therefore, the Morison model which does not take currents into account, presents better results.

In order to use the Morison model, empirical coefficients are required. These coefficients depend on the Keulegan-Carpenter (KC) number: a dimensionless number which magnitude is a direct measure of vortex generation around bodies in oscillating flow. The larger the oscillation's amplitude, the more vortices are generated and the higher the KC number's magnitude. The influence of the vortex generation and -shedding on the loads cannot be stressed enough. The frequency independence found in this study substantiates this.

The rudder's aspect ratio of 1.5 allows vortex separation around all four edges. Compared to the coefficients of infinite length flat plates, the magnitude of both inertia- and drag coefficient is lowered by a factor two. This indicates substantial pressure losses in the wake of the rudder models. The lift profile and the flat plate profile show comparable results. Clear trends between the third- and fifth order load coefficients and the KC number can be distilled: pressure sensors showed a significant enlargement and increased irregularity of wake peaks when the draught decreased. The influence of the free surface vicinity was found of little importance on the loads and often fell within the uncertainty bandwidth. Nonetheless, the loads' irregularity may enlarge, causing a functional decrease of the Morison model's predictions.

Oscillations with a non-uniform velocity profile over the rudder's span are likely in ocean environments. Unfortunately, the results of the roll oscillation experiments could not be relied on. Therefore, the test set-up is found insufficient to measure these loads.

8

Recommendations

This study demonstrated the complexity of the loads on a rudder in sway oscillation. Unfortunately enough, the experiments suffered from large inertia corrections, through which the results of the roll oscillations were unreliable. The sway oscillations showed a large sensitivity regarding the inertia corrections and a miscalculation of the inertia's phase with a few hundredths of a second could cause major differences in the drag coefficients' magnitude. The most striking recommendation is to execute similar experiments with a higher accuracy.
A different test set-up is then required. A set-up in which the rudder is placed in the water like a pendulum could be though of. Also, a very small six component frame exists, with dimensions of approximately 5x5x5 cm. Its use may solve the challenges with the large inertia.

A number of additions to the test matrix are recommended to fill more knowledge gaps. These consist of executing oscillation experiments in omnidirectional currents, in low-draughts and surface piercing conditions and irregular waves. The moment around the rudder stock is moreover relevant for the mechanical rudder-locking.

The currents are only tested while acting perpendicular to the rudder's blade. Currents can act under any angle on the rudder in ocean environments. This may alter the vortex pattern caused by the oscillation, which may alter the loads. When currents act on the rudder under an angle, additional effects may rise, such as an increased influence of viscous forces. Oscillations in an omnidirectional current are striking load cases which need additional research. The current's angle may however enlarge the difficulty of finding a suitable load prediction model.

The pressure sensors indicated that the influence of the free surface's vicinity is significant. This is a very likely case for a FPSO to encounter. In fully loaded condition, the rudder root is just below the water surface. More experiments are required to fully assess this condition. In ballast condition, the rudder may even be piercing the water surface. This gives rise to even more free surface disturbances and eventually additional loads like wave run-up and slamming. These loads, especially in combination with the wave- and ship motion-induced loads, can cause high peak loads on the rudder- and rudder-locking system. Attention is required.

The moment around the rudder stock is of mayor importance for the mechanical locking of the rudder. Rudders are often designed such that they are balanced in sailing conditions: the moment around the rudder stock is then minimized. In moored conditions, vortices are shed around both edges. Due to the rudder's asymmetry, it is likely that the center of action for the moment around the rudder stock is not in the rudder's geometrical center, but tends towards the trailing edge. Unfortunately enough, the measured moment around the rudder stock was too noisy for investigations. Studies towards the moment around the rudder stock are recommended.

In other researches it was shown that irregular oscillations, may be significantly different than similar amplitude, regular oscillations. It is evident that a FPSO will encounter such a situation at sea; therefore clear insights in the effects of non-linear waves are required for a proper load prediction. Irregular oscillation experiments are executed in this study as well. They are not used for analysis, as the load were too inaccurate; a significant spread in the top- and trough heights were already found in regular oscillations.

This study was limited by experimental tests. CFD simulations can give additional insights in the loads, and may predict them with even more detail. It is therefore recommended to executed CFD experiments in all oscillation cases encountered in this study. Furthermore, after the loads on a single rudder are simulated, a complete (aft-) hull form can be tested as well. With this, hull diffraction and eventually radiation can be taken into account as well, resulting in more realistic rudder loads.

A not rudder-loads-related recommendation originates from the vertical rudder oscillations. These give rise to a sceptic view about the phase accuracy of the motion camera with regards to the measured loads. One cause may be the difference in sampling frequency. Tests should be executed to prove whether or not this presumption is true.

A

Geometry of models

A.1. NACA0020

[h] The NACA 4-digit-series lift profile shapes are described by the following equation:

$$\frac{y}{c} = a_0\left(\frac{x}{c}\right)^{1/2} + a_1\left(\frac{x}{c}\right) + a_2\left(\frac{x}{c}\right)^2 + a_3\left(\frac{x}{c}\right)^3 + a_4\left(\frac{x}{c}\right)^4 \tag{A.1}$$

In this equation y points in direction of the thickness, c is the chord length and x points along the chord of the rudder. The coefficients are determined as: $a_0 = 0.2969$, $a_1 = -0.1260$, $a_2 = -0.3516$, $a_3 = 0.2843$ and $a_4 = -0.1015$. Without any multiplication of all y/c numbers, the thickness over chord ratio is 0.20.

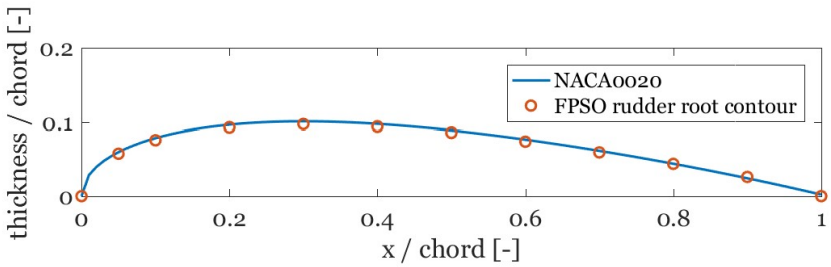

Figure A.1: Plot of rudder contours; the NACA0020 shows good agreement with the simplified contour plot of a FPSO's rudder (Ladson *et al.*, 1996) (Hyundai Heavy Industries, 2014)

Table A.1: NACA0020 x- and y coordinates for 125 mm chord length model

x	y	x	y
0	0	63.82	10.825
1.251	3.566	65.071	10.683
2.503	4.939	66.322	10.537
3.754	5.944	67.574	10.387
5.005	6.754	68.825	10.232
6.257	7.437	70.076	10.074
7.508	8.028	71.328	9.912
8.76	8.547	72.579	9.746
10.011	9.008	73.83	9.576
11.262	9.421	75.082	9.403
12.514	9.791	76.333	9.226
13.765	10.125	77.585	9.046
15.016	10.427	78.836	8.862
16.268	10.699	80.087	8.676
17.519	10.945	81.339	8.486
18.77	11.168	82.59	8.292
20.022	11.368	83.841	8.096
21.273	11.547	85.093	7.897
22.525	11.708	86.344	7.694
23.776	11.851	87.595	7.489
25.027	11.977	88.847	7.281
26.279	12.088	90.098	7.07
27.53	12.184	91.35	6.856
28.781	12.266	92.601	6.639
30.033	12.334	93.852	6.419
31.284	12.39	95.104	6.196
32.535	12.435	96.355	5.971
33.787	12.468	97.606	5.742
35.038	12.49	98.858	5.511
36.29	12.501	100.11	5.277
37.541	12.503	101.36	5.041
38.792	12.495	102.61	4.801
40.044	12.479	103.86	4.559
41.295	12.453	105.11	4.313
42.546	12.419	106.37	4.065
43.798	12.377	107.62	3.814
45.049	12.328	108.87	3.56
46.3	12.271	110.12	3.302
47.552	12.207	111.37	3.042
48.803	12.135	112.62	2.779
50.055	12.058	113.87	2.513
51.306	11.974	115.13	2.243
52.557	11.883	116.38	1.97
53.809	11.787	117.63	1.694
55.06	11.685	118.88	1.415
56.311	11.577	120.13	1.132
57.563	11.464	121.38	0.846
58.814	11.346	122.63	0.556
60.065	11.223	123.89	0.262
61.317	11.095	125.00	0.00
62.568	10.962		

A.2. Model geometries

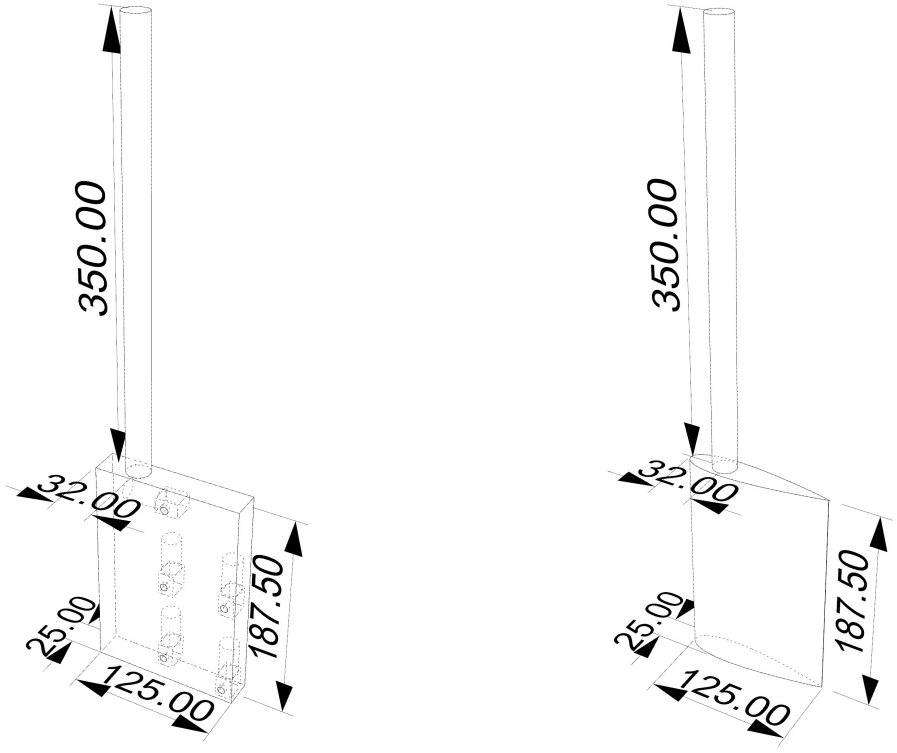

(a) Flat plate model

(b) NACA0020 model

Figure A.2: Rudder models with dimensions

A.3. Specifications TU Delft Towing Tank no. 1 and Hexamove

Towing tank no. 1 has a length of 142.00 m, a width of 4.22 m and a maximum water depth of 2.50 m. The maximum carriage speed is 7.00 m/s. The Hexamove is placed under the carriage to execute oscillations in 6 degrees of freedom. The maximum workload of the Hexamove is 200 kg. The theoretical reach for translations is about 200 mm in x-direction, about 235 mm in y-direction and about 175 mm in z-direction. The reach for rotations is about 27° around the x-axis, about 25° around the y-axis and about 30° around the z-axis. However, the reach depends on dynamic loads as well, which is governed by the mass of the model and the accelerations. (Maritime and Transport Technology, 2017b) (Maritime and Transport Technology, 2017a)

A.4. Model alignment

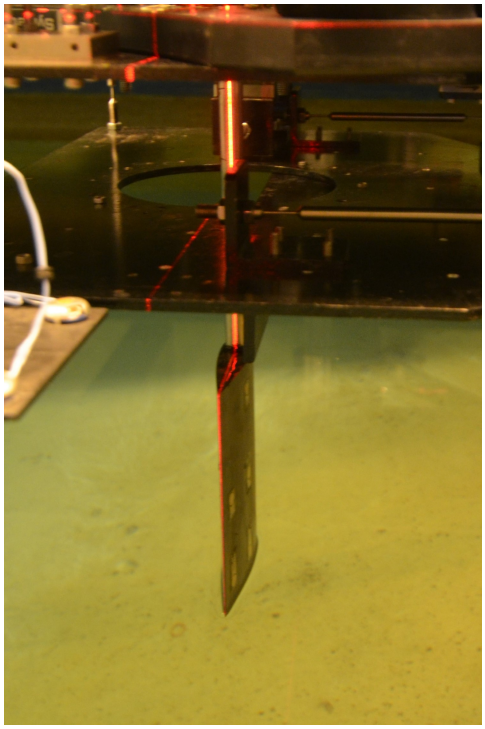

Figure A.3: Aligning the model with use of a laser

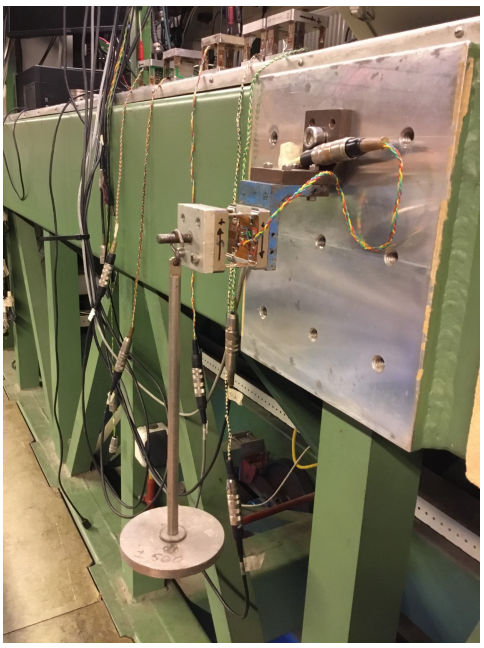

Figure A.4: Calibration set-up of load cells

A.5. Calibration of sensors

A.5.1. Load cells

As discussed in the previous subsection, The individual load cells are tested by conventional static load tests. A picture of the calibration test set-up is included in appendix A.4 figure A.4. The results of these tests are shown in figure A.5a and figure A.5b. The graphs show a very linear behaviour. The slope of the trend line determines the calibration factor. For all load cells, the deviation between the calibration factor and the measured data is 0.5 percent at most. The hysteresis of an individual load cell is negligible.

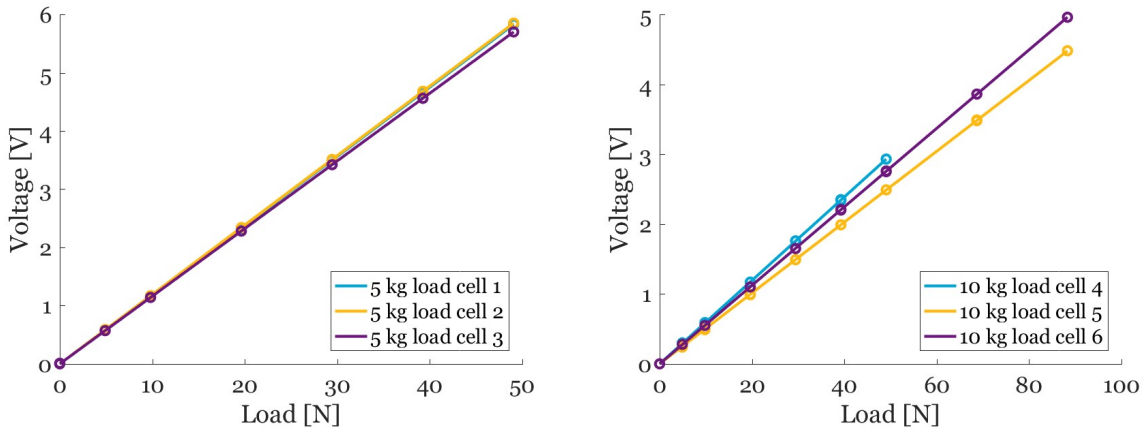

(a) Static calibration measurements of 5 kg load cells.

(b) Static calibration measurements of 10 kg load cells.

Figure A.5: Calibration measurements of the load cells.

A.5.2. Pressure sensors

The membrane pressure sensors are calibrated by hydrostatic pressure tests. Two pictures of the calibration set up is included in appendix A.4 figure A.7. The calibration measurements are shown in figure A.6. The graphs of sensor 1 and sensor 3 are not visible as their graph is exactly underneath the graphs of sensor 2 respectively sensor 5. The sensors show a highly linear behaviour. The accuracy of the calibration measurement is relatively small at lower hydrostatic pressures. This is likely to be due to inaccurate observation of the imposed pressure. These measurements are not taken into account in determining the calibration factor. The deviation between the calibration factor and the measured data is 2.5 percent at most.

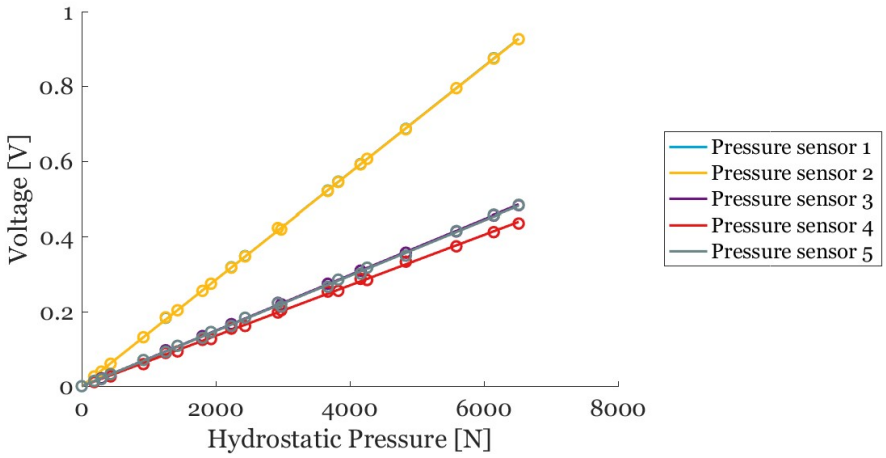

Figure A.6: Calibration measurements of the pressure sensors.

(a) Set-up in which 10 pressure sensors can be fitted

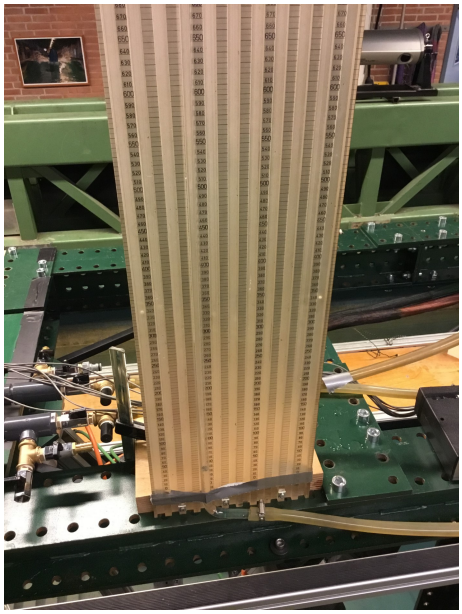

(b) Water height ruler

Figure A.7: Calibration set-up for membrane pressure sensors

B

Signal corrections

B.1. Butterworth filter

The signals measured by the load cells and the pressure sensors both contain noise. Therefore, the signals need to be filtered. The motions measured with Certus do not contain visible noise, but the signal sometimes shows small discrepancies. These are barely noticeable when observing the motion signal, but when the motion signal is differentiated to the velocity or acceleration, large peaks can be observed at the discrepancy's moment. Filtering the motion signal avoids these peaks.

Filtering of all signals is done with a Butterworth filter. This filter design is known for its 'maximally flat' behaviour (MathWorks, 2018). This means there are no 'ripples' generated in the gain-function (which is related to the transfer function) before the cut-off frequency. This behaviour is illustrated in figure B.1. In this figure, a gain-function is of a Butterworth low-pass filter is shown. Before the cut-off frequency, which is at $f/f_0 = 1$, the gain function does not show ripples and is very flat.
The order of the function determines the steepness of the filter. In figure B.1, the different orders of the function are shown by graphs A to E, with A being the lowest order and E the highest order. The steepness of the function is known as the roll-off rate. Figure B.1 shows a low-pass filter; a filter that passes low frequencies and cuts off high frequencies. The maximum cut-off frequency is the Nyquist frequency, which is defined as half of the sampling rate. Above this frequency, no filtering is possible because of aliasing (Holthuijsen, 2007). A consequence of filtering is the generation of a phase lag of the signal. This phase lag is numerically corrected with use of Matlab's 2016a filtfilt function.

Besides high frequency noise, low frequency noise may be present in the pressure- and load cell signals

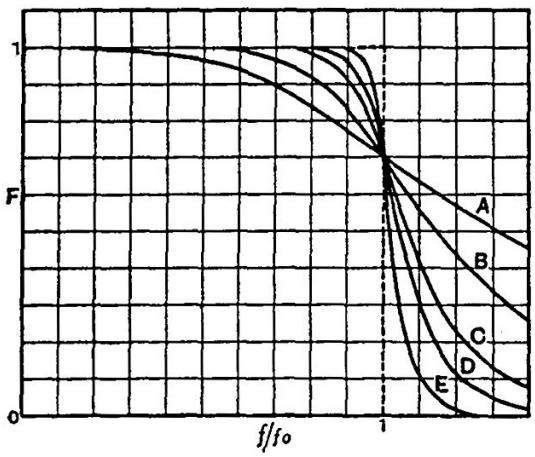

Figure B.1: Butterworth filter design of several orders. Adapted from Butterworth (1930).

as well. Low frequency noise can be added by low frequency waves in the towing tank. Due to the numerous tests during the day or even the week, low frequent waves can be generated. These are hardly visible in the tank and the signal, but may affect the results. The low-frequent waves may be present especially for runs at the end of a test day. To account for this, a Butterworth bandpass filter is used, which filters both low frequency noise as high frequency noise.
Figure 4.1a shows the normalized spectral density of load cell F2 in y-direction during sway oscillation. The spectrum clearly shows a large peak between 0 and 4 Hz. The same trend is observed in figure 4.1b, which shows the normalized spectral density of pressure sensor P3 during the same sway oscillation. For the pressure sensor, a small peak is observed at 7 Hz and 11 Hz as well. This is probably noise. The load cell's signal also shows small peaks at 7 and 11 Hz as well, and moreover shows an increase at higher frequencies. At high frequencies, this clearly is noise. A cut-off frequency for both signals is chosen at 7 Hz. This filters the signal enough, but does not flattens the signal out too much. The signals are both sampled at 1000 Hz, which makes the Nyquist frequency equal to 500 Hz. The input parameter for the filter design is $\frac{f_{cut-off}}{f_{nyq}}$.

A lower cut-off frequency of 0.06 Hz is used. This number is determined by examining the filter's influence on the signal's mean. The signals were first corrected for their static values. Afterwards, the signals should have mean of zero, but a Fourier analysis still showed small deviations in the mean value. This can be due to low frequency noise. A cut-off frequency of 0.06 Hz minimized the deviations of the mean value, but did not influence the magnitude of the Fourier coefficients of interest much. The magnitude of the mean parameter after correction was smaller than 1/1000.

The motion signals are filtered with a low-pass filter with cut-off frequency of 1 Hz. The use of this filter is not because of the noise, but due to small ripples in the signals, which are unwanted amplified when the signal is used for further calculation.

B.2. Method of Least Squares

B.2.1. Phase correction

The motion of the model can be written is terms of a single sine with a phase ϵ_m, which is the time between the first zero-crossing of the signal and the starting time t_0 of the signal.

$$y(t) = y_a \sin(\omega t + \epsilon_m) \tag{B.1}$$

In this equation, $y(t)$ is the measured motion signal and ω the angular velocity, which is assumed constant throughout the whole measurement. Both y_a and ϵ_m are unknown for the raw data sets. They need to be known for further processing of the data. Both can be obtained with the Method of Least Squares. For this method, the equation is rewritten to a summation first, by using the angle addition formulas:

$$y(t) = y_a (\sin(\omega t)\cos(\epsilon_m) + \cos(\omega t)\sin(\epsilon_m)) \tag{B.2}$$

Equation B.2 can be written in vector formation, in which the measured time-series and known parameters can easily used as input.

$$\begin{bmatrix} \sin(\omega t_0) & \cos(\omega t_0) \\ \sin(\omega t_1) & \cos(\omega t_1) \\ \vdots & \vdots \\ \sin(\omega t_i) & \cos(\omega t_i) \end{bmatrix} \cdot \begin{bmatrix} y_a \cos(\epsilon_m) \\ y_a \sin(\epsilon_m) \end{bmatrix} = \begin{bmatrix} y(t_0) \\ y(t_1) \\ \vdots \\ y(t_i) \end{bmatrix}$$

This vector formation is basically a multiplication in the form of:

$$G\mathbf{x} = \mathbf{b} \tag{B.3}$$

The parameter $\mathbf{x}$ is a column vector of length n and $\mathbf{b}$ is a column vector of length m, which is the number of samples of a signal. The matrix A is of size $[m \cdot n\ ]$. Matrix G and column vector $\mathbf{b}$ are known from the time-series and vector $\mathbf{x}$, in our case the amplitude and phase of the signal, is unknown. There is no exact solution for vector $\mathbf{x}$, therefore the Least Squares Method tries to find the 'best fit' vector $\mathbf{x}^*$ to vector $\mathbf{b}$. This best fit can be visualized as minimizing the length of vector which denotes the difference between $\mathbf{b}$ and $G\mathbf{x}^*$ (Lay *et al.*, 2016):

$$||\mathbf{b} - G\mathbf{x}^*|| \tag{B.4}$$

The length of this vector is a summation of squares, $(b_1 - G_{1,:}{}^*)^2 + (b_2 - G_{2,:}{}^*)^2 + ...$ The name Least Squares obviously originates from this. The method thus tries to obtain a zero-vector (Lay *et al.*, 2016):

$$G\mathbf{x}^* - \mathbf{b} = \mathbf{0} \tag{B.5}$$

Via linear algebra methods, the best fit of to this zero-vector is obtained. First, both sides are multiplied with the transpose of G and subsequently rewritten (Lay *et al.*, 2016):

$$G^T\left(G\mathbf{x}^* - \mathbf{b}\right) = \mathbf{0} \tag{B.6}$$

$$G^T G\mathbf{x}^* - G^T\mathbf{b} = \mathbf{0} \tag{B.7}$$

$$G^T G\mathbf{x}^* = G^T\mathbf{b} \tag{B.8}$$

Furthermore, when matrix $A^T A$ is multiplied with its inverse, $\left(G^T G\right)^{-1}$, the identity matrix is obtained. This results in the least square fit (Lay *et al.*, 2016):

$$\mathbf{x}^* = \left(G^T G\right)^{-1} G^T\mathbf{b} \tag{B.9}$$

A solution to the amplitude and phase of the signal can thus be obtained with basic linear algebra. In terms of our initial problem as shown in equation B.1, the least squares fit of $y^*(1) = y_a \cos(\epsilon_m)$ and $x^*(2) = y_a \sin(\epsilon_m)$ is obtained. The result is thus a system of two equations with two unknowns, which can be solved.

B.2.2. Fourier coefficients

As explained in section 2.3.2, the measured force signal is assumed to be composed of a sum of sine. This is mathematically shown in equation 2.23. Assuming only the first and third term are relevant, the equation reduces. In vector formation, the equation is shown as:

$$\begin{bmatrix} \sin(\omega t_0) & \cos(\omega t_0) & \sin(3\omega t_0) & \cos(3\omega t_0) & \sin(5\omega t_0) & \cos(5\omega t_0) \\ \sin(\omega t_1) & \cos(\omega t_1) & \sin(3\omega t_1) & \cos(3\omega t_1) & \sin(5\omega t_1) & \cos(5\omega t_1) \\ \vdots & \vdots & \vdots & \vdots & \vdots & \vdots \\ \sin(\omega t_i) & \cos(\omega t_i) & \sin(3\omega t_i) & \cos(3\omega t_i) & \sin(5\omega t_i) & \cos(5\omega t_i) \end{bmatrix} \cdot \begin{bmatrix} A_1 \\ B_1 \\ A_3 \\ B_3 \\ A_5 \\ B_5 \end{bmatrix} = \begin{bmatrix} F_y(t_0) \\ F_y(t_1) \\ \vdots \\ F_y(t_i) \end{bmatrix}$$

The Fourier coefficients A_1, B_1 A_3, B_3, A_5 and B_5 can be solved with the method of Least Squares, as explained in the previous section.

C

Signal corrections

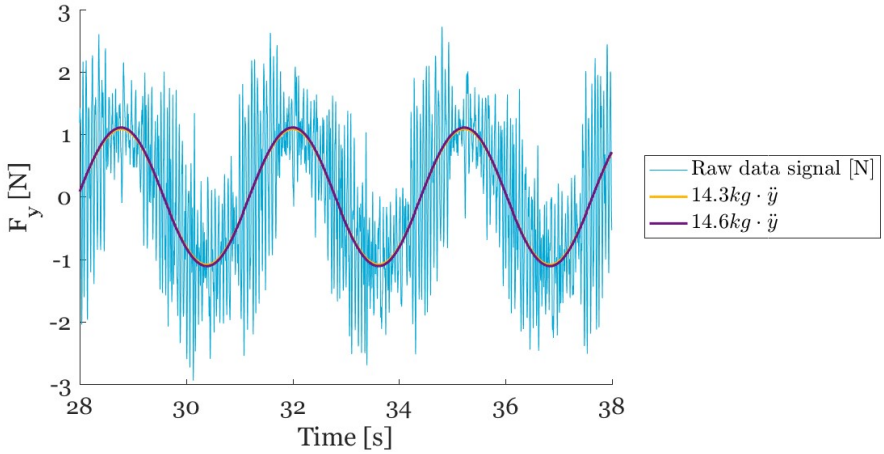

Figure C.1: Time trace of F_y of 0.31 Hz sway oscillation in air with an amplitude of 20 mm.

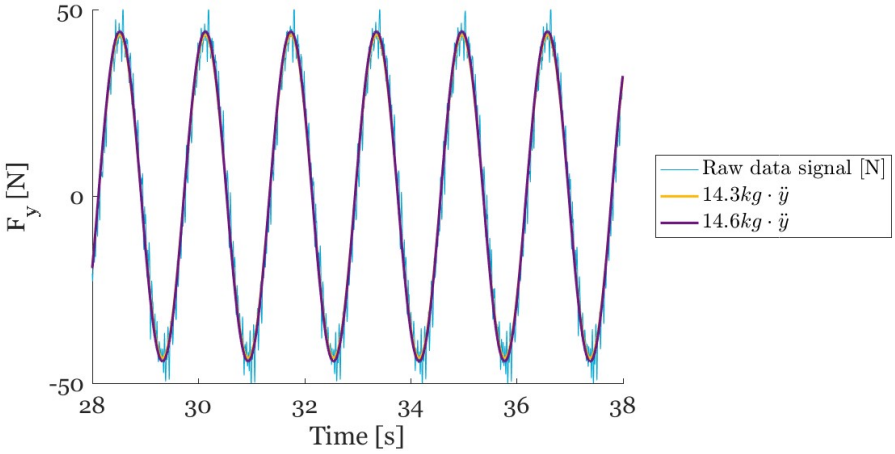

Figure C.2: Time trace of F_y of 0.62 Hz sway oscillation in air with an amplitude of 250 mm.

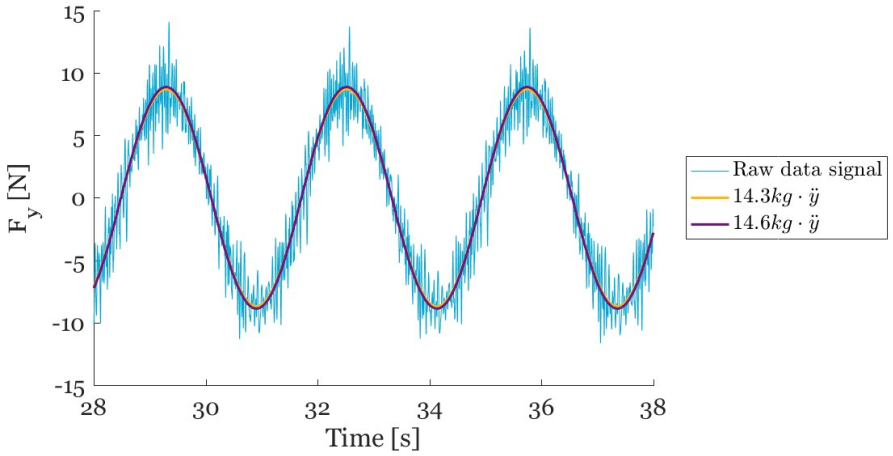

Figure C.3: Time trace of F_y of 0.31 Hz sway oscillation in air with an amplitude of 160 mm.

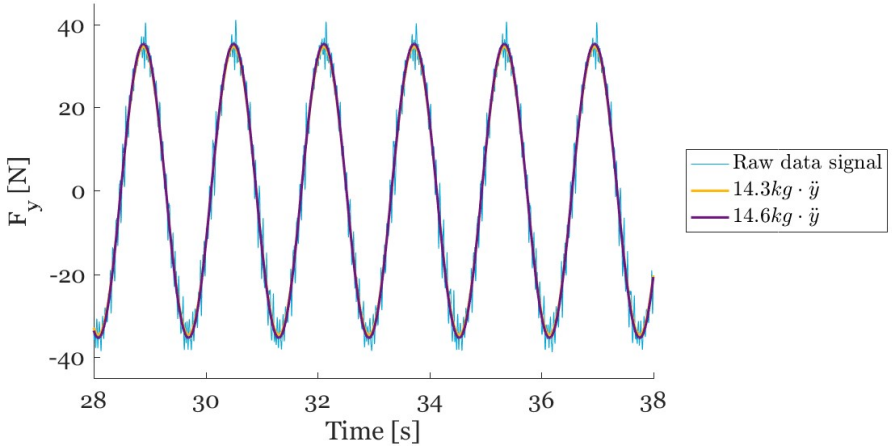

Figure C.4: Time trace of F_y of 0.62 Hz sway oscillation in air with an amplitude of 160 mm.

C.1. Pressure sensors

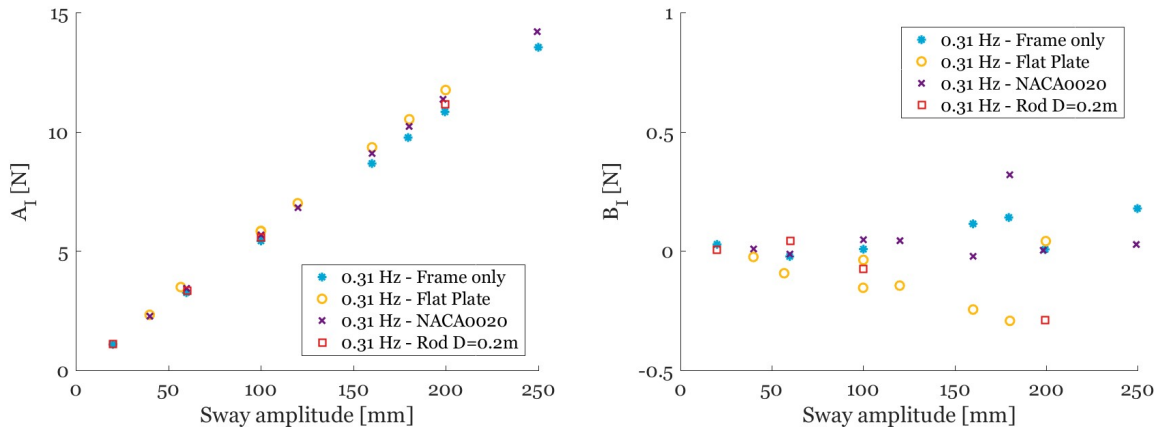

(a) Dimensionless amplitude A_I of inertia experiments at 0.31 Hz oscillation

(b) Dimensionless amplitude B_I of inertia experiments at 0.31 Hz oscillation

Figure C.5: Dimensionless amplitude A_I of inertia experiments of the 6 component frame only, the frame with flat plate model, the frame with the NACA0020 model and the frame with the aluminium rod

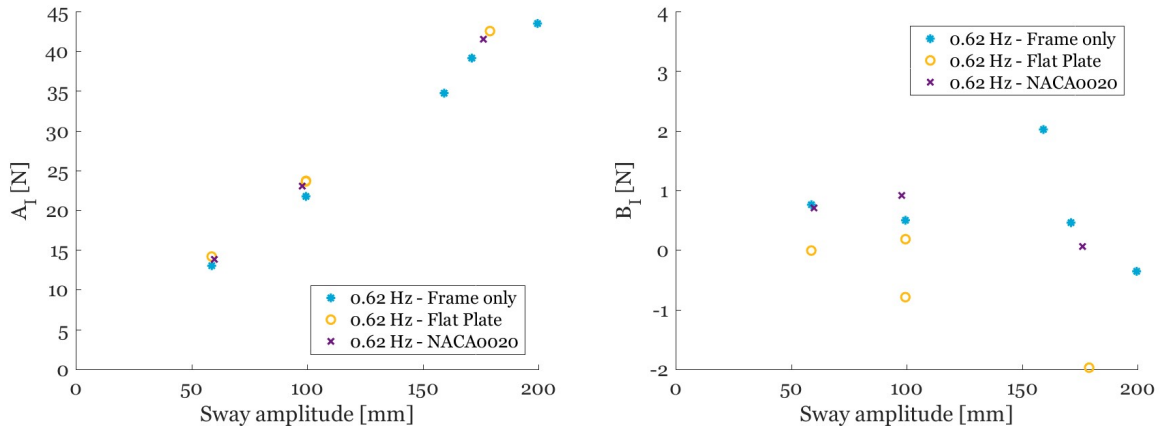

(a) Dimensionless amplitude A_I of inertia experiments at 0.62 Hz oscillation

(b) Dimensionless amplitude B_I of inertia experiments at 0.62 Hz oscillation

Figure C.6: Dimensionless amplitude A_I of inertia experiments of the 6 component frame only, the frame with flat plate model and the frame with the NACA0020 model

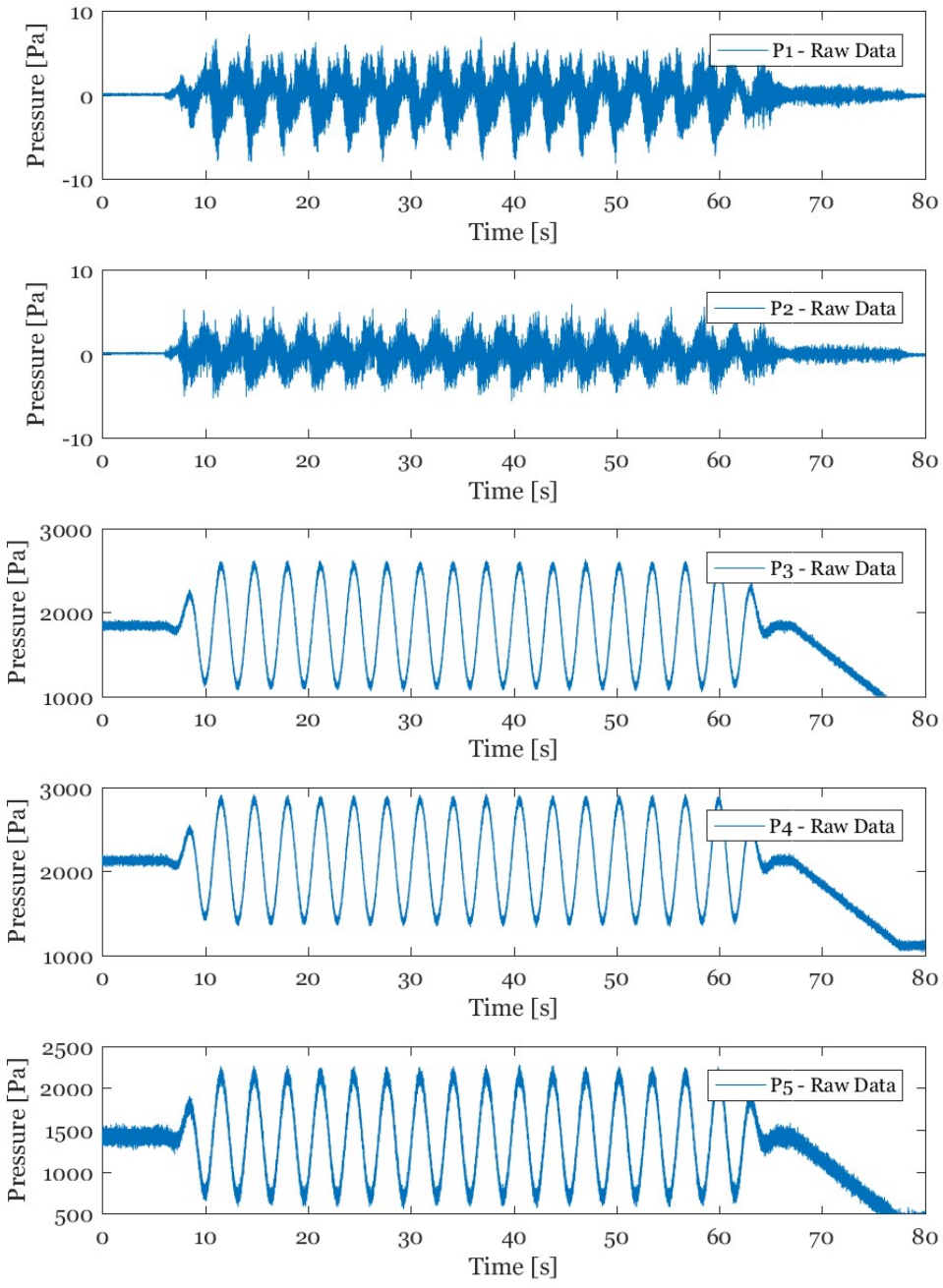

Figure C.7: Pressure signals of a vertical oscillation test at 0.31 Hz with an amplitude of 75 mm to inspect the pressure sensors after water leakage in the model. Sensor 1 and 2 do not work properly.

D

Sway oscillations

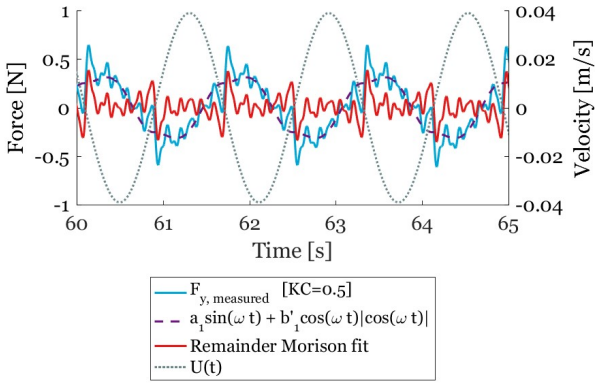

(a) F_y on the lift profile in sway oscillation at 0.62 Hz, KC = 0.5

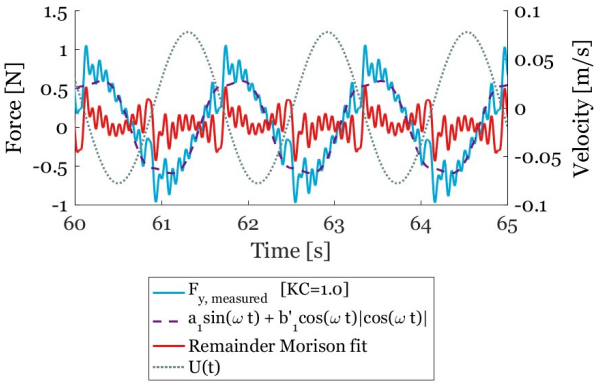

(b) F_y on the lift profile in sway oscillation at 0.62 Hz, KC = 1.0

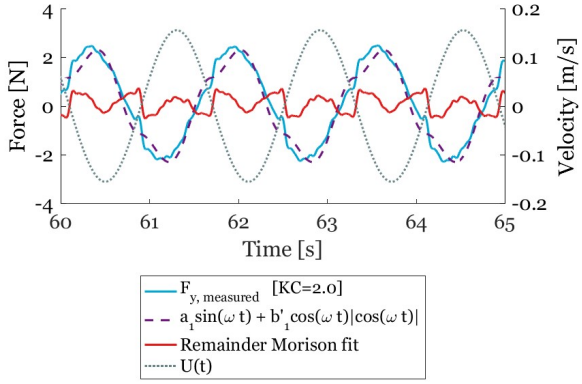

(c) F_y on the lift profile in sway oscillation at 0.62 Hz, KC = 2.0

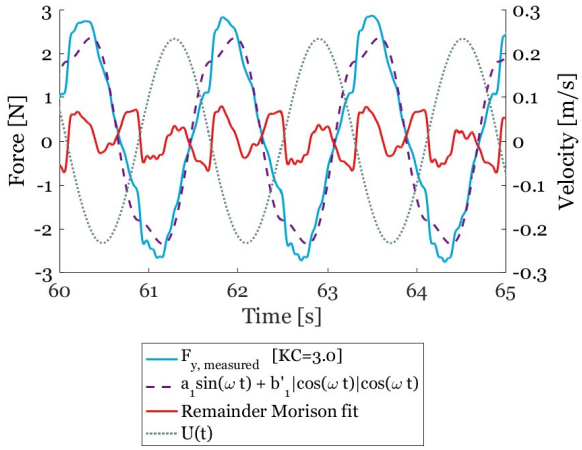

(d) F_y on the lift profile in sway oscillation at 0.62 Hz, KC = 3.0 (1)

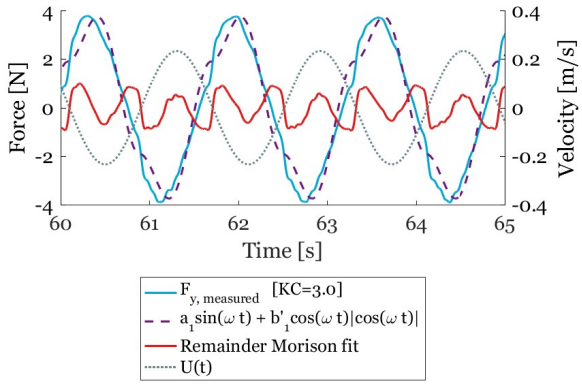

(e) F_y on the lift profile in sway oscillation at 0.62 Hz, KC = 3.0 (2)

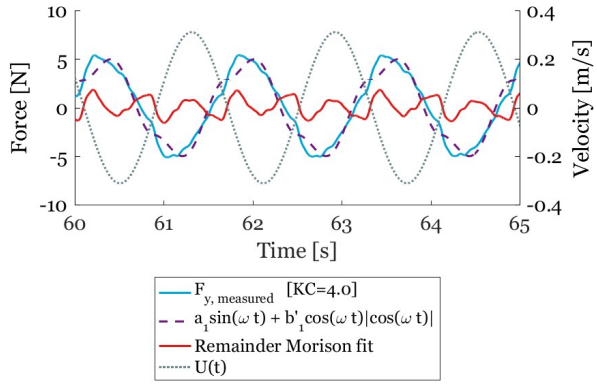

(f) F_y on the lift profile in sway oscillation at 0.62 Hz, KC = 4.0

Figure D.1: F_y on the lift profile in regular sway oscillation at 0.62 Hz

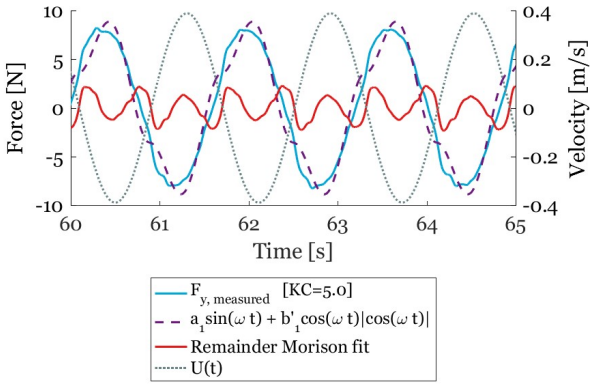

(a) F_y on the lift profile in sway oscillation at 0.62 Hz, KC = 5.0

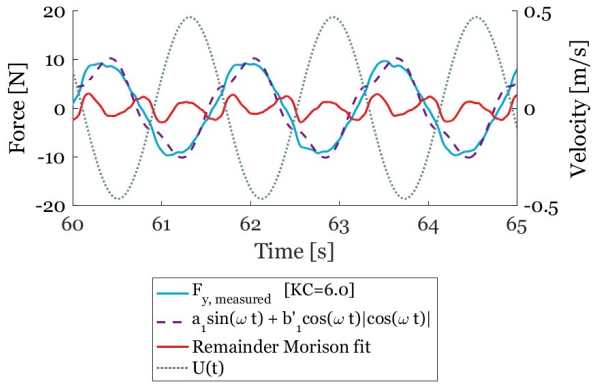

(b) F_y on the lift profile in sway oscillation at 0.62 Hz, KC = 6.0

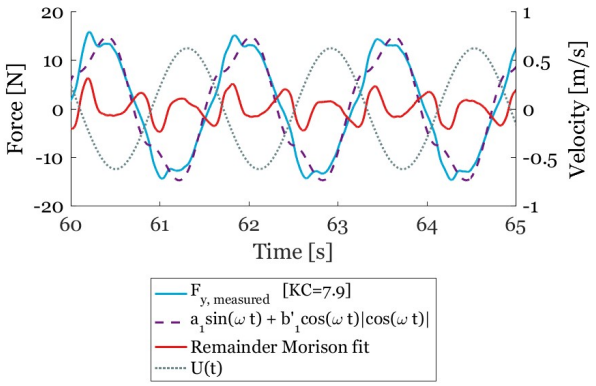

(c) F_y on the lift profile in sway oscillation at 0.62 Hz, KC = 8.0

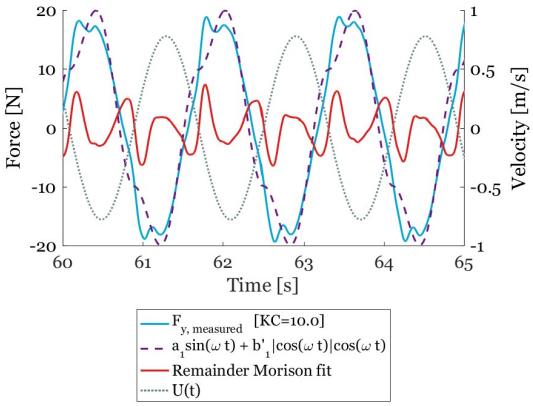

(d) F_y on the lift profile in sway oscillation at 0.62 Hz, KC = 10.0

Figure D.2: F_y on the lift profile in regular sway oscillation at 0.62 Hz

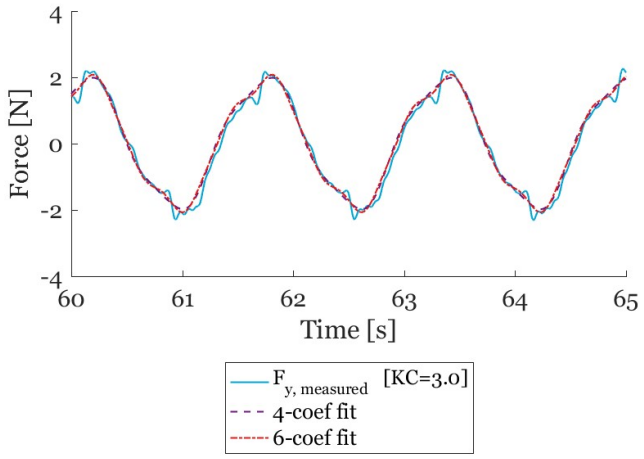

Figure D.3: Force history and 4- and 6-coefficients Morison fits of lift profile in 60 mm sway oscillation at 0.62 Hz

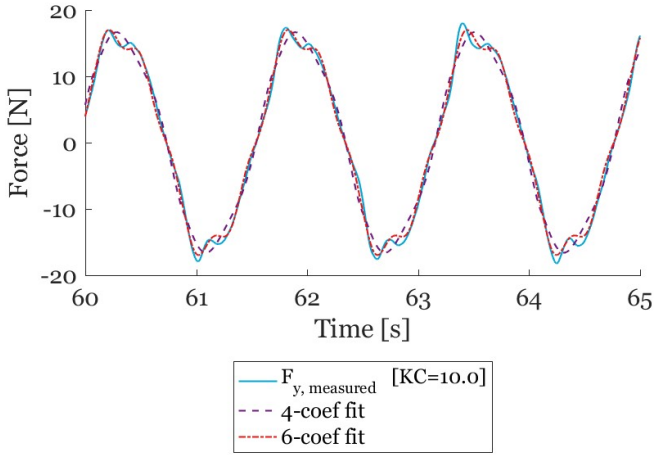

Figure D.4: Force history and 4- and 6-coefficients Morison fits of lift profile in 200 mm sway oscillation at 0.62 Hz

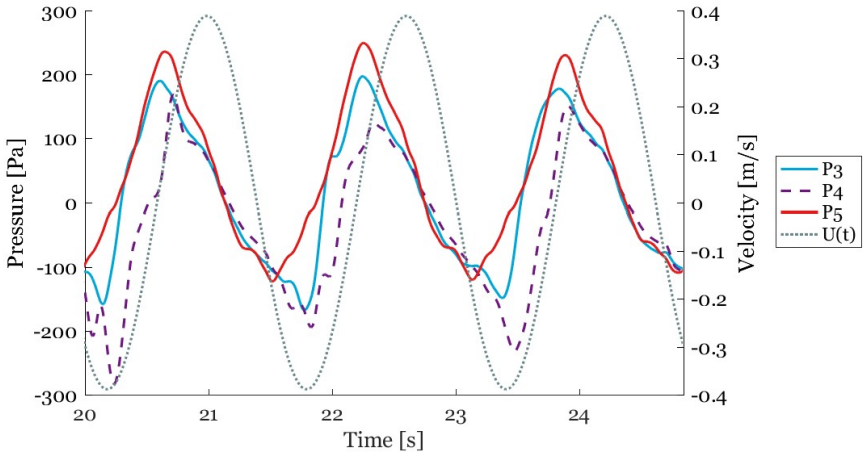

Figure D.5: Pressure measurements 100 mm sway oscillation at 0.62 Hz

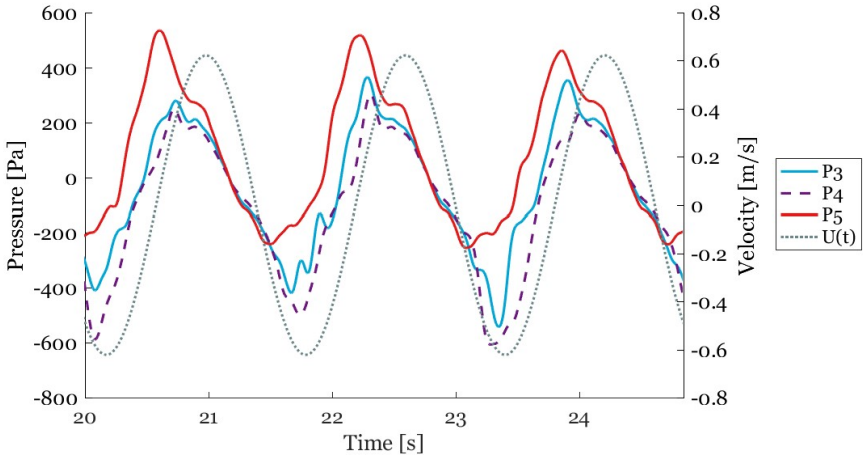

Figure D.6: Pressure measurements 160 mm sway oscillation at 0.62 Hz

E

Draught variations

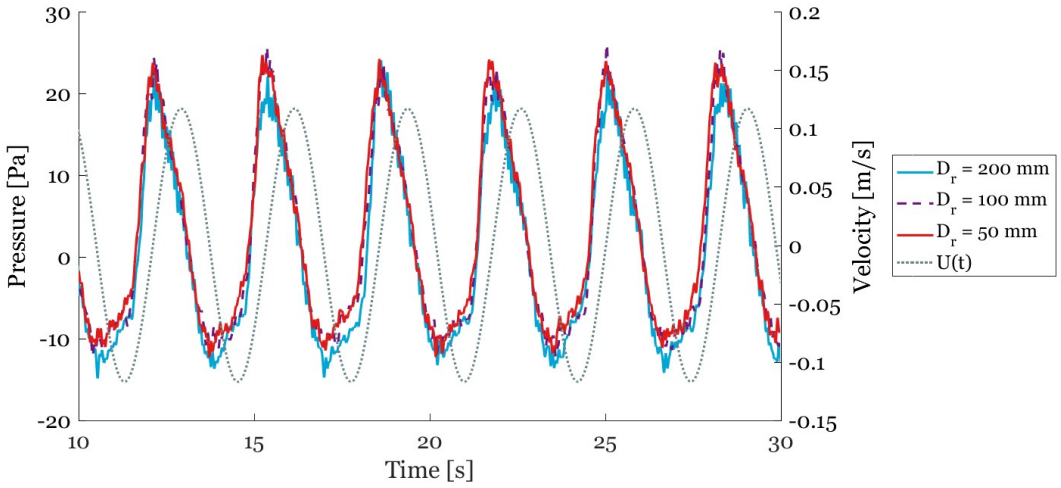

(a) Pressure signal of P3 at different draughts for a 60 mm 0.31 Hz sway oscillation

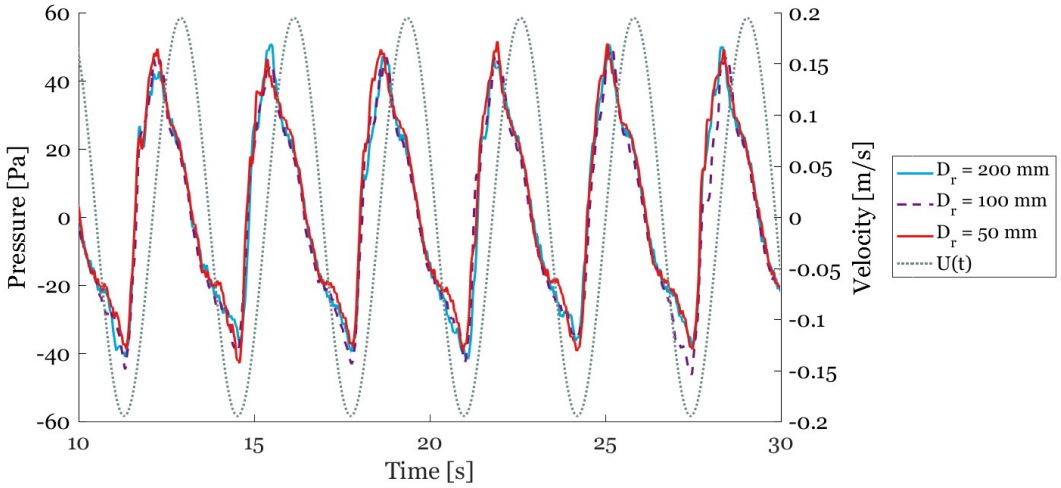

(b) Pressure signal of P3 at different draughts for a 100 mm 0.31 Hz sway oscillation

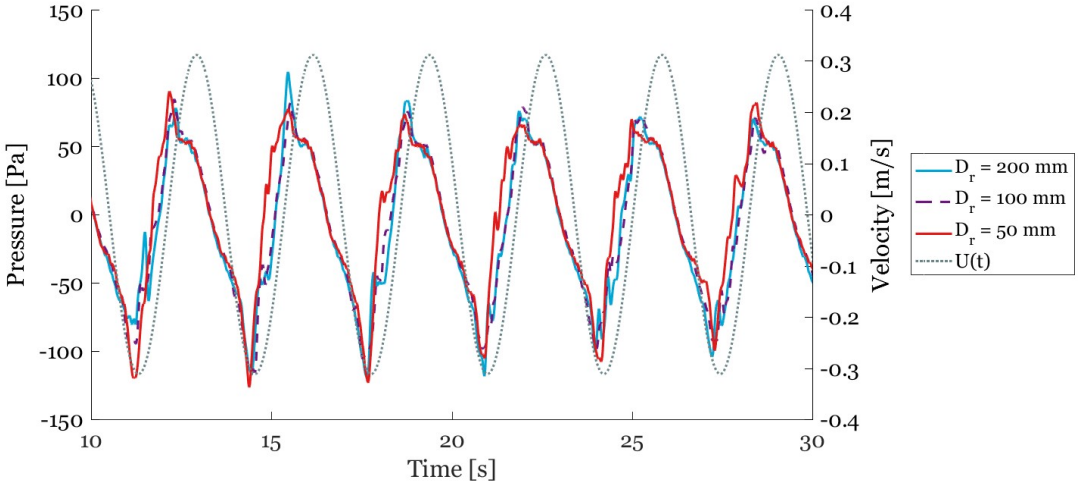

(c) Pressure signal of P3 at different draughts for a 160 mm 0.31 Hz sway oscillation

Figure E.1: P3 pressure signals at different draughts in 0.31 Hz sway oscillation

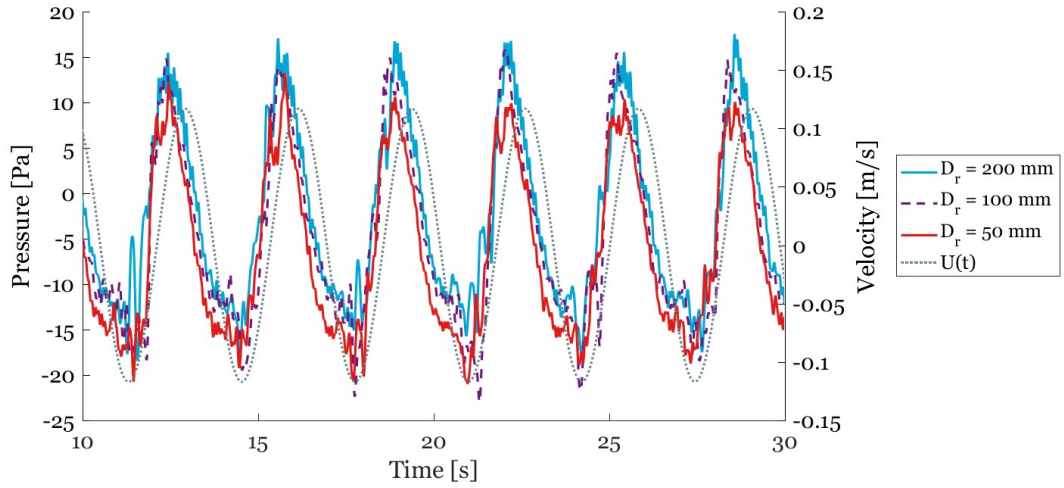

(a) Pressure signal of P4 at different draughts for a 60 mm 0.31 Hz sway oscillation

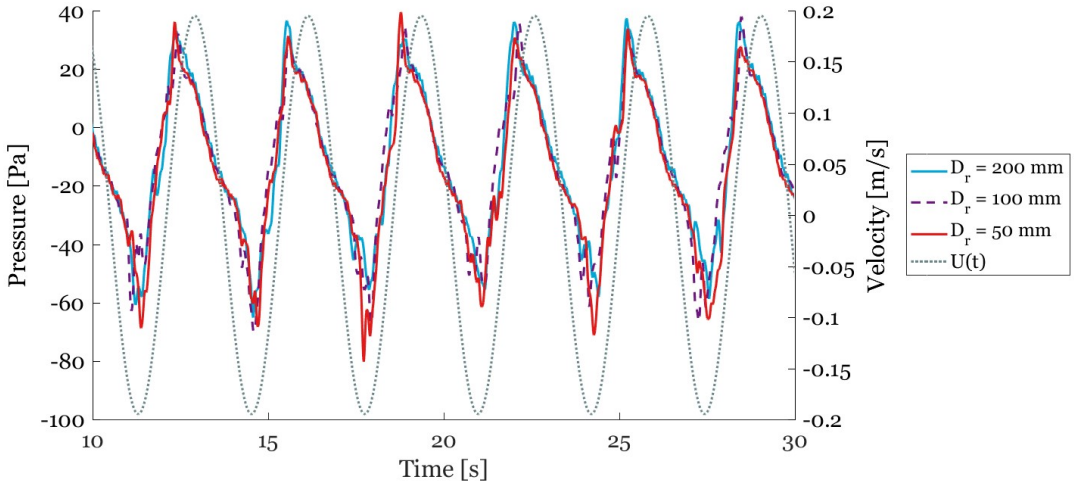

(b) Pressure signal of P4 at different draughts for a 100 mm 0.31 Hz sway oscillation

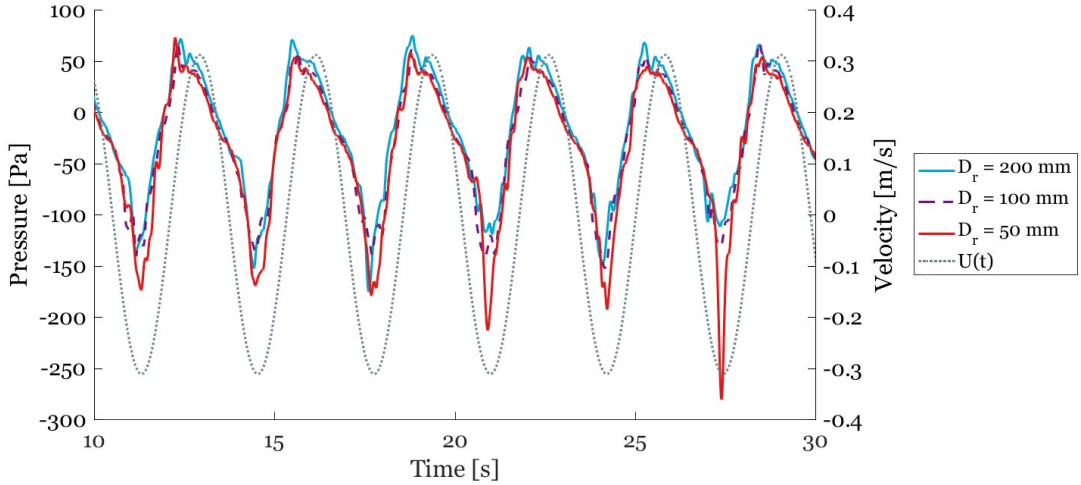

(c) Pressure signal of P4 at different draughts for a 160 mm 0.31 Hz sway oscillation

Figure E.2: P4 pressure signals at different draughts in 0.31 Hz sway oscillation

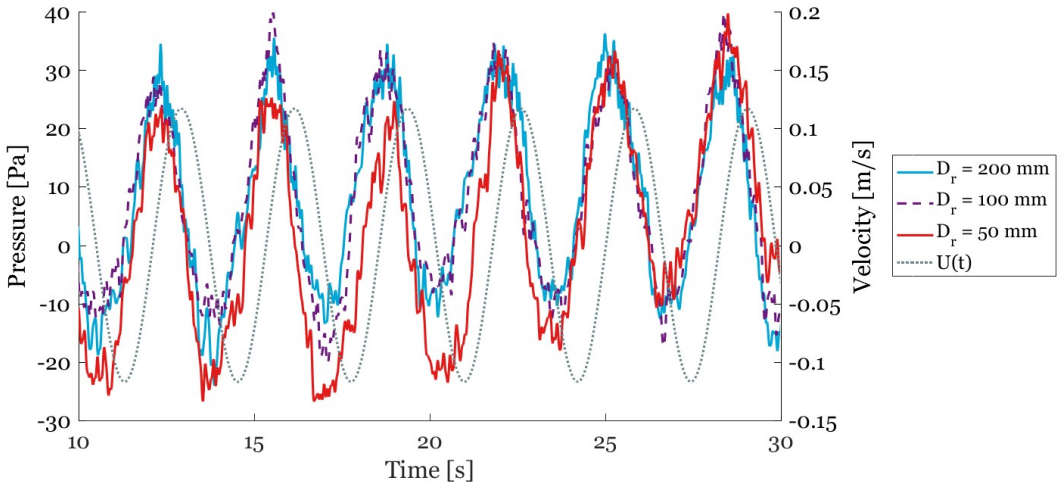

(a) Pressure signal of P5 at different draughts for a 60 mm 0.31 Hz sway oscillation

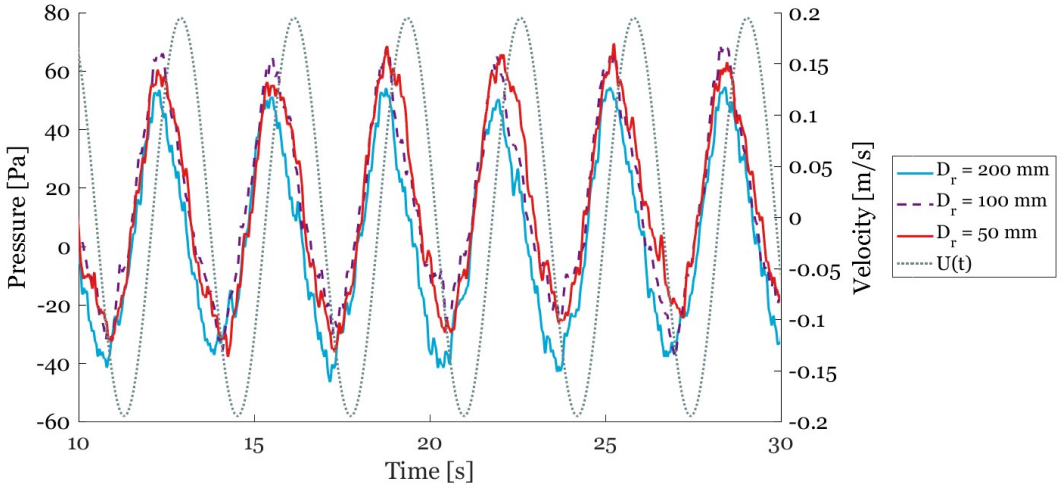

(b) Pressure signal of P5 at different draughts for a 100 mm 0.31 Hz sway oscillation

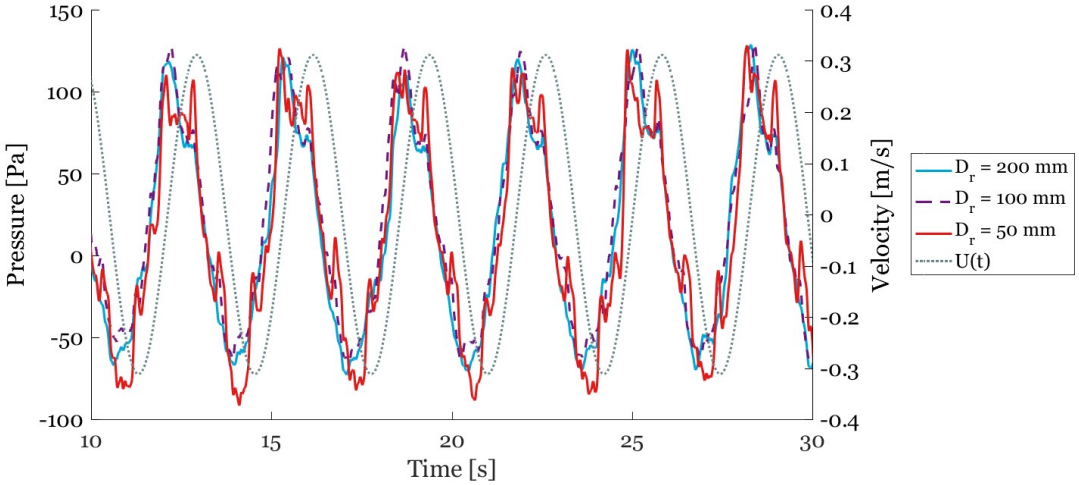

(c) Pressure signal of P5 at different draughts for a 160 mm 0.31 Hz sway oscillation

Figure E.3: P5 pressure signals at different draughts in 0.31 Hz sway oscillation

F

Pressure signals in current

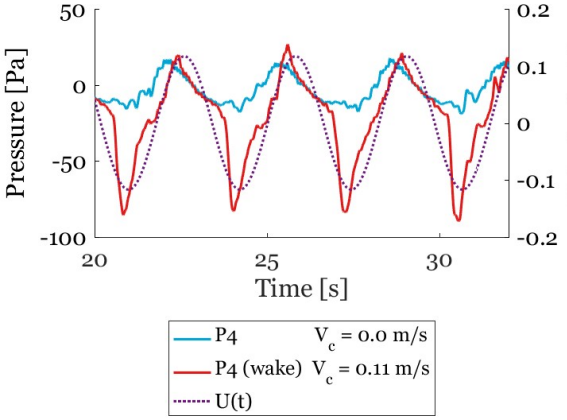

(a) P4-AS in 60 mm oscillation at 0.31 Hz

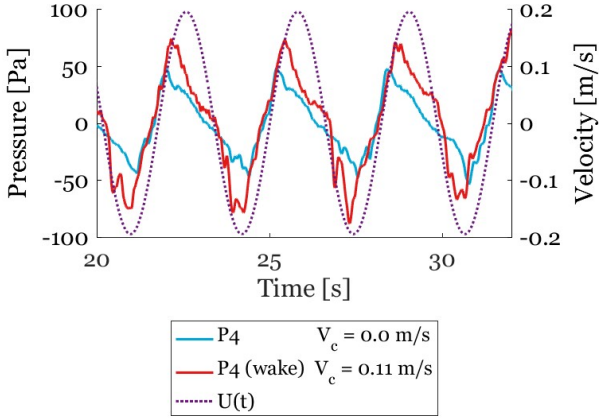

(b) P4-AS in 100 mm oscillation at 0.31 Hz

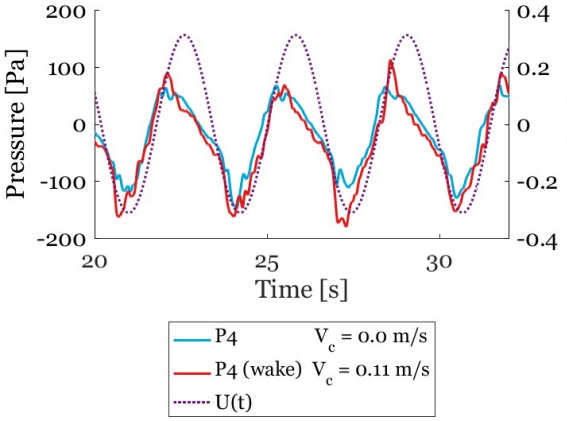

(c) P4-AS in 160 mm oscillation at 0.31 Hz

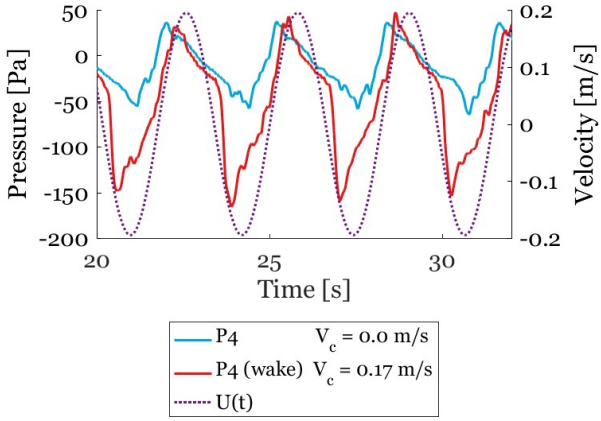

(d) P4-AS in 100 mm oscillation at 0.31 Hz

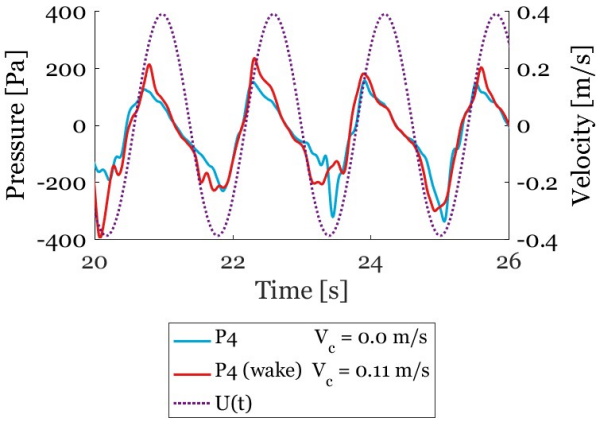

(e) P4-AS in 100 mm oscillation at 0.62 Hz

Figure F.1: Time trace of P4-AS in current compared with P4 in zero-current

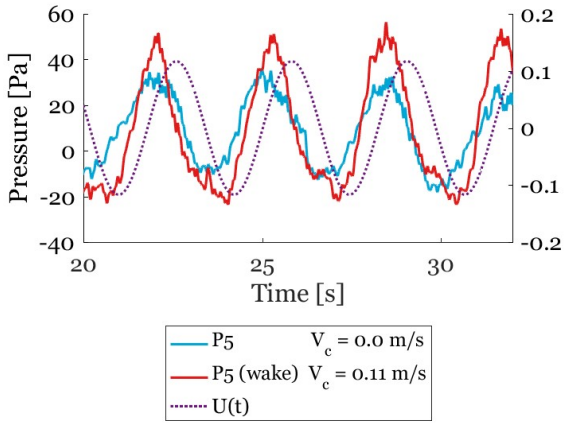

(a) P5-AS in 60 mm oscillation at 0.31 Hz

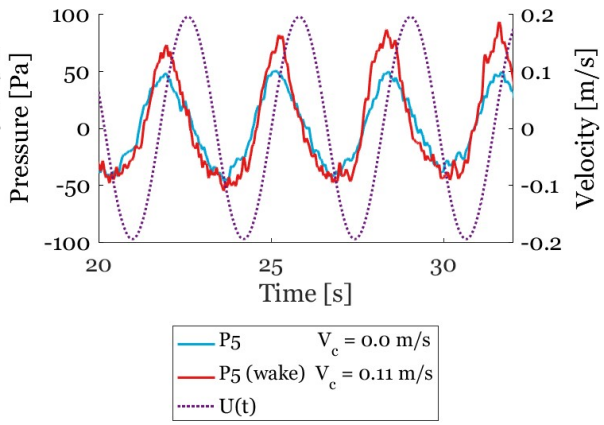

(b) P5-AS in 100 mm oscillation at 0.31 Hz

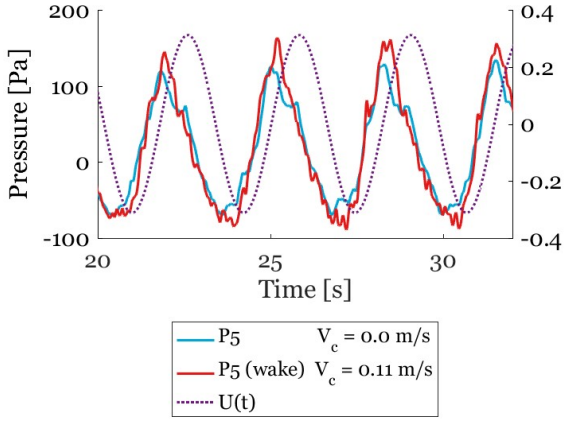

(c) P5-AS in 160 mm oscillation at 0.31 Hz

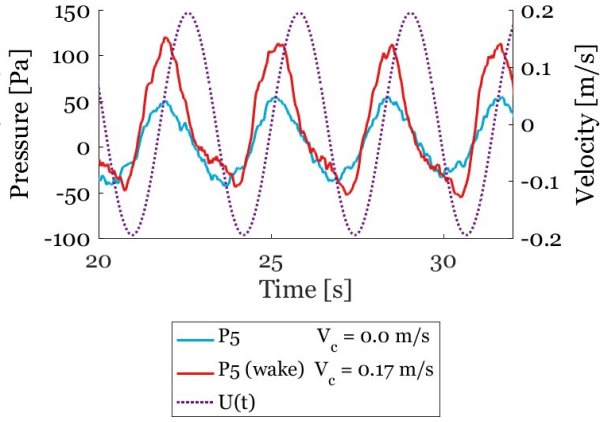

(d) P5-AS in 100 mm oscillation at 0.31 Hz

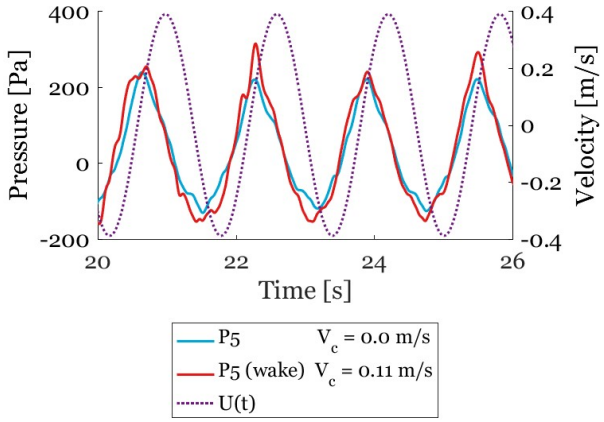

(e) P5-AS in 100 mm oscillation at 0.62 Hz

Figure E.2: Time trace of P5-AS in current compared with P5 in zero-current

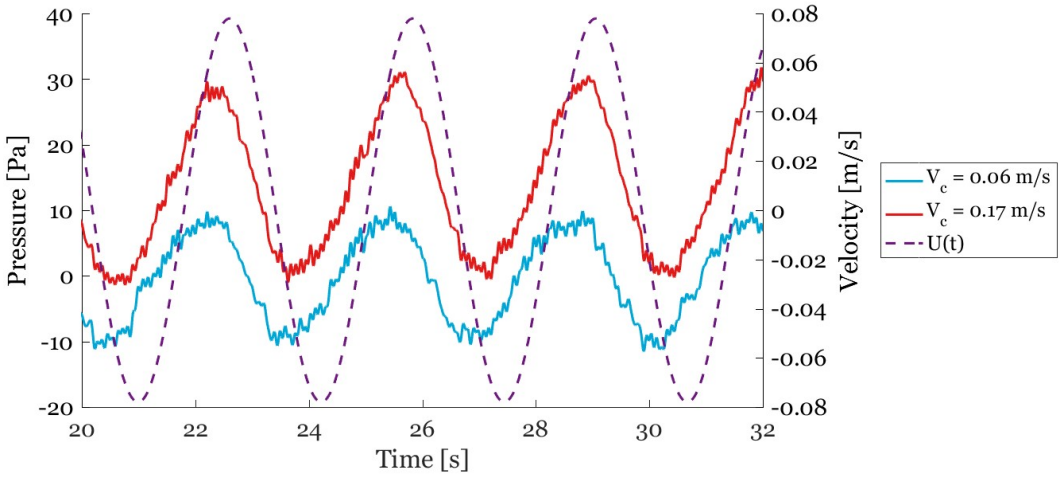

(a) P3-FS of the flat plate in 40 mm sway oscillation at 0.31 Hz with V_c = 0.00, 0.06, 0.11 and 0.17 m/s

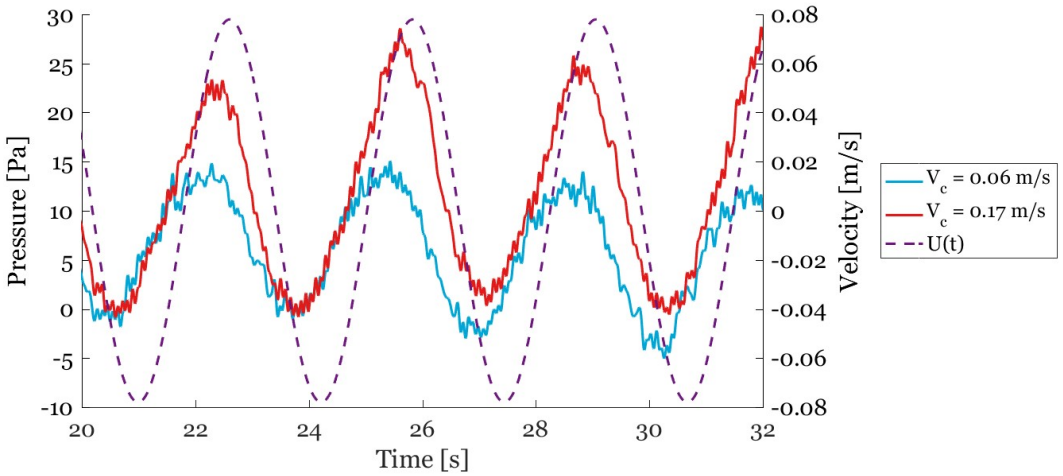

(b) P4-FS of the flat plate in 40 mm sway oscillation at 0.31 Hz with V_c = 0.00, 0.06, 0.11 and 0.17 m/s

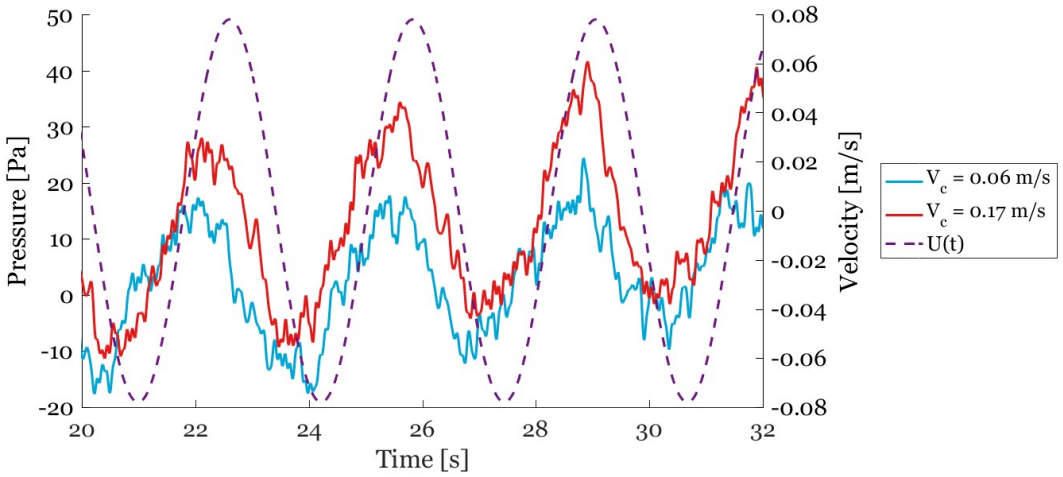

(c) P5-FS of the flat plate in 40 mm sway oscillation at 0.31 Hz with V_c = 0.00, 0.06, 0.11 and 0.17 m/s

Figure F.3: FS-sensors' time traces in 40 mm sway oscillation at 0.31 Hz in various current speeds

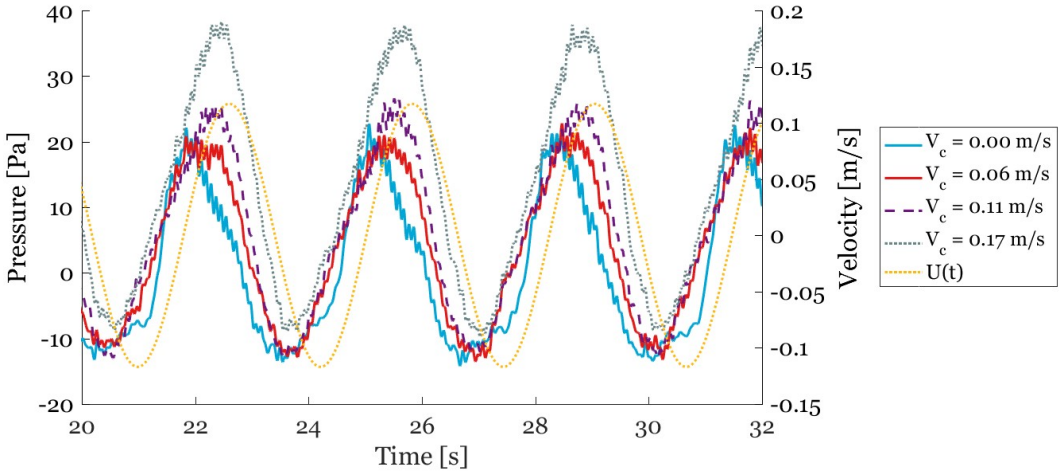

(a) P3-FS of the flat plate in 60 mm sway oscillation at 0.31 Hz with V_c = 0.00, 0.06, 0.11 and 0.17 m/s

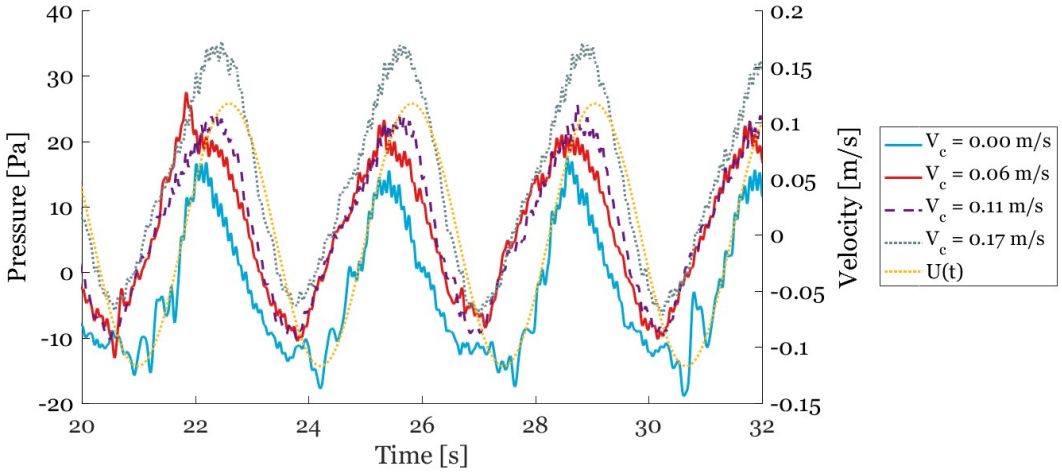

(b) P4-FS of the flat plate in 60 mm sway oscillation at 0.31 Hz with V_c = 0.00, 0.06, 0.11 and 0.17 m/s

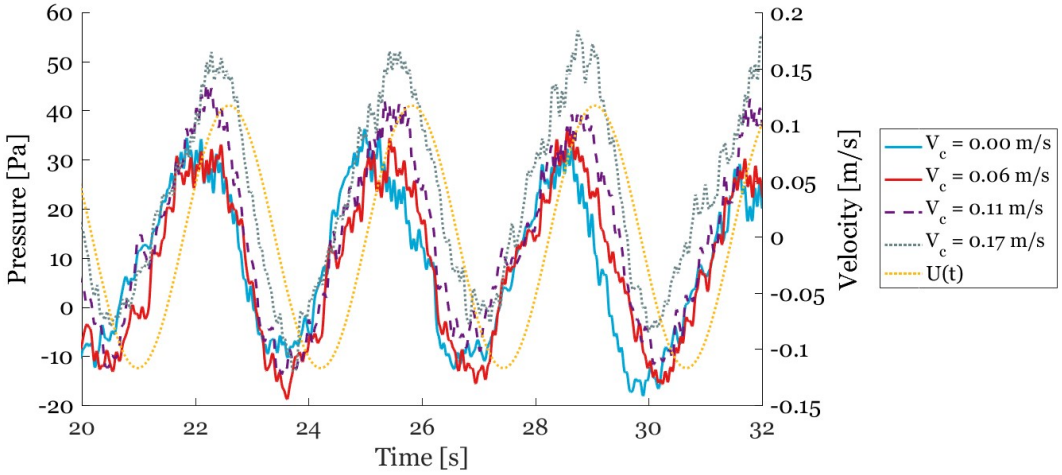

(c) P5-FS of the flat plate in 60 mm sway oscillation at 0.31 Hz with V_c = 0.00, 0.06, 0.11 and 0.17 m/s

Figure E4: FS-sensors' time traces in 60 mm sway oscillation at 0.31 Hz in various current speeds

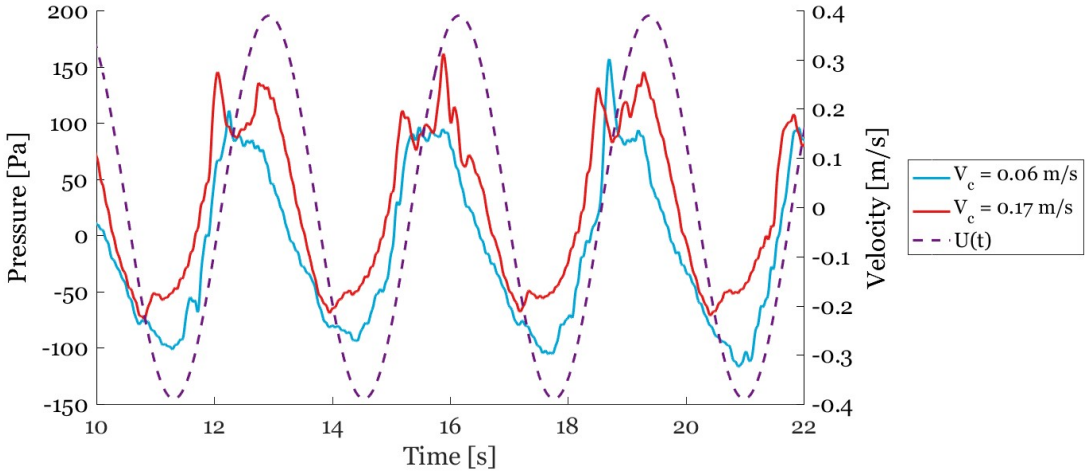

(a) P3-FS of the flat plate in 200 mm sway oscillation at 0.31 Hz with V_c = 0.00, 0.06, 0.11 and 0.17 m/s

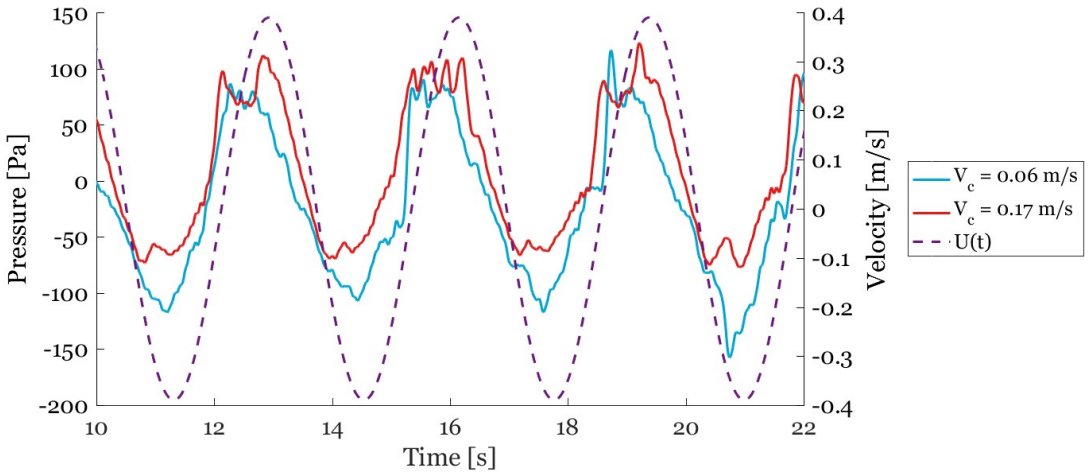

(b) P4-FS of the flat plate in 200 mm sway oscillation at 0.31 Hz with V_c = 0.00, 0.06, 0.11 and 0.17 m/s

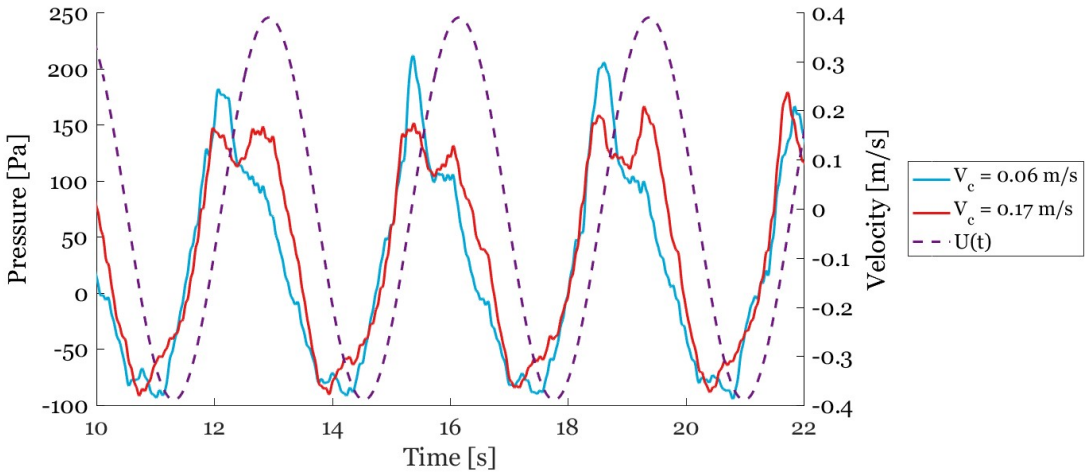

(c) P5-FS of the flat plate in 200 mm sway oscillation at 0.31 Hz with V_c = 0.00, 0.06, 0.11 and 0.17 m/s

Figure F.5: FS-sensors' time traces in 200 mm sway oscillation at 0.31 Hz in various current speeds

G

Oscillations in current

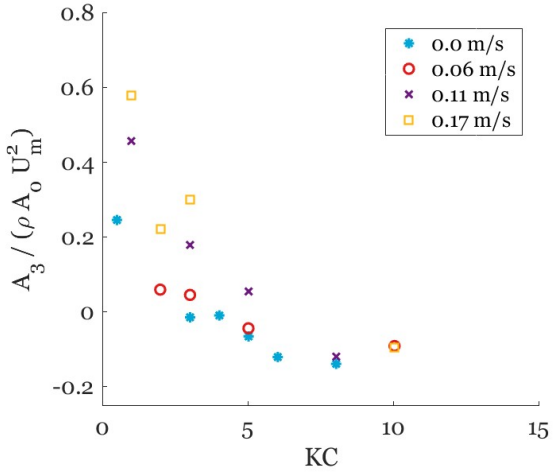

(a) A_3 in 0.31 Hz oscillation versus KC

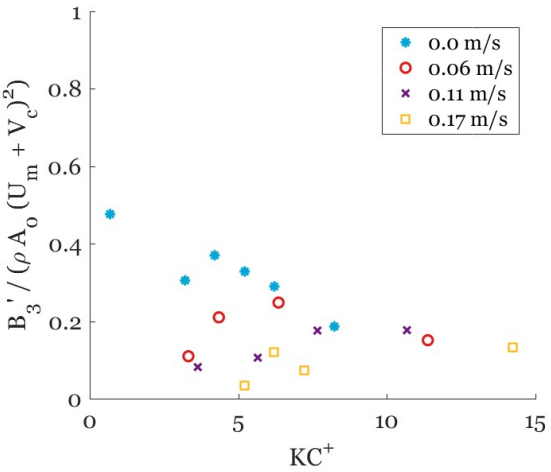

(b) B_3' in 0.31 Hz oscillation versus K^+

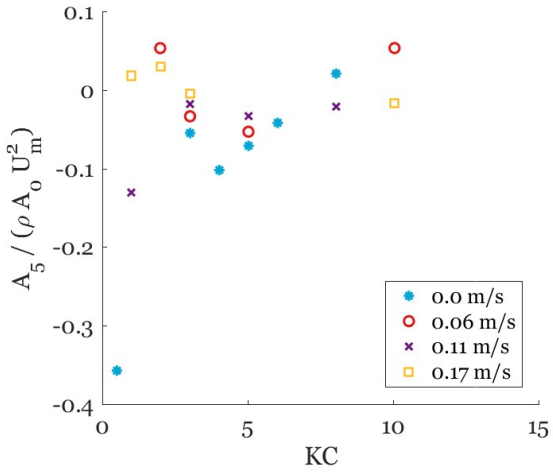

(c) A_5 in 0.31 Hz oscillation versus KC

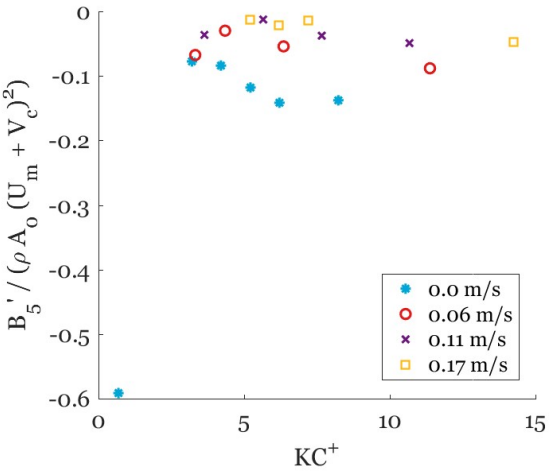

(d) B_5' in 0.31 Hz oscillation versus K^+

Figure G.1: Third- and fifth order Fourier terms for the flat plate model in 0.31 Hz sway oscillation with currents acting perpendicular to the blade

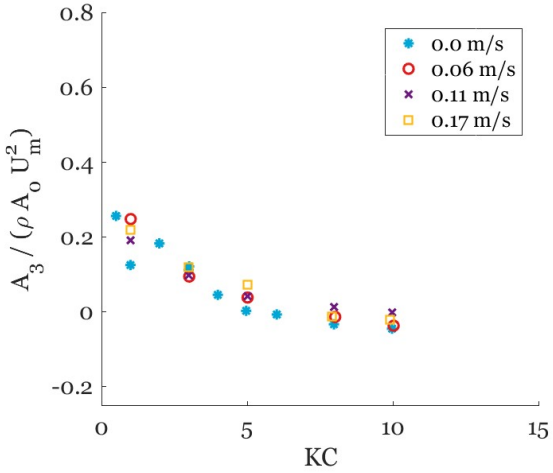

(a) A_3 in 0.62 Hz oscillation versus KC

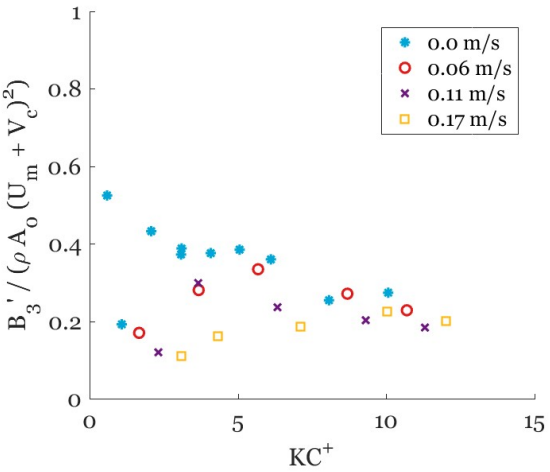

(b) B_3' in 0.62 Hz oscillation versus K^+

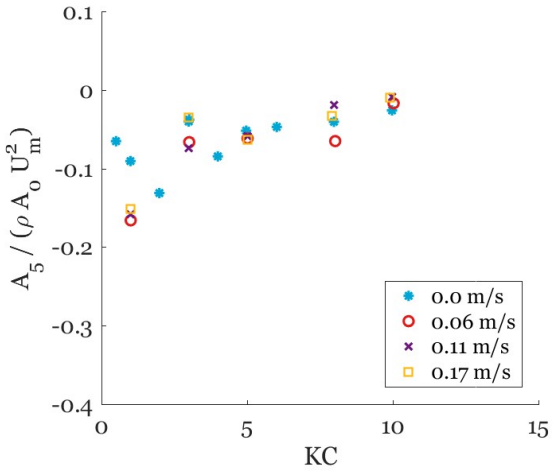

(c) A_5 in 0.62 Hz oscillation versus KC

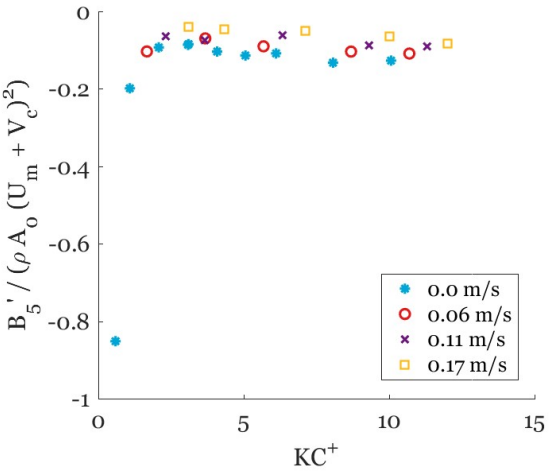

(d) B_5' in 0.62 Hz oscillation versus K^+

Figure G.2: Third- and fifth order Fourier terms for the lift profile in 0.62 Hz sway oscillation with currents acting perpendicular to the blade

Bibliography

Barrass, C. (2004). *Ship design and performance for masters and mates.* Elsevier Butterworth-Heinemann, Oxford.

Bearman, P. (1984). Vortex shedding from oscillating bluff bodies. *Journal of Fluid Mechanics*, (16), 195–222.

BestShippingNews.com (2018). Electro hydraulic 4-ram steering gear.

Blevins, R. D. (1990). *Flow induced vibration.* Krieger Publishing Company, New York, second edi edition.

Butterworth, S. (1930). On the theory of filter amplifiers. *Experimental Wireless and the Wireless Engineer*, **7**, 536–541.

Cozanet, H. (2006). Repair on a propeller.

Det Norske Veritas (2007). *DNV-RP-C205: Environmental conditions and environmental loads.*

Dyke, M. v. (1982). *Album of fluid motion.* Stanford California,Parabolic Press.

Earle, S. (2015). Physical Geology.

England, L. T., Duggal, A. S., and Queen, L. A. (2001). A Comparison Between Turret and Spread Moored F(P)SOs for Deepwater Field Developments. *Deep Offshore Technology*, pages 1–23.

Faltinsen, O. M. (2005). Hydrodynamics of high-speed marine vehicles.

Graham, J. M. R. (1980). The forces on sharp-edged cylinders in oscillatory flow at low Keulegan-Carpenter numbers. *Journal of Fluid Mechanics*, **97**, 331–346.

Holthuijsen, L. (2007). *Waves in Oceanic and Coastal Waters.* Cambridge University Press, New York, 1 edition.

Hyundai Heavy Industries (2014). Rudder plan of ship no. 1114.

Ikeda, Y. (1983). On the form of nonlinear roll damping of ships. Technical report, Technische Universität Berlin, institut für schiffs- und meerestechnik.

Ikeda, Y., Komatsu, K., Himeno, Y., and Tanaka, N. (1979). Effect of Hull Surface Pressure Created by Bilge Keels. Technical report, Department of Naval Architecture, University of Osaka Prefecture, Osaka.

Ikeda, Y., Ali, B., and Yoshida, H. (2004). A roll damping prediction method for a FPSO with steady drift motion. In *Proceedings of the fourteenth international offshore and polar engineering conference*, pages 676–681.

International Association of Classification Societies (2001). No. 34 Standard Wave Data.

International Towing Tank Commitee (2008). ITTC – Recommended Procedures and Guidelines ITTC: 7.5-02 06-04. Forces and Moment Uncertainty Analysis. pages 1–8.

Journée, J. M. J., Massie, W. W., and Huijsmans, R. H. M. (2015). *Offshore Hydromechanics.* Delft University of Technology, Delft, 3th edition.

Keulegan, G. H. and Carpenter, L. H. (1958). Forces on cylinders and plates in an oscillating fluid. *Journal of research of the national bureau of standards*, pages 423–440.

Kundu, P. K., Cohen, I. M., and Dowling, D. R. (2016). *Fluid Mechanics.* Elsevier Inc., London, sixth edit edition.

Ladson, C. L., Brooks, C. W., Hill, A. S., and Sproles, D. W. (1996). Computer pgrogram to obtain ordinates for NACA Airfoils. Technical report, National Aeronautics and Space Administration, Hampton.

Lay, D. C., Lay, S. R., and McDonald, J. J. (2016). *Linear algebra and its applications*. Pierson Education Inc., Boston, 5th edition.

Li, C. (1989). Force coefficients of spheres and cubes in oscillatory flow with and without current. Technical report, NTH, Trondheim.

Lloyd's Register (2003). FPSO Inspection Repair and Maintenance - Study into Best Practice. Technical report, Lloyd's Register of Shipping, UKOOA.

Maritime and Transport Technology (2017a). Hexamove.

Maritime and Transport Technology (2017b). Towing Tank No. 1.

MathWorks (2018). MathWorks Documentation: butter.

MODEC (2016). FPSO Cidade de Caraguatatube MV27.

Molland, A. F. and Turnock, S. R. (2007). *Marine rudders and control surfaces*. Elsevier Ltd.

Remery, G. F. and Oortmerssen, G. (1973). The mean wave, wind and current forces on offshore structures and their role in the design of mooring systems. In *Offshore technology conference*, pages 170–180. American institute of mining, metallurgical and petroleum engineers.

Ridjanovic, M. (1962). Drag coefficients of flat plates oscillating normally to their planes. *Schiffstechnik*.

Sarpkaya, T. and Isaacson, M. (1981). *Mechanics of wave forces on offshore structures*. Litton Educational Publishing Inc., New York.

Sarpkaya, T. and O'Keefe, J. L. (1996). Oscillating flow about two and three-dimensional bilge keels. *Journal of offshore mechanics and arctic engineering*.

Sarpkaya, T. and Storm, M. (1985). In-line force on a cylinder translating in oscillatory flow. *Applied Ocean Research*, pages 188–196.

Shafiee-far, M. (1997). Hydrodynamic Interaction Between Fluid Flow and Oscillating Slender Cylinders. Technical report, Delft University of Technology, Delft.

Sheldahl, R. E. and Klimas, P. C. (1981). Aerodynamic characteristics of seven symmetrical airfoil sections through 180-degree angle of attack for use in aerodynamic analysis of vertical axis wind turbine. Technical report, Sandia National Labaratories.

Shimamura, Y. (2002). FPSO/FSO: State of the art. *Journal of Marine Science and Technology*, **7**, 59–70.

Tanaka, N., Ikeda, Y., and Nishino, K. (1982). Hydrodynamic viscous force acting on oscillating cylinders with various shapes. In *6th Symposium of Marine Technology, The Society of Naval Architects of Japan*. Department of Naval Architecture University of Osaka.

Van der Kolk, N. J., Keuning, J. A. ., and Huijsmans, R. (2018). Part 1: Experimental Validation of a RANS-CFD Methodology for the Hydrodynamics of Wind-Assisted Ships Operating at Leeway Angles. Technical report, Delft University of Technology, Delft.

Van 't Veer, R., Fathi, F., and Kherian, J. G. (2011). On roll hydrodynamics of FPSO's fitted with bilge keels and riser balcony. In *International conference of ocean, offshore and arctic engineering*.

Van 't Veer, R., Pistidda, A., and Koop, A. (2012). Forces on bilge keels in regular and irregular oscillating flow.

Van 't Veer, R., Schut, X., and Huijsmans, R. (2015). Bilge keel loads and hull pressures created by bilge keels fitted to a rotating cylinder. *Applied Ocean Research*.

White, F. M. (2011). *Fluid Mechanics*. McGraw-Hill, Rhode Island, 7th edition.